ELECTRICAL RESISTIVITY AND ELECTRON MICROSCOPIC STUDIES OF LATTICE DEFECTS IN THE MICROPLASTIC REGION IN PURE NICKEL

by

Raj Narain Singh

Thesis submitted in partial fulfillment
of the requirements for the degree of
Master of Science

The Faculty of Graduate Studies and Research
Department of Mechanical Engineering
University of Manitoba
Winnipeg

August 1969

ABSTRACT

The generation of point and line defects and also their interactions during tensile deformation of pure nickel in the micro-plastic region (strain range of 1.0×10^{-4} to 45.0×10^{-4}) have been investigated by electrical resistivity measurements and transmission electron microscopy. Grain boundaries and twin boundaries were observed to act as dislocation sources and a mechanism is proposed to explain their production. At all levels of strain, some dislocation activity and entanglement in isolated areas was observed. The mechanisms responsible for tangling are discussed.

Point defects (vacancies) were produced even at very low tensile deformations and a mechanism for their generation is proposed. The vacancy concentration (C_v) was measured by electrical resistivity and was found to obey the following relationship with tensile strain (ε),

$$C_v \text{ (at. pct. vac)} = 4.54 \times 10^{-3} \varepsilon^{0.36}$$

Measurements on residual lattice strains (by an x-ray diffraction technique) have been related to the electron microscopic observations in thin foils and a possible explanation, using a model based on point defects and dislocation substructure has been proposed. The dislocation substructure was found to generate hydrostatic stresses.

Single stacking faults, overlapping stacking faults and deformation twins were produced during tensile deformation of polycrystalline nickel. The faults were analysed and found to be intrinsic in nature. These faults were seen to originate at grain boundaries, at twin boundaries and also at the intersection of slip planes. A mechanism is proposed to explain their formation.

ACKNOWLEDGEMENT

I wish to express my sincere thanks to Dr. K. Tangri, Professor, Metallurgical Science, for his continued help and advice throughout this work.

TABLE OF CONTENTS

Table of Contents continued

FIGURE INDEX

Figure Index continued

TABLE INDEX

1. INTRODUCTION AND OBJECTIVES

It has been ten years since Bollman[1] and Hirsch et al.[2] first observed dislocations using transmission electron microscopy. Since then many studies of dislocation arrangements and interactions have been made mainly on FCC metals.

There have been many transmission studies, using thin foils, of dislocation distribution in deformed crystals of FCC metals[3-10], however, no clear picture of the dislocation distribution and the mechanism of its formation has so far emerged. The results on polycrystals have been even more complex. Furthermore, the majority of work on FCC single and polycrystals has been done only at higher strains (more than 1 pct) with the result that the dynamics of dislocations in the microplastic region are not yet well understood.

Many investigations, particularly those of Kuhlmann-Wilsdorf[11] and Mott[12] have clearly established that point defects are produced during plastic deformation. Since these defects influence dislocation dynamics in a variety of ways, their study (using some indirect method e.g. resistivity) is essential. One of the objectives of this work is to study the origin and nature of point and line defect generation and the interaction between them.

Polycrystals deformed plastically in uniaxial tension show residual lattice strains (RLS). Simultaneous measurements of lattice (elastic) strain by the x-ray line shift method and total strain with an electrical strain gauge have been carried out on polycrystalline nickel[13]. The rate of increase in the lattice strain was found to follow the total strain closely until the plastic strain

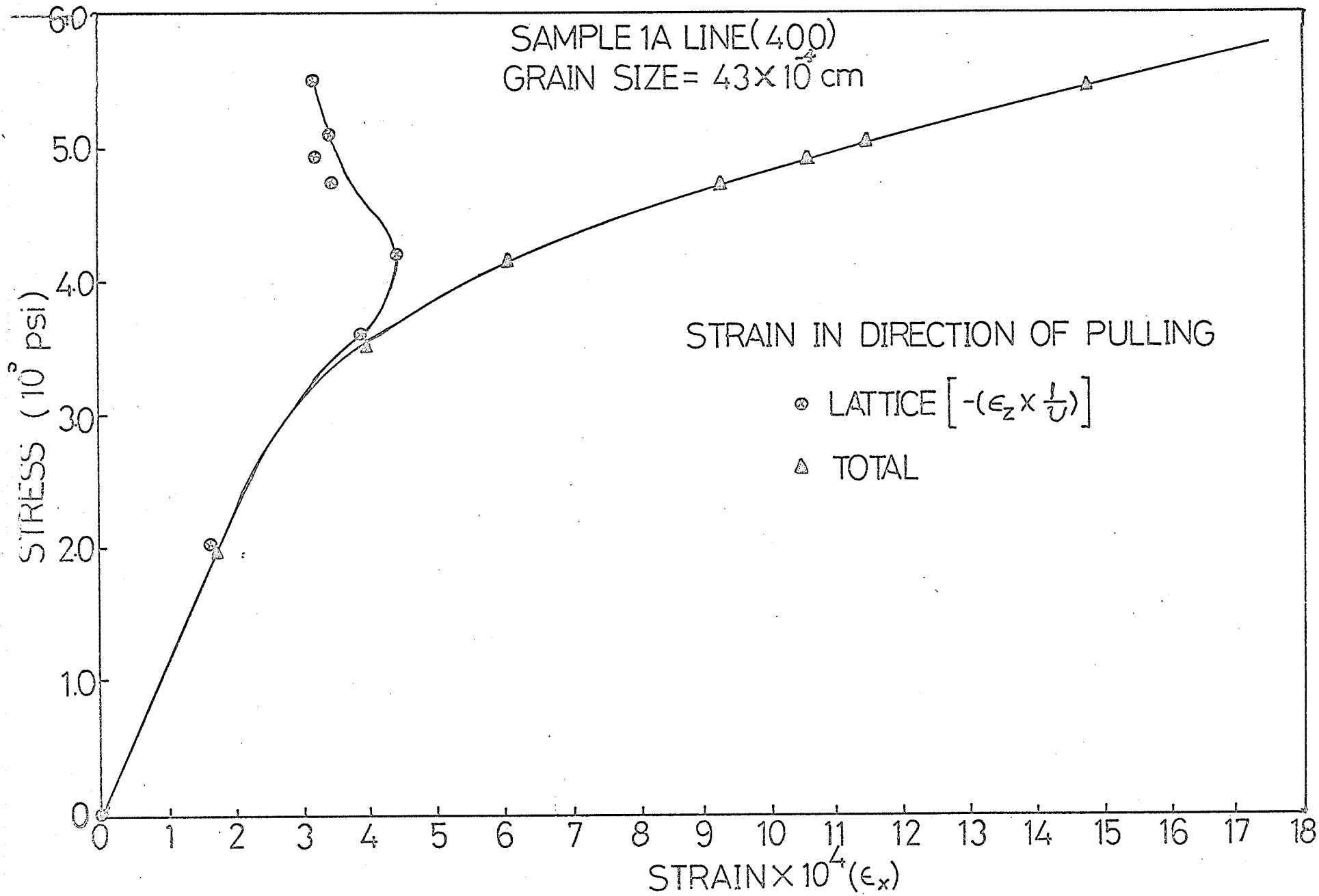

FIG.1 LATTICE AND TOTAL STRAIN, BOTH IN THE DIRECTION OF PULLING, VS STRESS DURING UNIAXIAL LOADING OF NICKEL

set as shown in Figure 1. Thereafter the two strains deviated from each other and the rate of increase of lattice strain eventually decreased. Depending upon the mode of unloading, both compressive and tensile strains were observed in nickel deformed up to 0.29 pct strain. These results were explained on the basis of the effects of clustering of dislocations and also the production and behaviour of point defects during loading and unloading, respectively.

To further investigate this hypothesis original nickel[13] specimens were deformed within the strain range of 1.0×10^{-4} to 45.0×10^{-4}, to cover the whole of the elastic-plastic region (Figure 1) and were examined using transmission electron microscopy and electrical resistivity techniques.

Thus the two objectives of the present investigation are:

1. To study the dislocation dynamics in the microplastic region of nickel and
2. To investigate the origin and the nature of residual lattice strains in the microplastic region of nickel.

2. EXPERIMENTAL PROCEDURE

2.1 Material

Nickel of 99.98% purity, made available through the courtesy of the International Nickel Co. of Canada in the form of 0.016 cm thick rolled sheets, was employed for this investigation. The chemical analysis of the material is given in Table 1.

Table 1

Composition (pct by weight)

Elements	Ni	C	Mn	Fe	Cu	Cr	S	Si	Mg	Ti	Co
Nominal	99.98	0.01	<0.001	<0.001	<0.001	<0.001	<0.001	<0.001	<0.001	<0.001	<0.001
Limiting	99.97	0.02	0.001	0.005	0.001	0.001	0.001	0.001	0.001	<0.001	<0.001

2.2 Specimen Preparation and Heat Treatment

Small strips (1.3 cm x 10 cm) were cut from the 0.016 cm thick sheet and cold rolled to a thickness of about 0.013 cm. A thickness of 0.013 cm was necessary to give sufficient resistance for accurate resistivity measurements and also to reduce the time to thin down the specimen for transmission electron microscopy. The rolled strips were cut to a size of about 8mm x 12 cm with a shear cutter and cleaned in an ultrasonic cleaner. The potential leads were strips of the same material spot welded to the specimen. The separation between the potential leads was about 10 cm, i.e. large enough to give an accurate resistance measurement but small enough to handle without undue deformation. The final shape of the resistivity specimens with the potential and current leads spot welded at 'A' and 'B' respectively is shown in Figure 2.

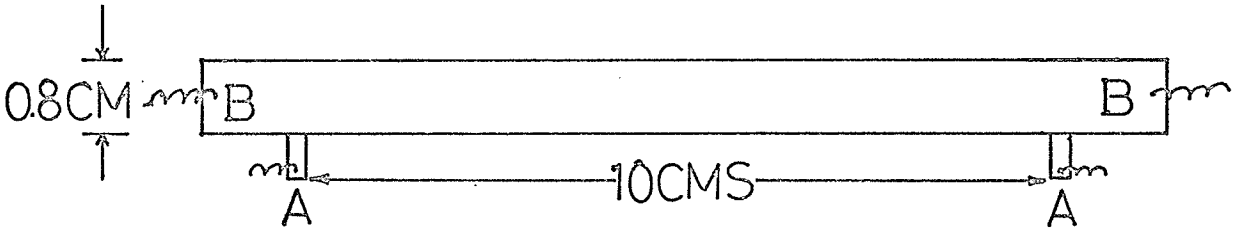

FIG 2 RESISTIVITY SPECIMEN

These specimens with the leads were cleaned again and sealed into a silica tube after flushing it three times with Argon. After a variety of heating times at 500°C, it was established that a twenty minute anneal at 500°C gave a grain size of 42.0×10^{-4} cm (comparable to a grain size of 43.0×10^{-4} cm for specimen 1A of the earlier RLS work in this laboratory[13]). Thus a batch of twenty-five specimens were annealed at 500°C for twenty minutes and air cooled to room temperature.

2.3 Grain Size Measurement and Optical Micrographs

Five of the annealed specimens, taken out at random, were electropolished and etched in a solution of 23 pct perchloric acid and 77 pct acitic acid at 22 and 14 volts respectively. The grain size was determined by the 'planimetric' method and an average value was found to be 41.5×10^{-4} cm.

It was also found that the grains were fully recrystallized as shown in Figure 3.

2.4 Thin Foil Preparation

The specimens were thinned down by electropolishing using the duel jet technique. An electrolyte containing 48 pct ortho-phosphoric acid, 32 pct sulphuric acid and 20 pct water was found to give the best results for pure nickel (99.98 pct). A potential of 5 volts, a current density of 0.2 - 0.3 amp./cm^2 and the jet flow at a setting of 6-7 on the Astromet dual jet polisher was found to give the best thinning conditions.

FIG 3 REPRESENTATIVE PHOTOMICROGRPH
OF RECRYSTALLIZED NICKEL

For preparing thin foils, specimen lengths of about 1.5 cms were cut by electro-thinning and laquered, leaving about 2 cm^2 area as the window. A polishing time of about 12 to 15 minutes was required to obtain suitable thin foils which was determined by the first appearance of a hole at the centre of the foil. The foil was then washed first with distilled water and subsequently with ethyl alcohol and dried. A rectangular area was cut around the hole using a razor blade and this foil was put into the specimen holder sandwiched between two specimen grids. After this, the foil was ready for the examination in a Philips EM-300 electron microscope. All the specimens were examined at $-130^{o}C$ to avoid heating from the electron beam.

2.5 Resistance Measurement

The resistance was measured by a Guildline Type 9920 D.C. Comparator Bridge a brief description of which is given below:

2.5.1 Direct Current Comparator Bridge

Conventional measurement methods of low value four terminal resistors involve a comparison of voltage drops when the same current passes through both resistors. The ratio of resistance is obtained from the ratio of voltages. This applies in a potentiometric comparison of resistors or in a conventional bridge configuration such as the Kelvin bridge.

In the potentiometric method, at balance no current flows in the measuring leads and the lead resistance is therefore unimportant. Resolution and accuracy are limited by (and cannot

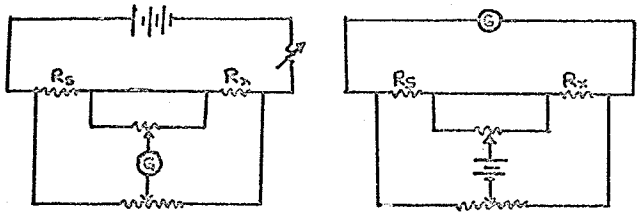

FIG. 4a KELVIN BRIDGE FIG. 4b CONJUGATE KELVIN BRIDGE

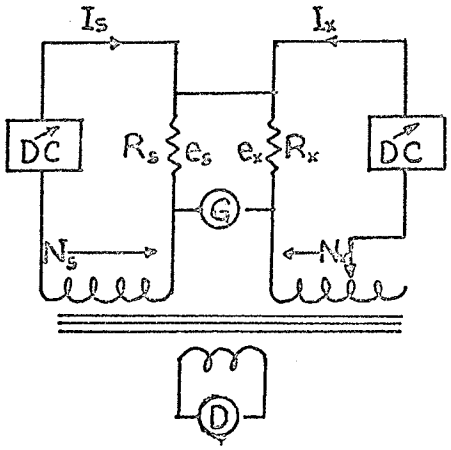

FIG. 4c D.C. COMPARATOR BRIDGE BASIC OPERATION

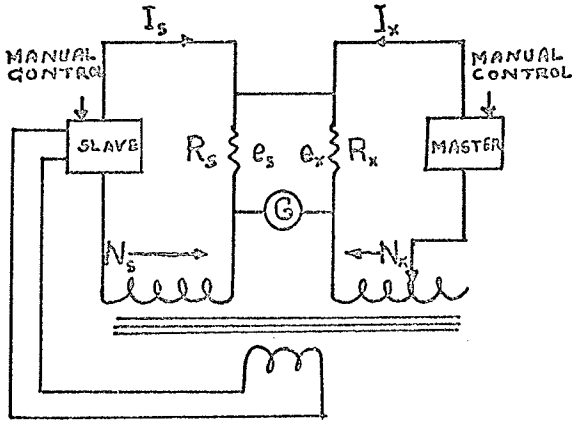

FIG. 4d D.C. COMPARATOR BRIDGE AUTOMATIC AMPERE-TURN BALANCE

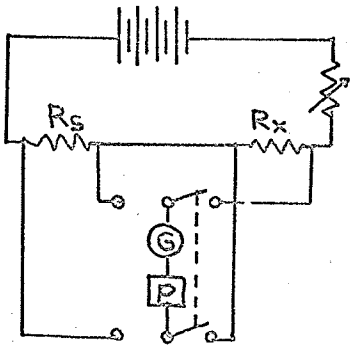

FIG. 4e POTENTIOMETER

FIG. 4(a-e)

be better than) the stability of the currents in the tested resistors and in the potentiometer.

On the other hand, the Kelvin bridge is sensitive to the resistance of the measuring leads but current stability is unimportant. Both potentiometric and Kelvin bridge methods suffer from the disadvantage that when scaling resistors in decade steps the same current must be passed through both resistors and the greatest power is dissipated in the largest resistance.

The new D.C. Comparator bridge is not sensitive to measuring lead resistance, it does not require current stability and when scaling resistors the greatest power is dissipated in the smallest resistance.

In the conventional Kelvin bridge, Figure 4a, the same current is passed through both resistors and the resulting voltage drops are in the same ratio as the resistance values. The resistance ratio is obtained from the voltage ratio. In the conjugate Kelvin bridge, Figure 4b, which is obtained by interchanging the positions of the current source and the detector, different currents flow in the two resistors to produce equal and opposite voltage drops. The ratio of resistors can now be obtained from the ratio of currents if a suitable device is available for measurement of the current ratio. The Direct Current Comparator is such a device.

2.5.2 Basic Operation

The two resistors to be compared are supplied from different current sources (Figure 4c) and the ratio of the two currents is measured when the voltage drop across the two resistors

are equal and opposite. One or both of the direct current sources can be adjusted until the voltages across the two resistors are equal. This balance condition is indicated by the galvonometer G. The current comparator is then used to obtain the ampere-turn balance between the primary and secondary windings by adjustment of the variable turns Nx until zero d.c. flux exists in the core. This zero flux condition is sensed by the detector D.

When G = 0,

$$e_s = e_x$$

$$I_s R_s = I_x R_x$$

$$\frac{R_x}{R_x} = \frac{I_s}{I_x} \qquad 2.5.2.1$$

Where:

e_s = Potential across standard resistor 'R_s'

e_x = Potential across unknown resistor 'R_x'

I_s = Current through standard resistor

I_x = Current through unknown resistor

When detector D indicates zero d.c. flux in the core:

$$I_s N_s = I_x N_x$$

$$\frac{I_s}{I_x} = \frac{N_x}{N_s} \qquad 2.5.2.2$$

Where:

N_s = No. of turns in standard winding

N_x = No. of turns in variable winding

From 2.5.2.1 and 2.5.2.2

$$\frac{R_x}{R_s} = \frac{I_s}{I_x} = \frac{N_x}{N_s}$$

and

$$R_x = \frac{N_x}{N_s} R_s \qquad 2.5.2.3$$

Which gives facilities of a ratio bridge. The D.C. Comparator bridge can also be made to read directly in ohms.

This simple bridge would have the disadvantage of requiring simultaneous manual balances for both voltage and ampere-turns. In such an arrangement highly stable current supplies would be essential.

In a practical form of the bridge (Fig. 4d) the requirement for two simultaneous balances and the need for stable supplies are eliminated by making the ampere-turn balance automatic. The output from the detector winding is used to control the current in the core, i.e. an ampere-turn balance, is maintained.

The only manual balancing operation now required is adjustment of the primary turns dial until the primary and secondary currents produce equal voltages across the compared resistors as indicated by the galvanometer 'G'.

At balance, no current flows in the potential leads and the Direct Current Comparator Bridge thus possesses the principal advantage of the potentiometric system but, at the same time, because of the automatic ampere-turns balance, there is no necessity for current stability. In addition to having the advantages of both the potentiometric and bridge methods, the Direct Current Comparator Bridge has a unique advantage in that the ratio of power dissipation in the compared resistors is the inverse of the ratio of resistance.

2.5.3 Power Dissipation in the Compared Resistors

In the potentiometric and Kelvin bridge methods of comparison of resistors the same current flows through both (Figs. 4(a, b and c)).

$$P_s = I^2R_x \text{ and } P_x = I^2R_x$$

The ratio of power is:

$$\frac{P_s}{P_x} = \frac{I^2R_s}{I^2R_x} = \frac{R_s}{R_x} \qquad 2.5.3.1$$

The greatest power is dissipated in the largest resistance. The comparison of a one ohm standard and 0.1 ohm resistor at 1 ampere using a Kelvin bridge or potentiometric method would involve the dissipation of 1 watt in the 1 ohm resistor and 0.1 watt in the 0.1 ohm.

In the Direct Current Comparator Bridge different currents flow in the two resistors to produce the same voltage across each:

$$P_s = \frac{E_s^2}{R_s} \quad \text{and} \quad P_x = \frac{E_x^2}{R_x}$$

$$\frac{P_s}{P_x} = \frac{R_x}{R_s} \qquad 2.5.3.2$$

The greatest power is now dissipated in the smallest resistance. In the comparison of a 1 ohm standard and a 0.1 ohm resistor, with 1 ampere in the 0.1 ohm to produce 0.1 volt there would be only 0.1 ampere in the 1 ohm standard. The power dissipation in the 0.1 ohm would still be 0.1 watt, but the power in the standard would be reduced to 0.01 watt. Under these conditions the power is dissipated in the resistor which is designed to handle power.

By means of a series of measurements at different current levels which would produce power in the standard insufficient to cause self-heating errors, the power co-efficient characteristics of a heavy current resistor or shunt can be investigated. Such measuring conditions have not previously been available.

2.5.4 Direct Reading Facility and Sensitivity

The 1000 turns on the unknown (primary) side of the bridge can be subdivided in steps of 1 part in 10^7 of full scale. On the standard (secondary) side the 1000 turns fixed winding can be modified by addition of 11.111, 0 turns in either polarity. This range of adjustment is ±1.111, 10% in steps of 1 part in 10^7 and is used to dial into the bridge the known deviation from nominal of the standard resistor. When this known becomes direct reading in ohms.

$$R_s = Ro\ (1+\Delta s)$$

Where: R_s = resistance of standard

Ro = nominal value

Δs = deviation of R_s from nominal in proportional parts

also $N_s = 1000\ (1+\eta_s)$

Where: N_s = standard turns

η_s = adjustment to N_s

From equation 2.5.2.3

$$R_x = \frac{N_x}{N_s}\ R_s$$

or $$R_x = \frac{N_x}{1000}\ \frac{Ro(1+\Delta s)}{(1+\eta s)}$$

If η_s is made equal to Δs

$$R_x = \frac{N_x}{1000} \quad Ro$$

and the bridge is direct reading in terms of nominal value of the standard.

For the scaling of decade values of resistance when heavy current capability is required on the unknown (primary) side, the first three decades are replaced by fixed windings of 100, 10 or 1 turn. So that the lower four decades will retain their resolution of parts in 10^7 they are switched over to the standard side where they work in conjunction with the 100 fixed turns N_s to provide an adjustment range of ±1.111.0 turns, which is equivalent to ±0.111,0 turns, which is equivalent to ±0.111, 10% with resolution of 1 part in 10^7.

A reversing switch simultaneously reverses the current in both resistors and the comparator and the effect of thermal emfs in the resistors and the galvanometer are eliminated from the balance.

The limit of sensitivity of the bridge is defined by the noise level, which is about 3 microampere-turns. When the bridge is used (as is normal) at the 1000 ampere-turn level, this noise corresponds to 3 parts in 10^8 of full scale.

Voltage balance sensitivity depends on the galvanometer G which is a photocell amplifier with a sensitivity of 0.01 microvolts. With 1 volt across the tested resistors this is equivalent to 1 part in 10^8.

The principal source of error in most types of bridge is in the linearity of the resistors in the measuring dials. In the D.C. Comparator bridge the linearity depends not on resistors but on a turns ratio which is of extremely high accuracy. Errors in linearity are less than 1 part in 10^7 of full range. This quality of linearity applies to the first three decades. The linearity of the fourth and subsequent dials also depends on an accurate number of turns, but interdial agreement depends on resistance ratio as the only practical method of achieving the effect of fractional turns. However, the fourth decade requires an accuracy of only 1 in 10^4 to equal the full scale accuracy of the bridge and this is not difficult to achieve.

In the D.C. Comparator bridge, therefore, we have a low range (up to 1000 ohms for 7 figure resolution) resistance bridge which contains no critical resistors, has no significant long term drift, is accurate to better than 1 part in 10^7 of full range and in which measuring lead resistance and variation in lead resistance are completely unimportant. There is no need for current stability and thermal emfs are eliminated. The bridge is permanently accurate.

3. RESULTS

3.1 Resistivity

3.1.1 Theory

The electrical resistivity of pure metals is increased by the introduction of impurities and defects into the lattice[14]. In accord with modern theoretical concepts and most experimental observations, Matthiessen's rule states that the electrical resistivity of a metal, ρ, is equal to the sum of the lattice resistivity due to thermal vibrations, ρi, and a temperature independent component (residual resistivity) due to defects, ρo. If for reasonable variations in the concentration of defects, $\frac{d\rho}{dT}$ (i.e., temperation derivative of resistivity) is not constant, Matthiessen's rule does not hold.

The residual resistivity is very sensitive to the presence of imperfections because any distrubance of the ideally periodic lattice results in scattering of the conduction electrons and hence an increase in the electrical resistance. At low defect concentrations one expects the increase in the residual resistivity to be proportional to the concentration of defects, since the interference among the various defects can be neglected. The change in the residual resistivity is therefore an appropriate and convenient measure of the defect concentration in metals. The change in the thermal component of the resistance depends upon the change in the vibrational spectrum in the solid caused by the presence of the defect. Since the defect contribution to the thermal component is not well known (although known to be small)

and is difficult to estimate theoretically, measurements are usually made at a sufficiently low temperature to avoid the problem.

For our purpose the imperfections can be divided into two groups: point imperfections (vacancies, impurities, interstitials) and line and planar imperfections (dislocations, stacking faults, grain boundaries). All these scatter electrons to a varying degree.

Plastic deformation of metals usually causes an increase, $\Delta\rho$, in the electrical resistivity which can be divided into two parts of roughly equal magnitude:

$$\Delta\rho = \Delta\rho_V + \Delta\rho_D$$

where $\Delta\rho_V$ = Resistivity increase due to point defects

and $\Delta\rho_D$ = Resistivity increase due to line and planar defects

$\Delta\rho_V$ disappears after annealing at temperatures where point defects can diffuse but $\Delta\rho_D$ remains until recrystallization occurs and is ascribed to the scattering of electrons by dislocations.

Stacking faults associated with partial dislocations in extended dislocations may make significant contributions to the resistivities of some deformed metals and alloys[15]. From elementary considerations, Klemens[16] has deduced that their effect might be large as compared to that of dislocations. However, brief accounts of calculations by Tweedale[17] and by Blatt, Ham and Koehler[18] suggest that stacking faults make no significant contribution to the resistivity of dislocations in copper.

3.1.2 Results

The dimensions of the various specimens used for resistivity measurements, electron microscopy and tensile testing are given in Table 2.

Table 2

Specimen No.	Specimen width mms	Specimen thickness mm	Specimen potential Lead separation cms.	Cross-sectional area mm^2	Cross-sectional area $in^2 x10^3$	Comments
1	8.00	0.132	9.25	1.06	1.64	Specimens 1 to 5 were used for resistivity and electron microscopy.
2	8.00	0.122	10.00	0.98	1.52	
3	7.88	0.129	10.00	1.02	1.58	
4	8.05	0.121	9.95	0.97	1.50	
5	8.2	0.120	9.45	0.98	1.52	
6	8.2	0.128	9.55	1.05	1.63	Specimens 6 to 11 were used for the tensile test experiments
7	8.00	0.132	9.85	1.06	1.64	
8	8.18	0.132	9.90	1.08	1.67	
9	7.95	0.142	9.86	1.13	1.75	
10	7.88	0.131	10.00	1.03	1.60	
11	7.93	0.137	10.00	1.09	1.69	

The results of resistance measurements both at room and liquid nitrogen temperatures are shown in Table 3.

Specimens 1 to 5 with 'Budd Metalfilm' strain gauges (Type C6-121 A) attached to them with Budd 'GA-1' contact cement were deformed in tension to strain values of $1.0x10^{-4}$, $2.0x10^{-4}$, $3.0x10^{-4}$, $6.0x10^{-4}$ and 45.0×10^{-4} respectively. Immediately after deformation the specimens were immersed in liquid nitrogen to retain the point defects produced during tensile deformation. All resistance measurements were carried out at liquid nitrogen temperature.

Table 3

R_x = Specimen Resistance

Specimen No	Specimen Condition	S. No. of observations	Standard Resistance R_s (ohms)	(R_x/R_s) at room temp. maintained at 19°C	(R_x/R_s) at Liq. N_2 temp.	Average (R_x/R_s) at 19°C	Average (R_x/R_s) at Liq. N_2 temp.
1	Annealed	1	0.01	0.6537002	0.0557399		
"	at 500°C	2	0.01	0.6536202	0.0557399		
"	for 20	3	0.01	0.6537002	0.0557399	0.6536834	0.0557399
"	minutes	4	0.01	0.6537000	0.0557399		
"	"	5	0.01	0.6536966	0.0557399		
2	"	1	0.01	0.7183466	0.0615199		
"	"	2	0.01	0.7183466	0.0615199		
"	"	3	0.01	0.7183466	0.0615199	0.7183426	0.0615199
"	"	4	0.01	0.7183366	0.0615199		
"	"	5	0.01	0.7183366	0.0615199		
3	"	1	0.01	0.6819449	0.0579400		
"	"	2	0.01	0.6819449	0.0579400		
"	"	3	0.01	0.6819649	0.0579400	0.6819549	0.0579400
"	"	4	0.01	0.6819549	0.0579400		
"	"	5	0.01	0.6819649	0.0579400		
4	"	1	0.01	0.7188369	0.0614623		
"	"	2	0.01	0.7188999	0.0614623		
"	"	3	0.01	0.7188999	0.0614623	0.7188920	0.0614623
"	"	4	0.01	0.7188999	0.0614623		
"	"	5	0.01	0.7188999	0.0614623		
5	"	1	0.01	0.6724200	0.0585000		
"	"	2	0.01	0.6724200	0.0585000		
"	"	3	0.01	0.6724200	0.585000	0.6724200	0.0585000
"	"	4	0.01	0.6724200	0.0585000		
"	"	5	0.01	0.6724200	0.0565000		

After resistance measurements of the deformed specimens, each specimen was step aged at room temperature and its resistance measured till further ageing produced no changes in resistivity. The first three ageing periods were of five minutes duration and for subsequent steps the ageing time was gradually increased. Data showing resistance changes during room temperature ageing of deformed specimens are given in Table 4.

A typical plot, showing resistnace change with ageing time for the data of specimen 3 in Table 4, is shown in Fig. 7a.

Table 4

Ra = Resistance in the annealed condition at liq. N_2 temperature

Rd = Resistance in the deformed condition at liq. N_2 temperature

Sp. No.	Tensile Strain x10^4	Cummulative Ageing time	Ra in ohms	Rd in ohms	Rd-Ra in ohms	$\frac{(Rd-Ra)}{Ra} \times 100$ pct resistance change
1	1.0	0	0.000557399	0.000558099	0.000000700	0.12558
"	"	5-min.	"	0.000557999	0.000000600	0.10764
"	"	10-min.	"	0.000557999	"	0.10764
"	"	15-min.	"	"	"	0.10764
"	"	30-min.	"	"	"	0.10764
"	"	2-hrs.	"	0.000557799	0.000000400	0.07176
"	"	3-hrs.	"	"	"	"
"	"	4-hrs.	"	0.000557599	0.000000200	0.03588
"	"	5-hrs.	"	0.000557399	0.00	0.00
"	"	23-hrs.	"	"	"	"
"	"	51-hrs.	"	"	"	"
2	2.0	0	0.000615199	0.000616399	0.000001200	0.19505
"	"	5-min.	"	0.000616199	0.000001000	0.16252
"	"	10-min.	"	"	"	"
"	"	15-min.	"	"	"	"
"	"	30-min.	"	"	"	"
"	"	1-hrs.	"	"	"	"
"	"	2-hrs.	"	"	"	"
"	"	15-hrs.	"	"	"	"
"	"	19-hrs.	"	"	"	"
"	"	38-hrs.	"	0.000615199	0.0	0.0
"	"	65-hrs.	"	"	0.0	0.0
3	3.0	0	0.000579400	0.000580500	0.000001100	0.18985
"	"	5-min.	"	"	"	"
"	"	10-min.	"	"	"	"
"	"	15-min.	"	"	"	"
"	"	30-min.	"	0.000580400	0.000001000	0.17259
"	"	1-hrs.	"	0.000580100	0.000000700	0.12081
"	"	2.5-hrs.	"	0.000579800	0.000000400	0.06903
"	"	25.5-hrs.	"	0.000579400	0.0	0.0
"	"	27.5-hrs.	"	"	"	"
"	"	45.0-hrs.	"	"	"	"
4	6.0	0	0.000614623	0.000616799	0.000002176	0.35403
"	"	5-min.	"	"	"	"
"	"	10-min.	"	0.000616699	0.000002076	0.33776
"	"	15-min.	"	0.000616599	0.000001976	0.32149
"	"	30-min.	"	0.000616499	0.000001876	0.30522
"	"	1-hrs.	"	"	"	"
"	"	2-hrs.	"	0.000616199	0.000001576	0.25641
"	"	3-hrs.	"	0.000615899	0.000001276	0.20760
"	"	19-hrs.	"	0.000615499	0.000000876	0.14252
"	"	23-hrs.	"	0.000615199	0.000000576	0.09371
"	"	26-hrs.	"	0.000614799	0.000000176	0.02863
"	"	29-hrs.	"	"	"	0.02863
"	"	43-hrs.	"	"	"	"

Table 4 Continued

Sp. No.	Tensile Strain x10^4	Cummulative Ageing time	Ra in ohms	Rd in ohms	Rd-Ra in ohms	$\frac{(Rd-Ra)}{Ra} \times 100$ pct resistance change
5	45.0	0	0.000585000	0.000594300	0.000009300	1.58974
"	"	5-min.	"	0.000594200	0.000009200	1.57264
"	"	10-min.	"	0.000594100	0.000009100	1.55555
"	"	15-min.	"	"	"	"
"	"	30-min.	"	"	"	"
"	"	1-hrs.	"	0.000594000	0.000009000	1.53846
"	"	2-hrs.	"	0.000593800	0.000008800	1.50427
"	"	14-hrs.	"	0.000592200	0.000007200	1.23076
"	"	21-hrs.	"	0.000591600	0.000006600	1.12820
"	"	38-hrs.	"	0.000591600	0.000006600	1.12820
"	"	45-hrs.	"	"	"	1.12820
"	"	63-hrs	"	"	"	"

3.1.3 Interpretation

The total increase in resistivity resulting from tensile plastic strain was found by van Bueren[19] to follow an equation of the form

$$\Delta\rho = c\,\varepsilon^{n} \qquad 3.1.3.1$$

or

$$\frac{\Delta\rho}{\rho} = c^{1}\,\varepsilon^{n} \qquad 3.1.3.2$$

Where c is a constant, ε is the permanent strain, n is a constant between zero and two, and $c^{1} = \frac{c}{\rho}$. To calculate the value of n for nickel, the percentage change in resistivity was calculated from the data given in Table 4 and is listed in Table 5. The percentage change in resistivity with tensile strain is shown in Fig. 5.

Table 5

Sp.No.	Strain x 10^{4}	Total Change in Resistance x 10^{10} in ohms	Percentage Change in Resistance
1	1.0	6.438	0.13
2	2.0	11.664	0.20
3	3.0	11.253	0.19
4	6.0	20.256	0.35
5	45.0	98.000	1.59

The least square fit for a straight line for the experimental data given in Table 5 as shown in Fig. 6 gives the following relationship:

$$\frac{\Delta\rho}{\rho} = 0.5 \times \varepsilon^{0.66} \qquad 3.1.3.3$$

and

$$\Delta\rho = 3.5\times10^{-6} \times \varepsilon^{0.66} \qquad 3.1.3.4$$

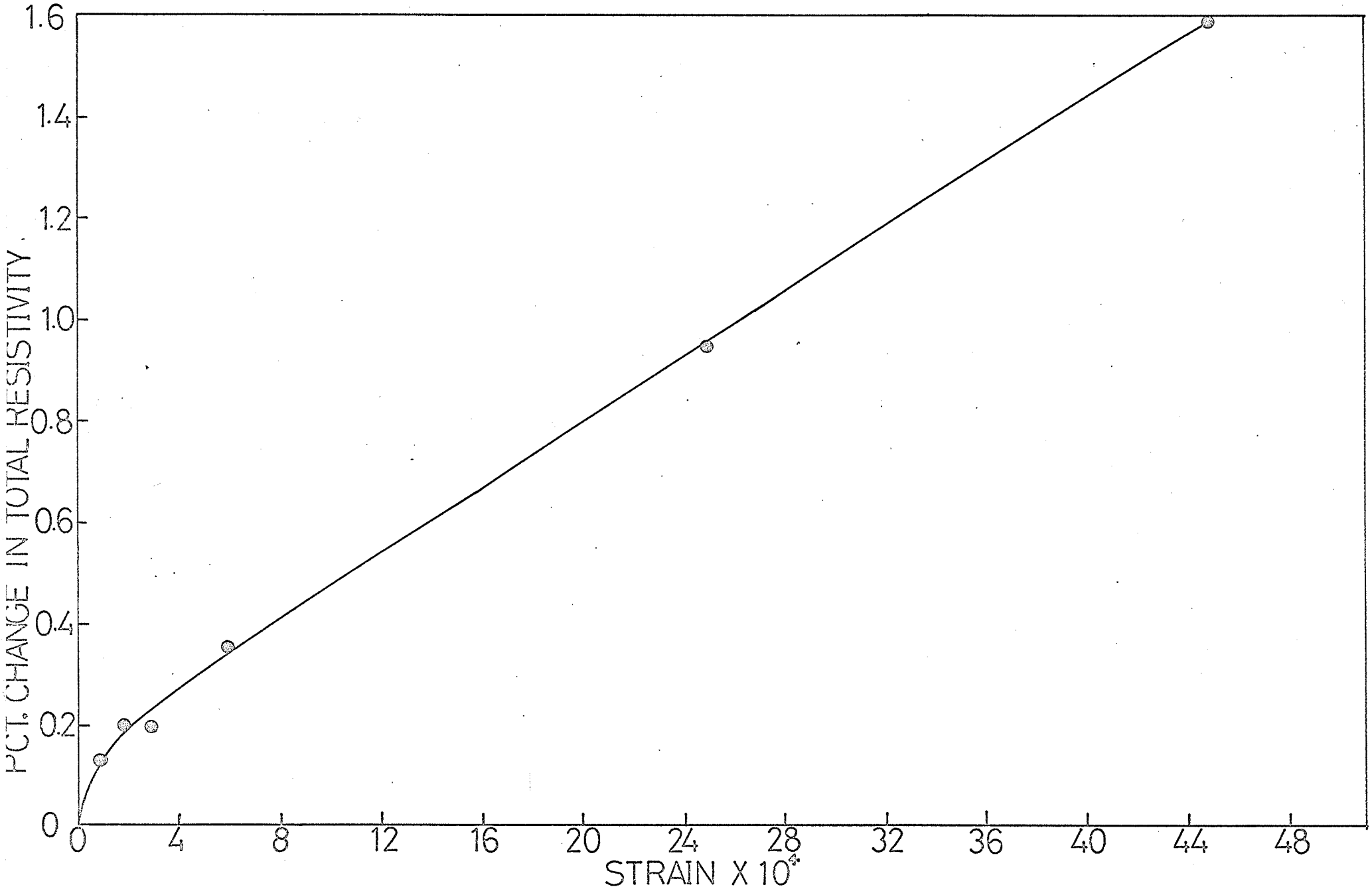

FIG. 5 PERCENTAGE CHANGE IN RESISTANCE AFTER TENSILE DEFORMATION VS TOTAL STRAIN

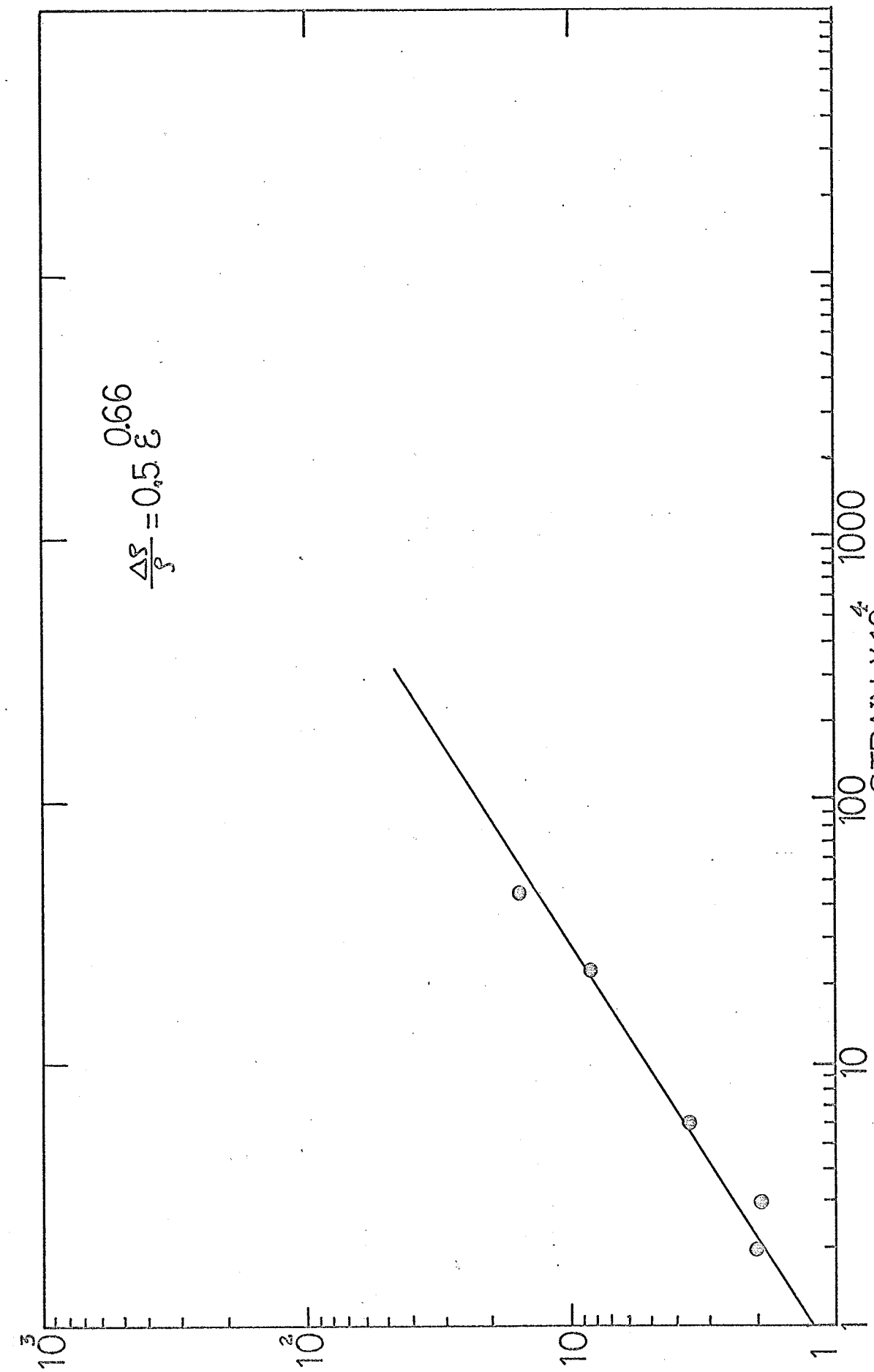

FIG.6 FRACTIONAL CHANGE IN RESISTANCE AFTER TENSILE DEFORMATION VS TOTAL STRAIN

Martin et al.[20] found 'n' to be 1.38 for 99.999 pct pure nickel and 5.29×10^{-7} ohm-cm as to be the value for c. Comparing with our data, it is seen that at low strains the change in resistance per unit strain is less as compared to that at higher strains[20] (more than 1 pct). This suggests that in the initial stages of deformation process less defects (point and line) are created because there are less number of sources responsible for their generation. With increased tensile strain these results show increased dislocation activity and more of point and line defect generation. When this has happened the rate of defect production will increase, which is apparent from the higher value of 'n' after 1 pct deformation as obtained by Martin et al.[20].

The room temperature ageing data (percentage change in resistivity vs time) are plotted in Figs. 7(b-f) for different amounts of tensile straining. From these plots the following conclusions may be drawn:

Up to a strain of 3.0×10^{-4} the increase in resistivity due to deformation is completely recovered by room temperature ageing (Figs. 7 b to d). Beyond this strain, deformation produces a net residual resistivity which is not recovered by room temperature ageing (Figs. 7 e and f).

It is well established that point defects are produced during deformation of a metal. Recently, Kressel et al.[21] have shown that in the initial stages of plastic deformation of up to 1 pct in nickel there is greater production of vacancies than interstitials. Furthermore, a recovery stage, stage III, lying

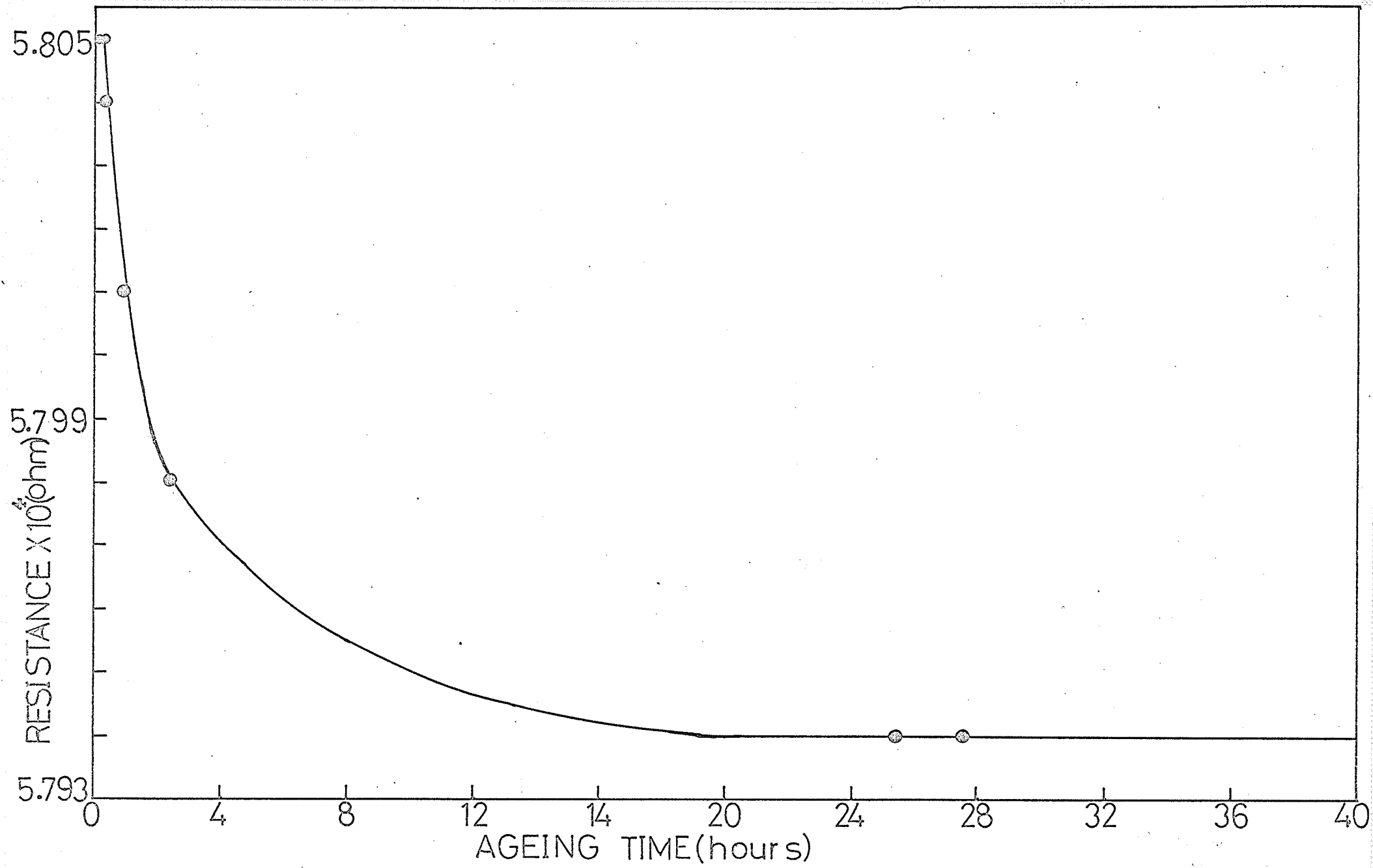

FIG.7a VARIATION IN RESISTANCE DURING AGEING OF DEEORMED POLYCRYSTALLINE NICKEL SPECIMEN VS AGEING TIME

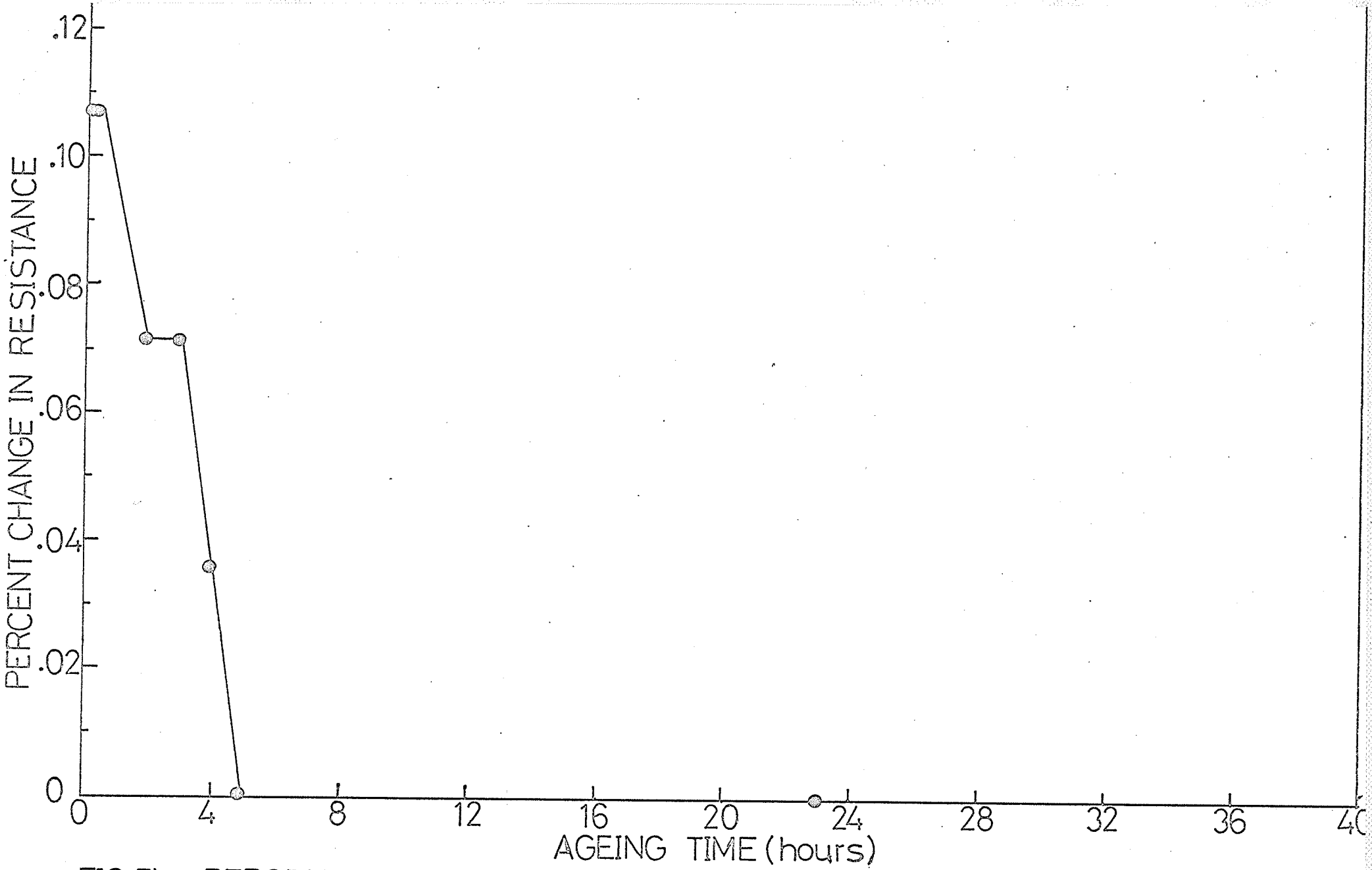

FIG.7b PERCENT CHANGE IN RESISTANCE DURING ROOM TEMPERATURE AGEING OF POLYCRYSTALLINE NICKEL DEFORMED TO 1.0×10^{-4} STRAIN VS AGEING TIME

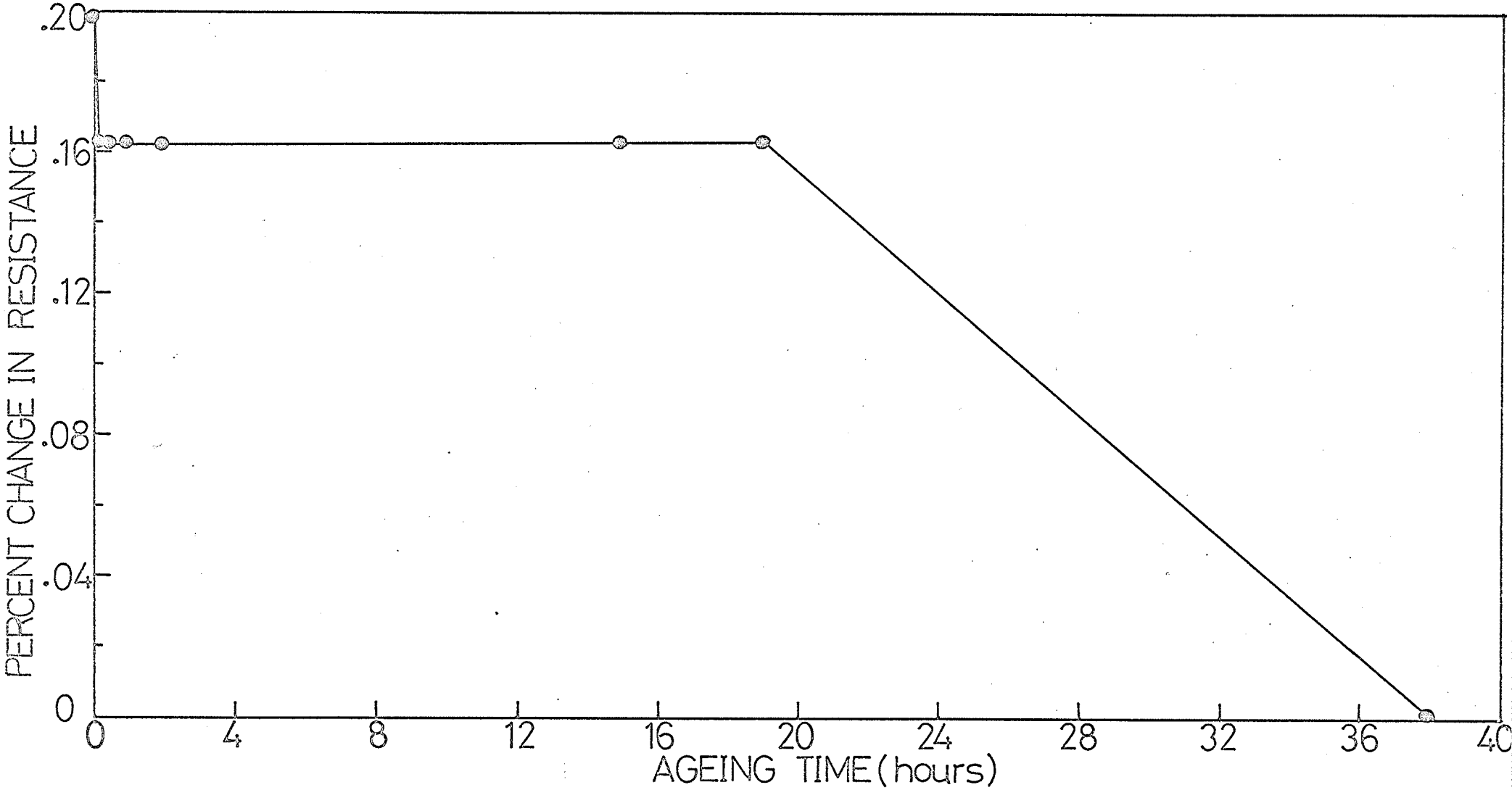

FIG. 7c PERCENT CHANGE IN RESISTANCE DURING ROOM TEMPERATURE AGEING OF POLYCRYSTALLINE NICKEL DEFORMED TO 2.0×10^{-4} STRAIN VS AGEING TIME

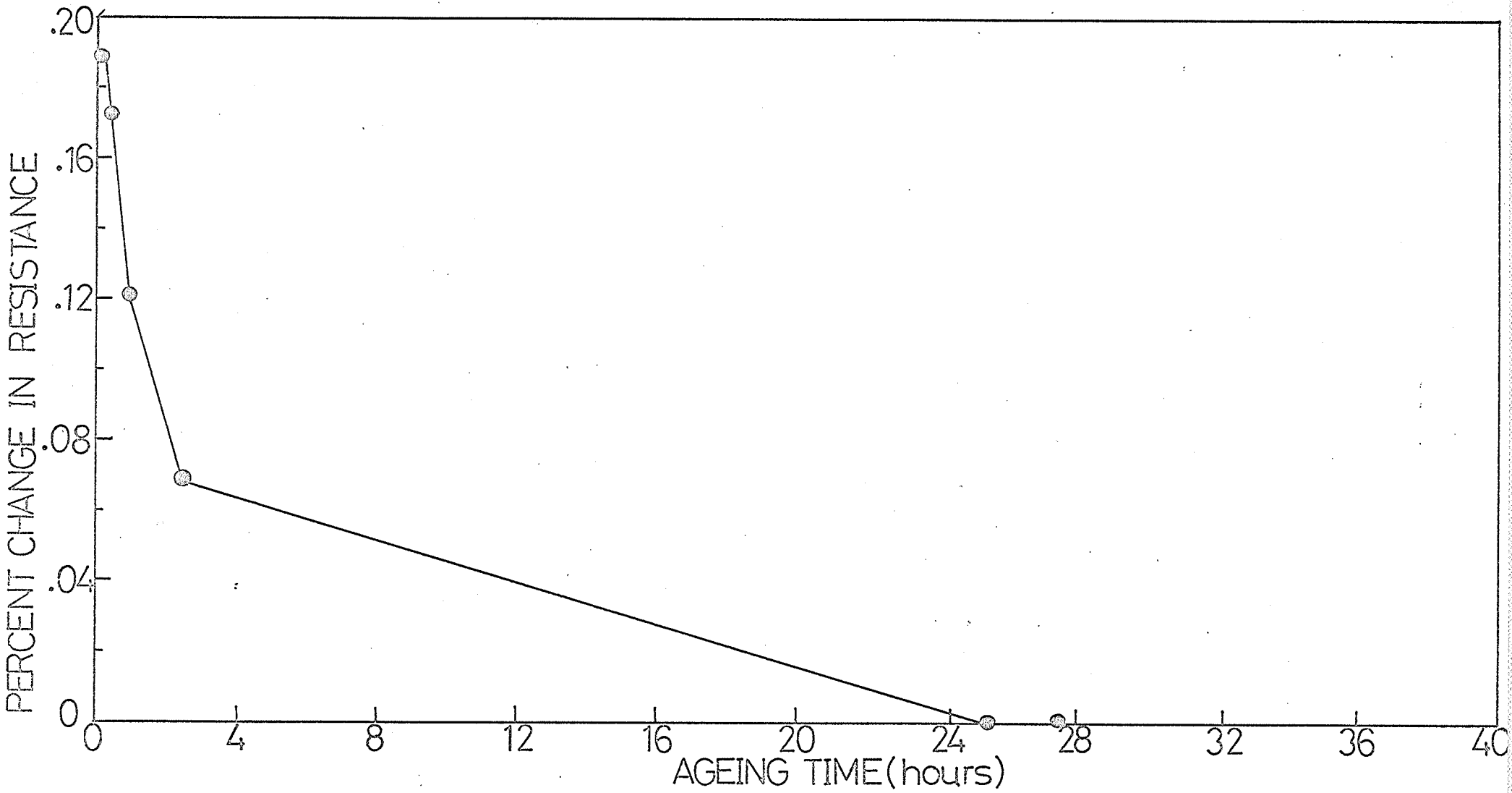

FIG.7d PERCENT CHANGE IN RESISTANCE DURING ROOM TEMPERATURE AGEING OF POLYCRYSTALLINE NICKEL DEFORMED TO 3.0×10^{-4} STRAIN VS AGEING TIME

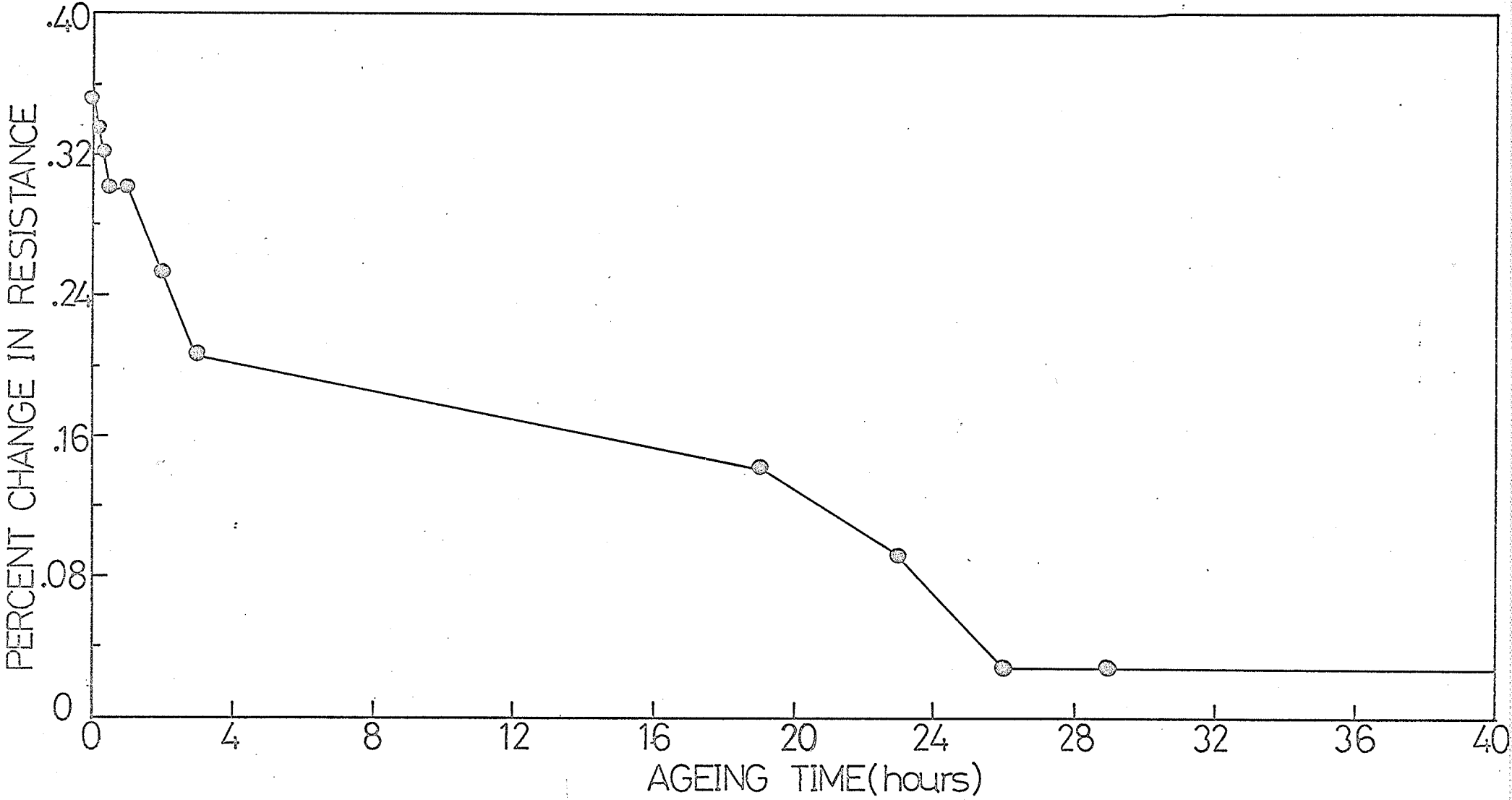

FIG. 7e PERCENT CHANGE IN RESISTANCE DURING ROOM TEMPERATURE AGEING OF POLYCRYSTALLINE NICKEL DEFORMED TO 6.0×10^{-4} STRAIN VS AGEING TIME

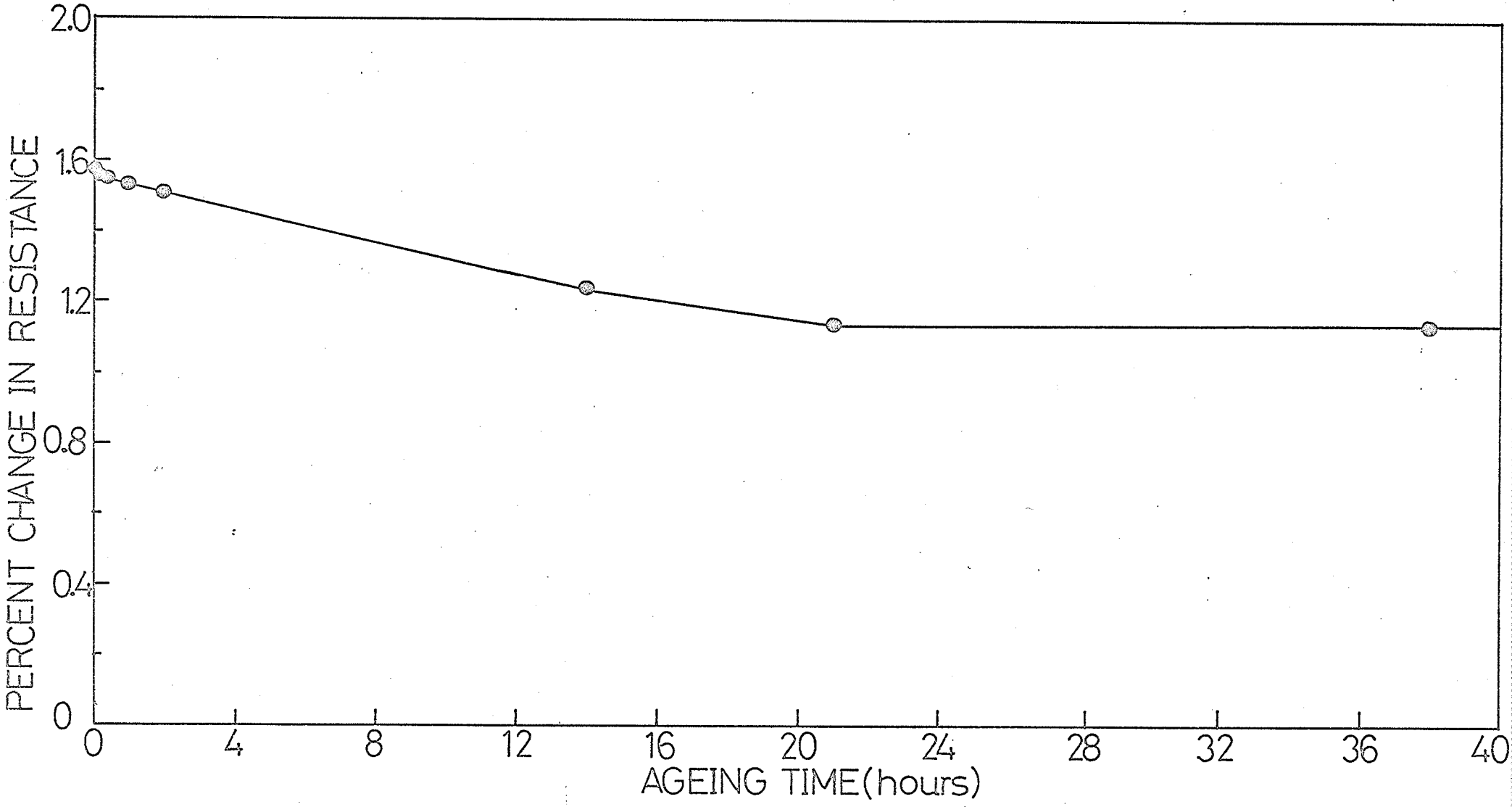

FIG.7f PERCENT CHANGE IN RESISTANCE DURING ROOM TEMPERATURE AGEING OF POLYCRYSTALLINE NICKEL DEFORMED TO 45.0×10^{-4} STRAIN VS AGEING TIME

between -30° and 140°C, which is ascribed primarily to the annihilation of interstitials through recombination with vacancies [22,23], and partly to the migration of a fraction of the interstitials to dislocations[21], has been observed in deformed nickel. In view of the above, the major portion of the non-equilibrium concentration of point defects (essentially vacancies because of lower energy of formation as compared to interstitials) produced during room temperature deformation of nickel is expected to anneal out by room temperature annealing and the residual resistivity left after ageing should be that due to dislocations, stacking faults and unannealed vacancies. After room temperature ageing, all the specimens were aged again at 100°C for 15 minutes to eliminate all of the point defect, but this treatment did not produce any change in resistance. Thus, it may be assumed that all the point defects produced during tensile deformation were annealed out by room temperature ageing and that the residual resistivity was mainly due to dislocations. It is assumed that there is very little contribution of stacking faults to the electrical resistivity due to the very small stacking fault density expected for nickel, which has a high stacking fault energy[24].

Therefore according to the above arguments we can separate the resistivity increase due to point defect (vacancies) and due to that of dislocations. The results are as follows.

Table 6

Specimen No.	Resistivity due to Point Defects		Resistivity due to Dislocations		Strain $x10^4$
	Change in Resistance due to point defects $x10^9$ (ohms)	Change in Resistivity due to point defects $x10^{10}$ (ohms-cm)	Change in Resistance due to dislocations $x\ 10^9$ (ohms)	Change in Resistivity due to dislocations $x10^{10}$ (ohms-cm)	
1	600	6.43	0.0	0.0	1.0
2	1200	11.66	0.0	0.0	2.0
3	1100	11.25	0.0	0.0	3.0
4	1600	15.61	476.0	4.646	6.0
5	2700	28.00	6600.0	70.000	45.0

Seeger[25] found a change of 4.0 micro-ohm-cm in the electrical resistivity for one atomic percent increase in the vacancy concentration in nickel. From this we can calculate the atomic percent of vacancies produced during tensile deformation. The calculated values are tabulated below.

Table 7

Specimen No.	Strain $x\ 10^4$	Atomic pct of Vacancies (cv)$x\ 10^4$
1	1.0	1.61
2	2.0	2.92
3	3.0	2.81
4	6.0	3.90
5	45.0	7.00

A plot of atomic pct vacancies vs strain is shown in Fig. 8. To find the power law the above data were replotted on a log-log scale. The best fit straight line through these points gave the following relationship between atomic pct vacancies (c_v) and strain (ε)

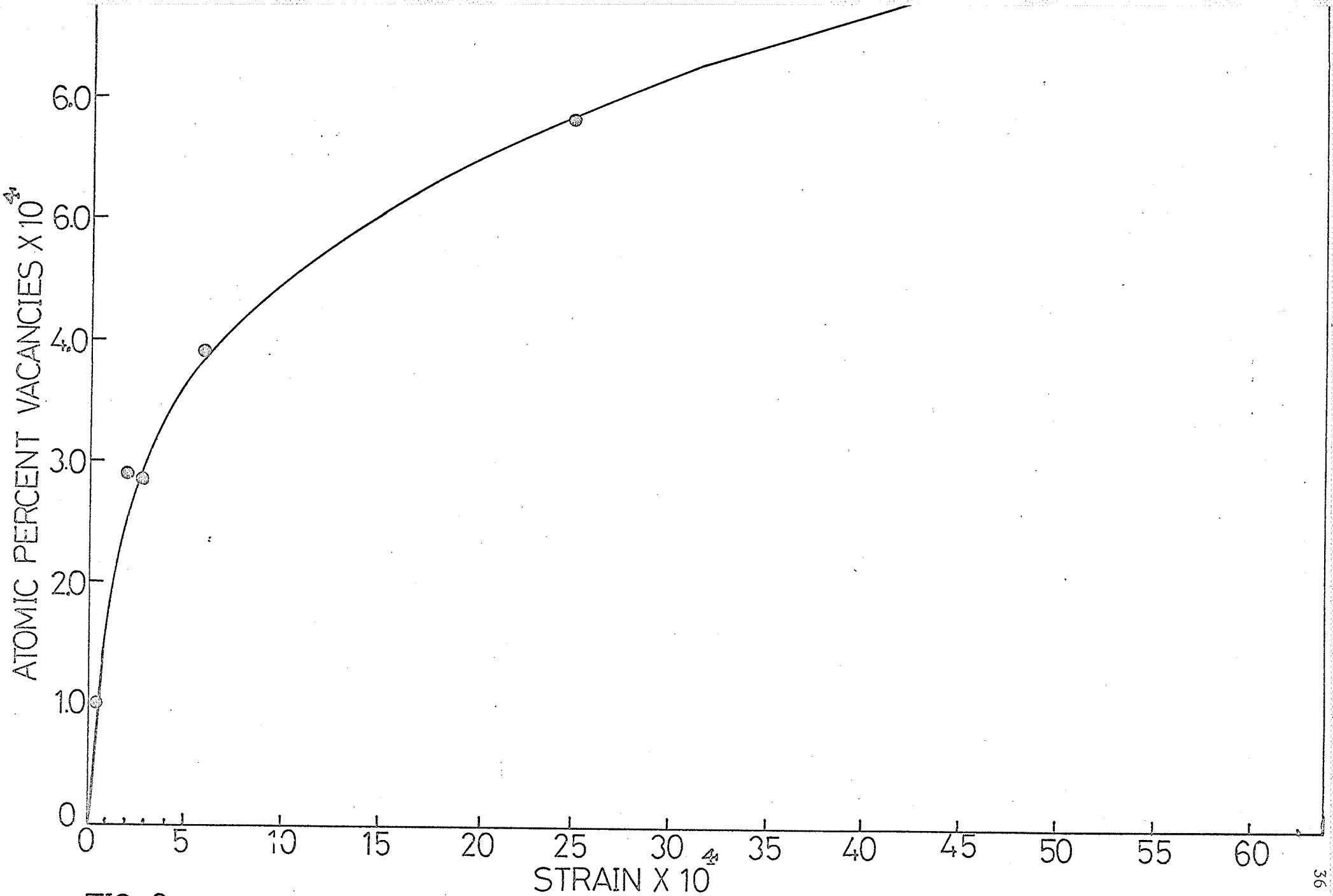

FIG. 8a ATOMIC PERCENT OF VACANCIES VS TOTAL TENSILE STRAIN

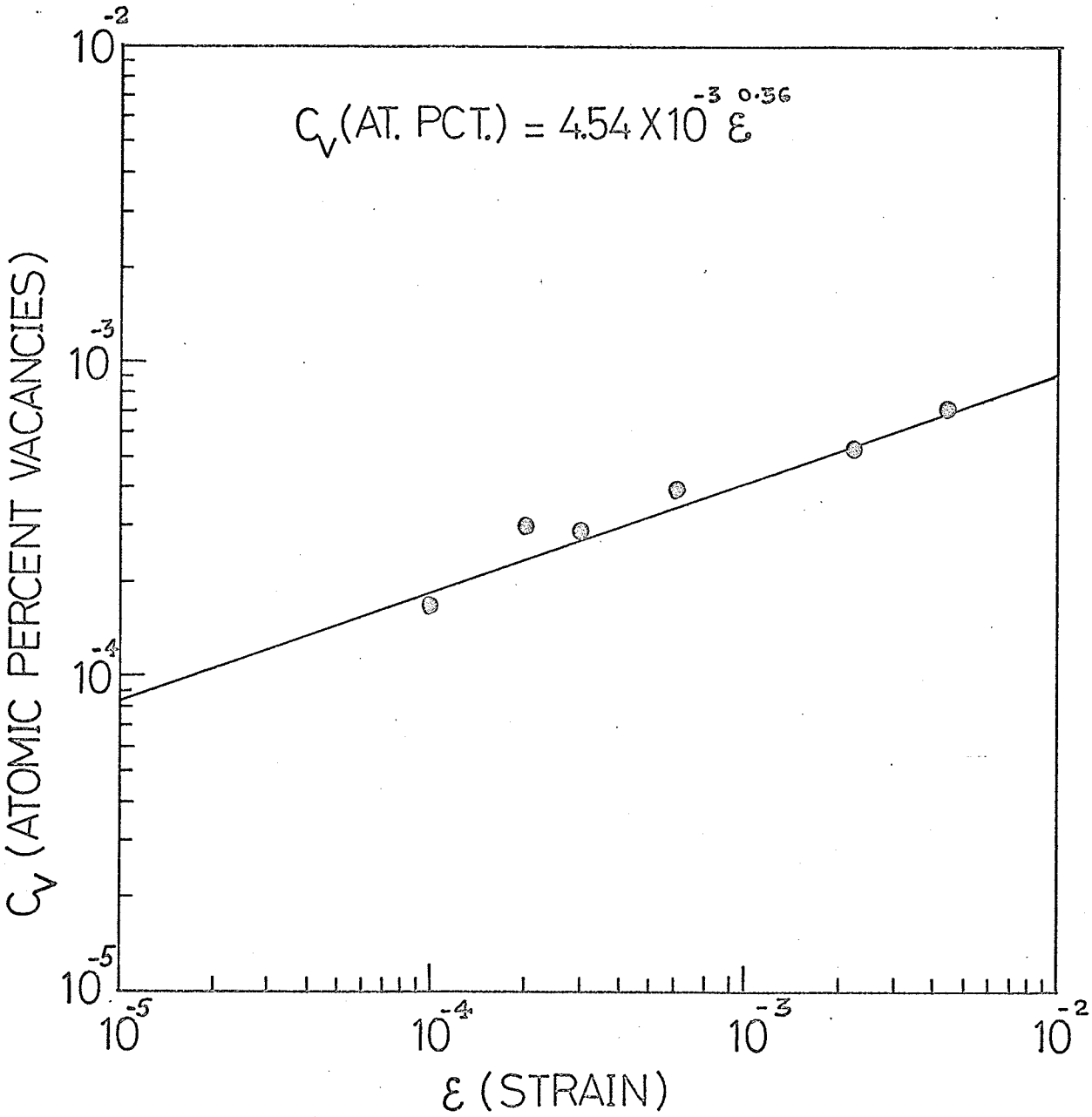

FIG.8b ATOMIC PERCENT OF VACANCIES PRODUCED DURING TENSILE DEFORMATION VS TOTAL TENSILE STRAIN

$$c_v \text{ (atomic pct)} = 4.54 \times 10^{-3} \varepsilon^{0.36} \qquad 3.1.3.5$$

A discussion, based on dislocation interactions, to explain the above equation is presented in section 4.1 after the results of transmission electron microscopy have been presented.

An attempt was made to determine the order of the reactions responsible for the point defects annealing during room temperature ageing of the deformed specimens. It was assumed that point defects are annihilated in such a way as to follow the rate equation of the form given below.

$$\frac{dc}{dt} = -k\, c^{\gamma} \qquad 3.1.3.6$$

where c = Defect concentration

t = Time

k = Rate constant

γ = Order of reaction

Since the rate of point defect annealing $\frac{dc}{dt}$ is proportional to the rate of resistance change $\frac{dR}{dt}$, we can rewrite the above equation in the following manner.

$$\frac{dR}{dt} = -k^1 R^{\gamma} \qquad 3.1.3.7$$

Where k^1 is another constant independent of defect concentration.

The order of reaction 'γ' was determined from a log-log plot (Fig. 8c) between rate of resistance change and the resistance and the results are given in Table 8.

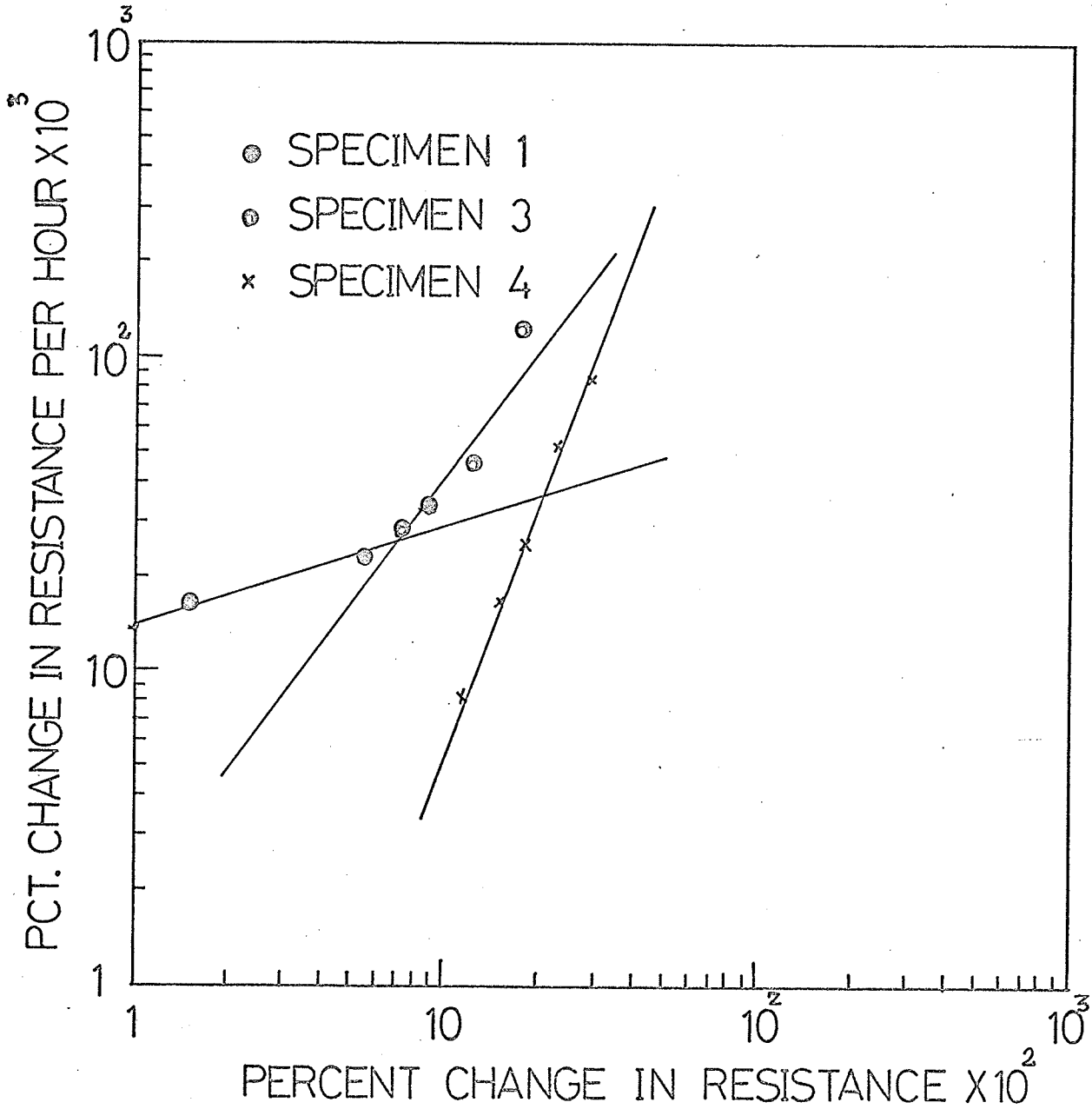

FIG.8c PERCENT CHANGE IN RESISTANCE PER HOUR DURING AGEING OF DEFORMED SPECIMENS VS PERCENT CHANGE IN RESISTANCE

Table 8

Specimen No.	Strain	Order
1	1.0×10^{-4}	0.15
3	3.0×10^{-4}	0.47
4	6.0×10^{-4}	0.57

It is known that the order of a reaction involving only single vacancy migrating to a fixed number of sinks in unity and random annihilation of equal concentration of vacancies and interstitials is described by a second-order reaction. Our data do not correspond to any of the above reactions. The low value of 'γ' in the case of point defects produced in nickel deformed at low strains suggests that there is some slow process responsible for the annihilation of defects. This could not be due to the recombination of vacancies with interstitials because the low activation energy of this process suggests a higher value for 'γ'. From the increase in the order of the reaction with increasing dislocation density it is proposed that point defects may be condensing on to the dislocations.

3.2 Electron Microscopy

3.2.1 General Electron Microscopy

Thin foils from all the specimens after resistance measurements were prepared for micro-structural examination, with the Philips EM 300 electron microscope, as described previously.

3.2.1.1 Results and Interpretation

3.2.1.1.1 An Annealed Condition

Typical electron-micrographs of as recrystallized nickel are shown in Fig. 9(a-d).

Figures 9a and 9b show grain boundaries 'A', annealing twin 'c' originating at grain boundaries and twin boundaries 'B'. Fig. 9c shows the saw-toothed nature of the annealing twin boundary. The majority of the areas are seen to be free from dislocations, suggesting a low dislocation density of as annealed nickel.

It is well known that the annealing twins are produced by the growth of atomic planes during recrystallization. As an intermediate stage of this growth process, microtwins[26] are also known to form (Fig. 9d). This growth process is sometimes hindered (Fig. 9d at E) due to the presence of dislocations (Fig. 9d at D) on the growth planes[26-28]. Similar micro-twins were seen after the growth of metallic thin films on sodium chloride substrates[26-28].

3.2.1.1.2 Deformed and Aged Condition

Specimens were deformed to a strain of 1.0×10^{-4}, 2.0×10^{-4}, 3.0×10^{-4}, 4.0×10^{-4}, 5.0×10^{-4}, 6.0×10^{-4} and 45.0×10^{-4} and were aged until no further change in resistance was detected. Then these specimens were thinned and examined under the electron microscope. The results are as follows.

3.2.1.1.2.1 $\varepsilon = 1.0 \times 10^{-4}$

The electron micrographs of specimens deformed to a strain of 1.0×10^{-4} are shown in Figs. 10(a-g).

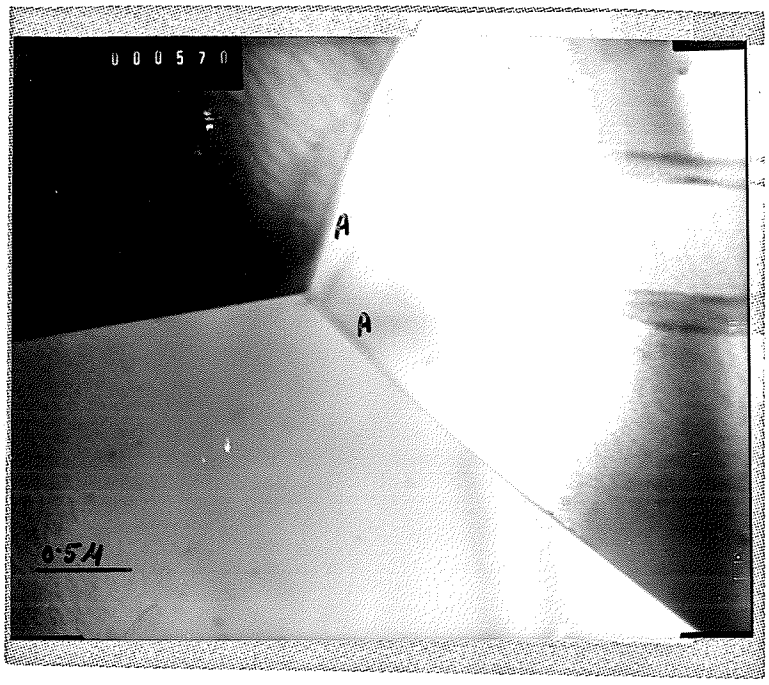

FIG. 9a ELECTRON MICROGRAPH OF RECRYSTALLIZED NICKEL

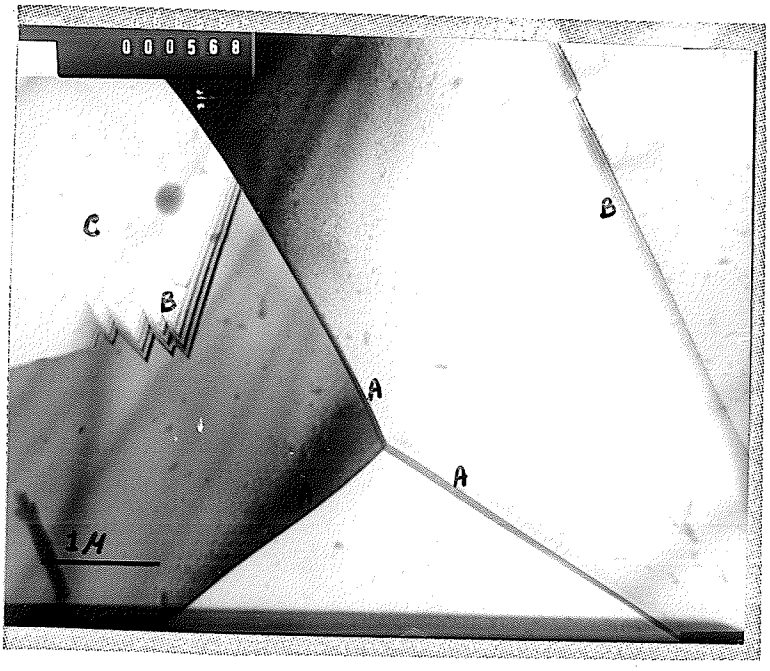

FIG. 9b ELECTRON MICROGRAPH OF RECRYSTALLIZED NICKEL

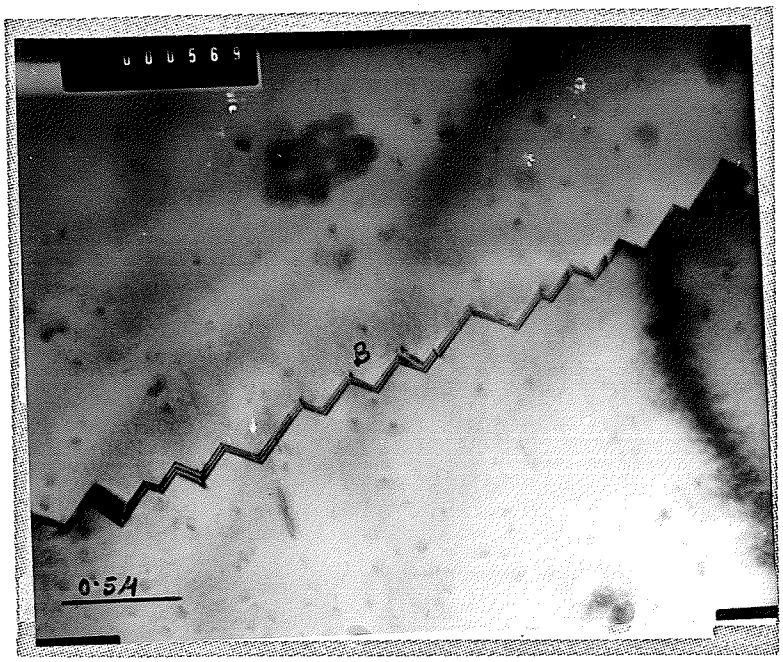

FIG.9c ELECTRON MICROGRAPH OF RECRY-STALLIZED NICKEL

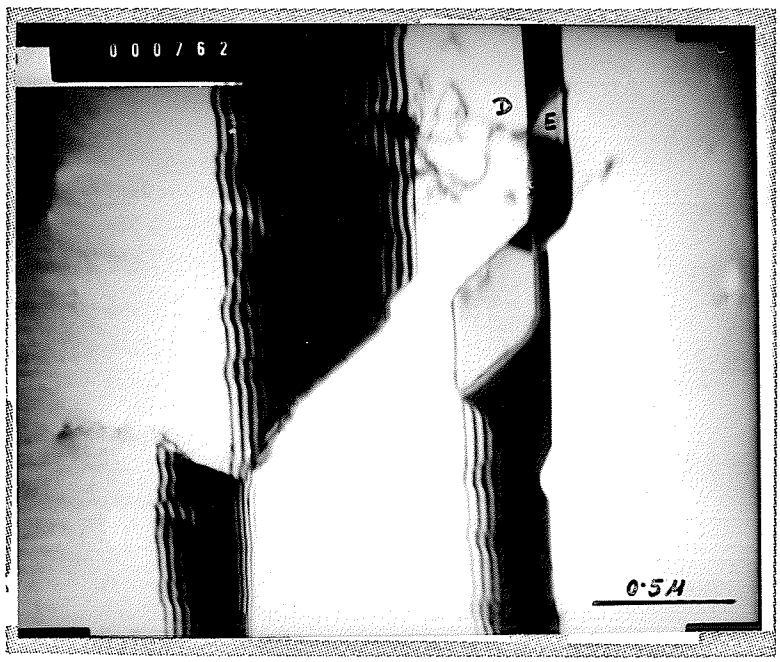

FIG.9d ELECTRON MICROGRAPH OF RECRY-STALLIZED NICKEL

Long straight dislocations (Fig. 10a) produced probably during handling of the thin foil were observed in some areas. The fact that such dislocation arrangements were not seen in any of the as annealed thin foils suggests immobility of these dislocations due to a pinning action. From the above results, it may be concluded that strains as low as 1.0×10^{-4} are sufficient to "unlock" these dislocations and render them mobile.

Stacking faults were seen in deformed nickel. From the fringe contrast (Fig. 10c) observed, it is evident that they are overlapping stacking faults rather than micro-twins, because of the constancy of the bright field fringe contrast, which is unexpected of the micro-twins[29]. These could also be considered as deformation twins which are essentially overlapping stacking faults separated by a small twinned area. The origin of the fault at the grain boundary and the dislocation free area surrounding it, suggests that stresses at the grain boundary are responsible for the splitting and movement of the grain boundary dislocations on to the parallel {111} planes and hence for the formation of stacking faults. Further discussion on stacking faults originating at grain boundaries is given in section 4.3.

Figures 10d and 10e show dislocation pile-ups in a band. The pile-ups are along the band length 'A' (of screw dislocations which cross-slip easily) and perpendicilar to the band length 'B' (edge dislocations where cross-slip is difficult). There are dislocations (probably screw) near this band, which have cross-slipped from the slip planes, constituting the band. Whereas some

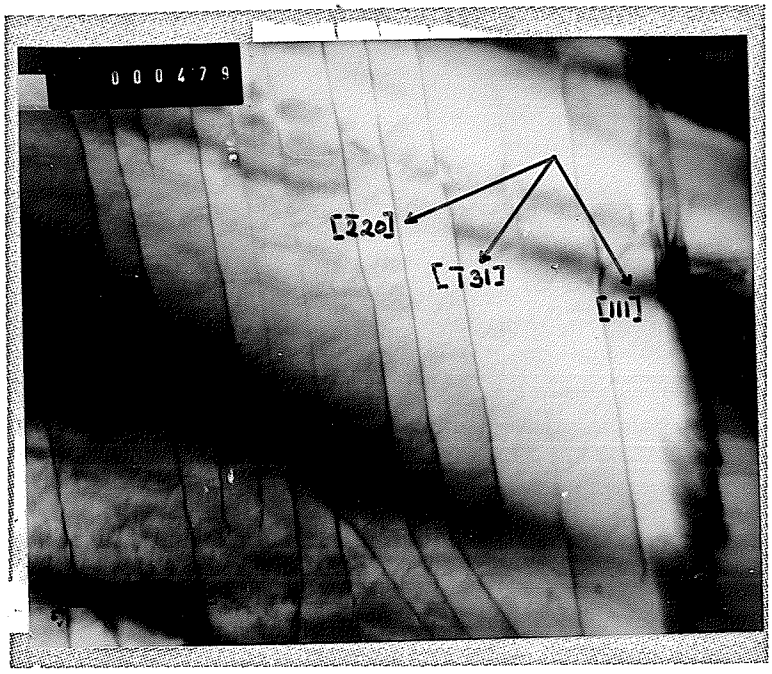

FIG.10a STRAIN = 1.0×10^{-4}

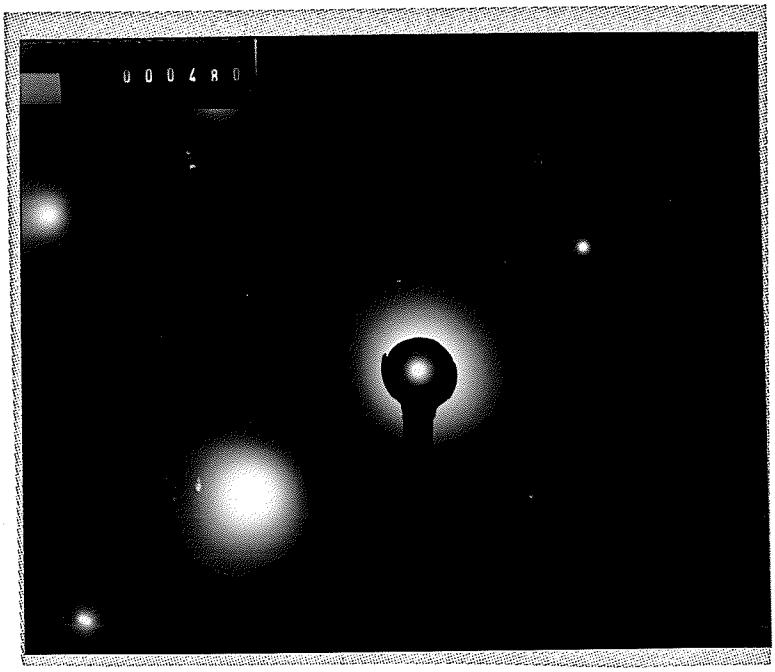

FIG.10b STRAIN = 1.0×10^{-4}

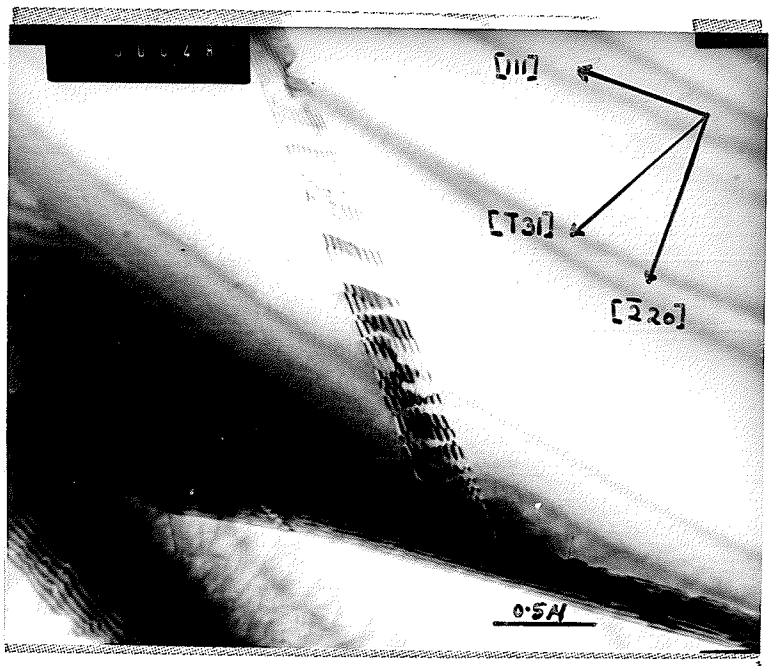

FIG. 10c STRAIN = 1.0×10^{-4}

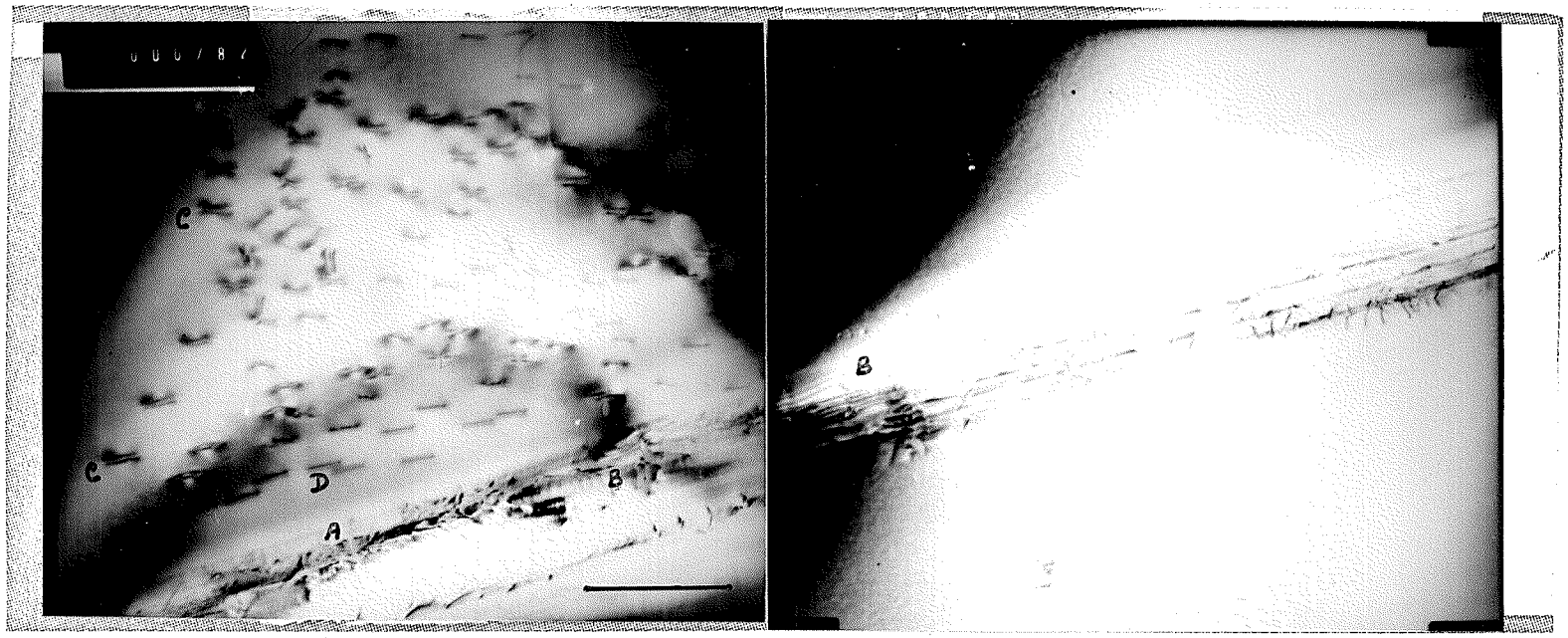

FIG.10d

STRAIN = 1.0×10^{-4}

FIG.10e

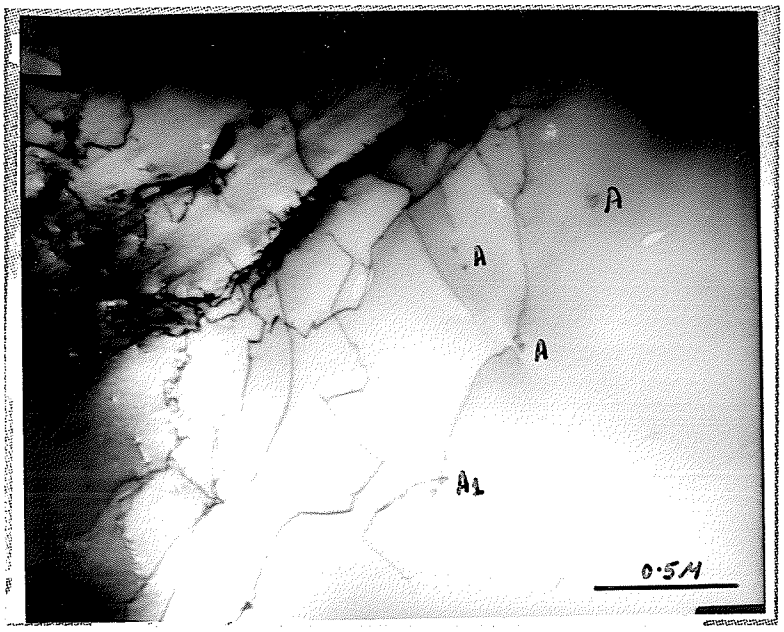

FIG.10f STRAIN=1.0×10^{-4}

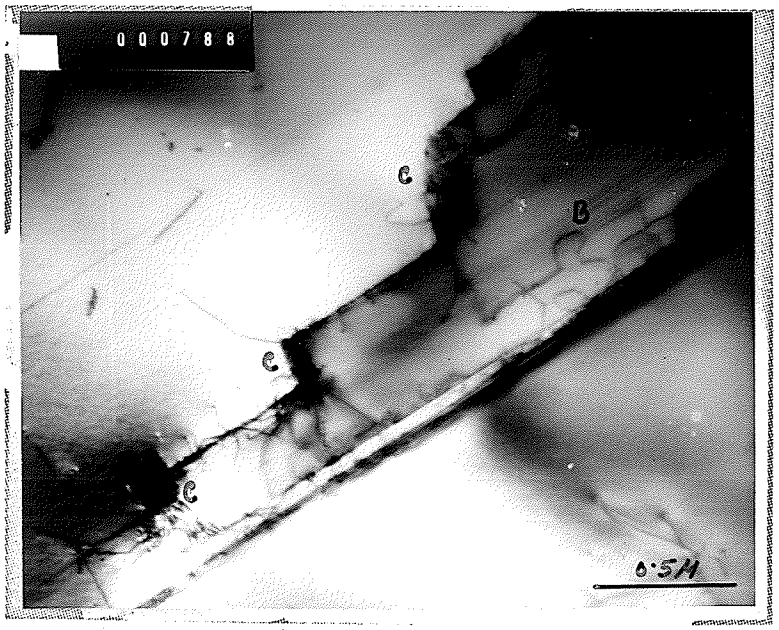

FIG.10g STRAIN=1.0×10^{-4}

of these dislocations show contrast similar to that observed for dipoles (for example at 'c'), the double image of others (for example at 'D') is suspected to be due to a double diffraction condition. From the above it is seen that deformation generally progresses on a few easy glide planes rather than throughout the material.

Figure 10f shows dislocations which have already started to interact on the glide planes. The high dislocation density along a particular direction suggests that this direction would be the interaction of planes of easy glide within the foil. The dislocations are joggy. A few dislocation loops such as at'A' are also seen which seem to be formed by the dipole mechanism seen with particular clarity at A1.

An area adjacent and to the right of the area shown in Fig 10f is shown in Fig 10g. The dislocation activity on the twin boundary is apparent. The dislocation configurations at 'A' and 'B' represent an earlier and later stage respectively of the formation of a dipole. The increased dislocation activity near the steps 'B' of the twin boundary suggests that, these twin boundary steps act as sources of dislocations.

3.2.1.1.2.2 $\varepsilon = 2.0 \times 10^{-4}$

Even at a strain of 2.0×10^{-4}, there are areas almost as free of dislocations as in recrystallized nickel (Figs. 11a and 11b). The annealing twins are seen to originate at the grain boundaries (Fig. 11b).

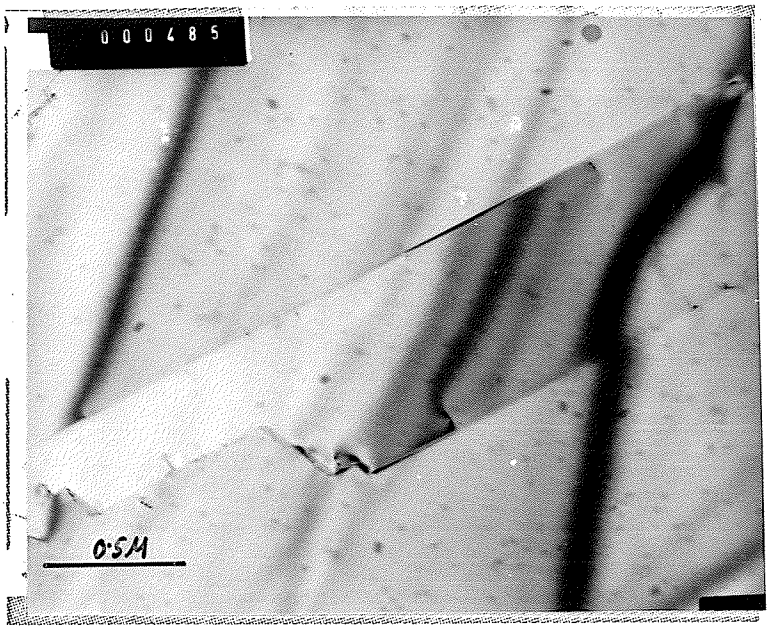

FIG.11a STRAIN = 2.0×10^{-4}

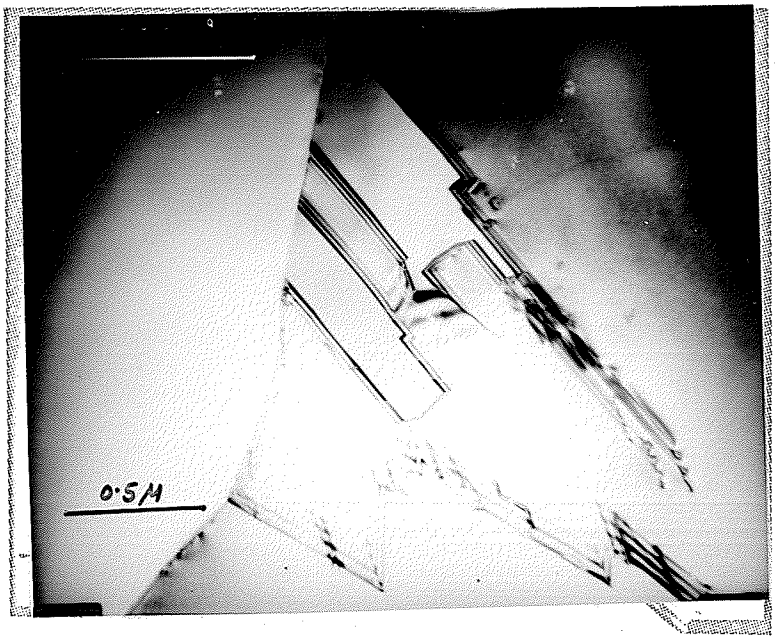

FIG.11b STRAIN = 2.0×10^{-4}

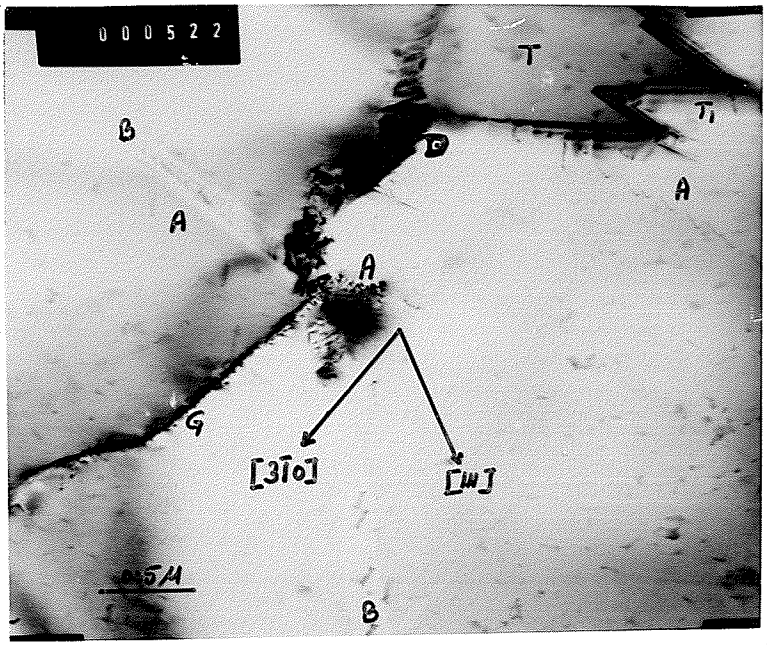

FIG.11c STRAIN = 2.0×10^{-4}

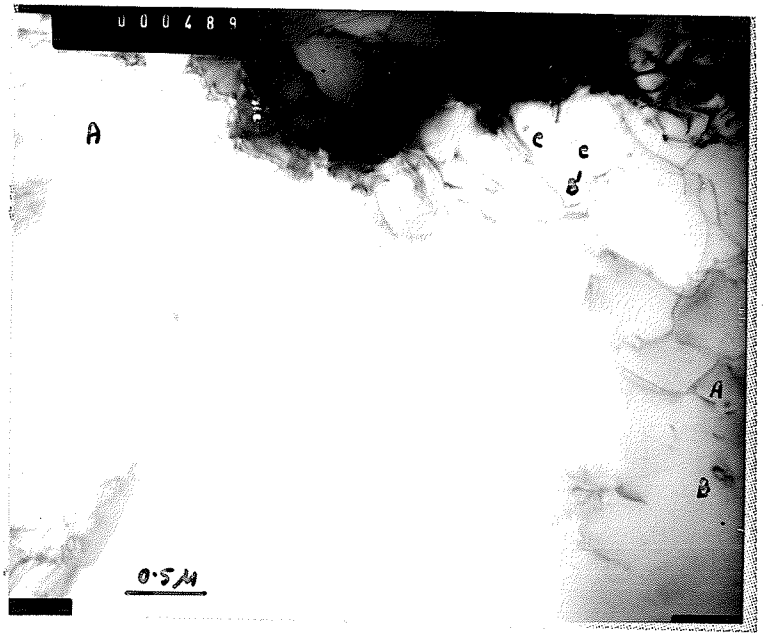

FIG.11d STRAIN = 2.0×10^{-4}

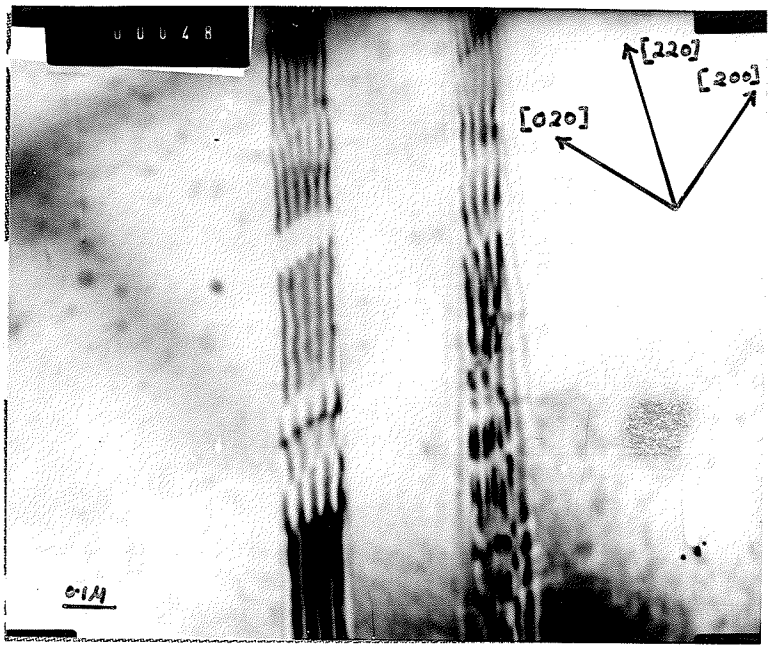

FIG.11e STRAIN=2.0X10^{-4}

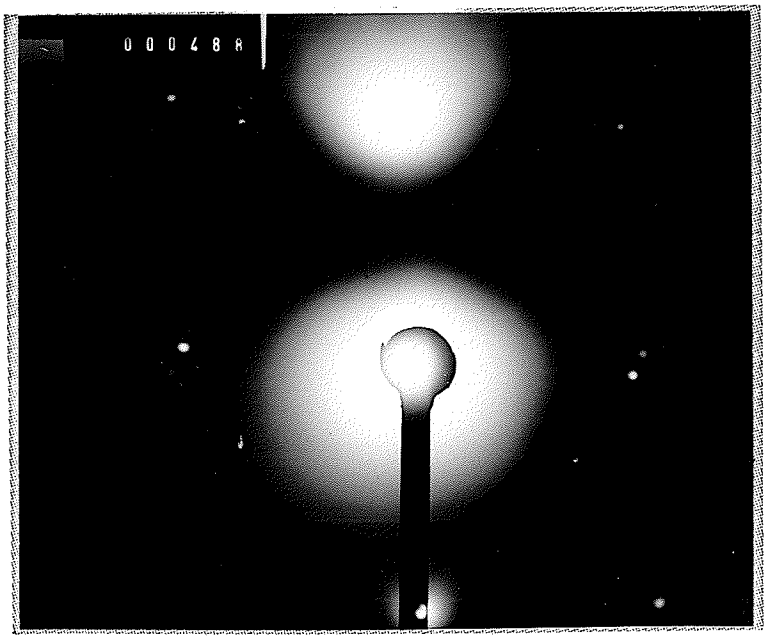

FIG.11f STRAIN=2.0X10^{-4}

The termination of the slip traces 'B' at the grain boundary in Fig. 11c and the pile-ups of dislocation on them suggest that grain boundaries are acting as sources of dislocations. The curvature of these dislocations on the slip traces, suggests that these are moving away from the grain boundary source. The twin boundary T_1 in Fig. 11c also appears to be acting as a source of dislocations, throwing out an array at 'A'. Since dislocations thus generated, lie only on the slip-planes, a proper orientation of the grain boundary or the twin boundary with respect to the slip plane is a necessary condition for them to act as sources.

The appearance (Fig. 11d) of heavily jogged dislocations 'A', the dipole configuration 'B' and the half moon contract 'c' are inter relatable. The vacancy clusters, giving rise to half moon contrast, are produced by the movement of dislocations with jogs on them. The dislocation loops 'B' are produced, most likely, by the formation of attractive junctions of dipole configuration, as is evident from the dipole configuration at 'B'. It may be mentioned that the area under examination is very localized and does not represent dislocation activity throughout the material.

A pair of single stacking faults were seen, Fig. 11e, in nickel deformed to a strain of 2.0×10^{-4}. The fringe profiles along the length of fault correspond to the condition when the foil thickness (t) is fixed and deviation(W) from the Bragg"s condition varies.[30] The dark lines represent minima in the intensity profiles and the dark extinction regions in the surrounding crystal are indicated by shading (Fig. 12). The fringes branch at certain

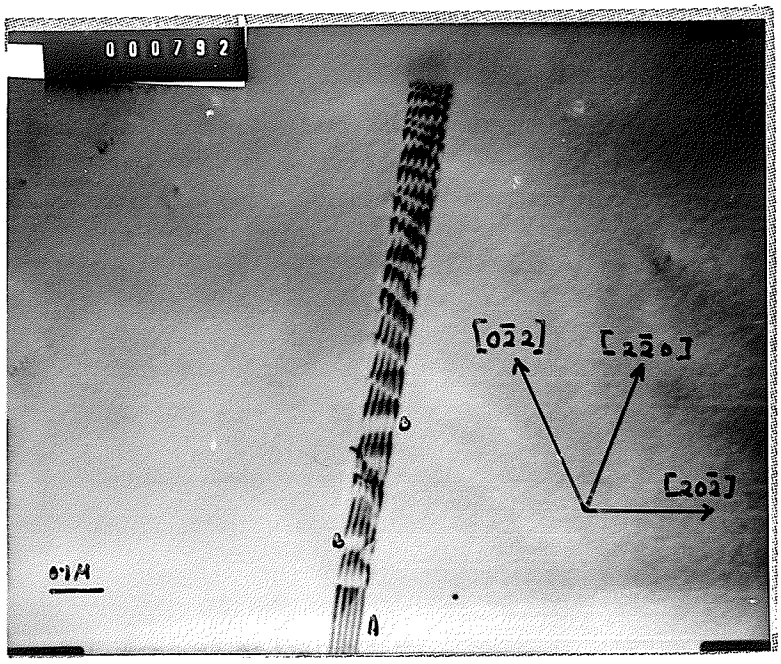

FIG.11g STRAIN=2.0×10^{-4}

FIG.11h STRAIN=2.0×10^{-4}

FIG.11i STRAIN = 2.0×10^{-4}

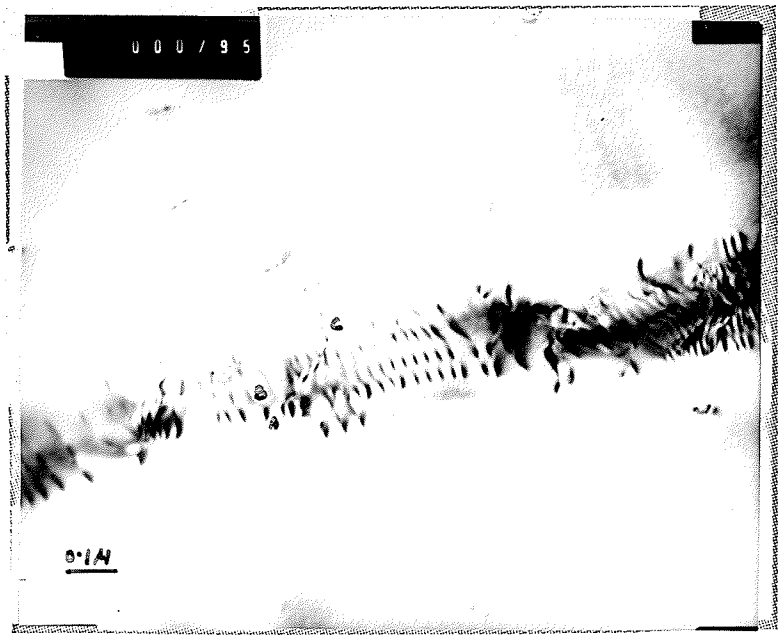

FIG.11j STRAIN = 2.0×10^{-4}

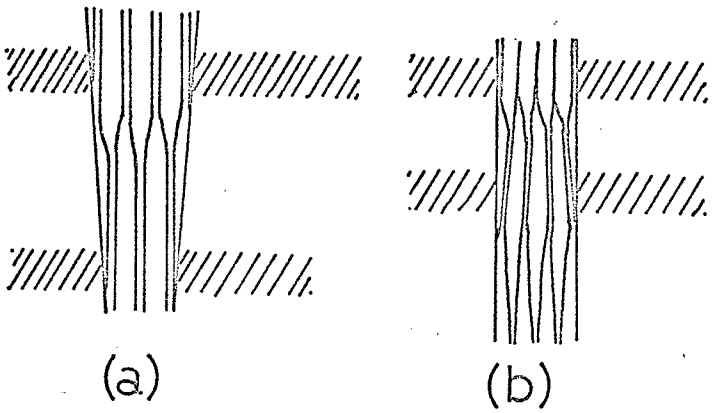

FIG.12 EFFECT OF VARYING THICKNESS WITH FIXED DEVIATION (w) FROM THE BRAGG CONDITION (FIG.12a) AND VARYING (w) WITH FIXED THICKNESS (FIG.12b) ON STACKING FAULT IMAGE PROFILES.

points along the length of the fault in the sense that the strong fringes become weak fringes and vise-versa. The above contrast conditions are fully met by the fault in Fig. 11e. The foil orientation is (100) and since the faults are lying along [220], (111) is the faulting plane, as expected.

Overlapping stacking faults were also seen in the specimens deformed up to 2.0×10^{-4} strain. Their Bright field, Dark field and Selected area diffraction pattern (S.A.D.P.) are shown in Fig. 11g to 11i respectively. Since, most of the contrast from the faulted length is (except at 'A') due to overlapping faults, the method[31] to determine their nature can be applied only to section 'A'. Thus analysed, the fault was found to be intrinsic in nature (Details in Appendix I). The faulting was found to be on the $(11\bar{1})$ plane as the fault lies along $[1\bar{1}0]$ direction and the foil plane is (111). In the region where the faults are overlapping the contrast vanishes whenever three faults overlap as seen at 'B' in Fig. 11g.

A careful examination of Fig. 11j reveals nodal configuration of split partials. The extended node at 'A' and constricted node at 'B' can be clearly seen. An enlarged photograph of this area will be analysed to determine the stacking fault energy of pure nickel.

3.2.1.1.2.3 $\varepsilon = 3.0 \times 10^{-4}$

The electron mecrographs of specimens deformed to a strain of 3.0×10^{-4} are shown in Figs. 13(a-d). Apart from the

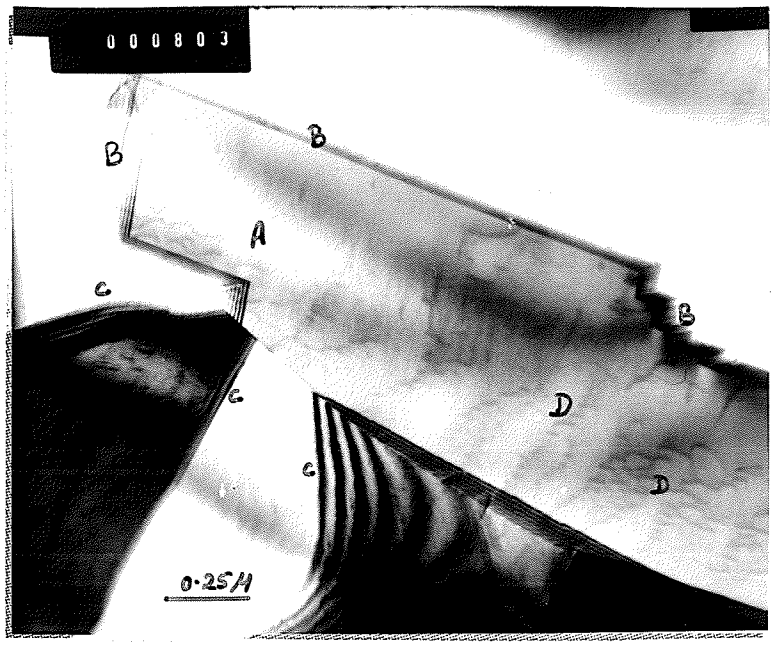

FIG.13a STRAIN = 3.0×10^{-4}

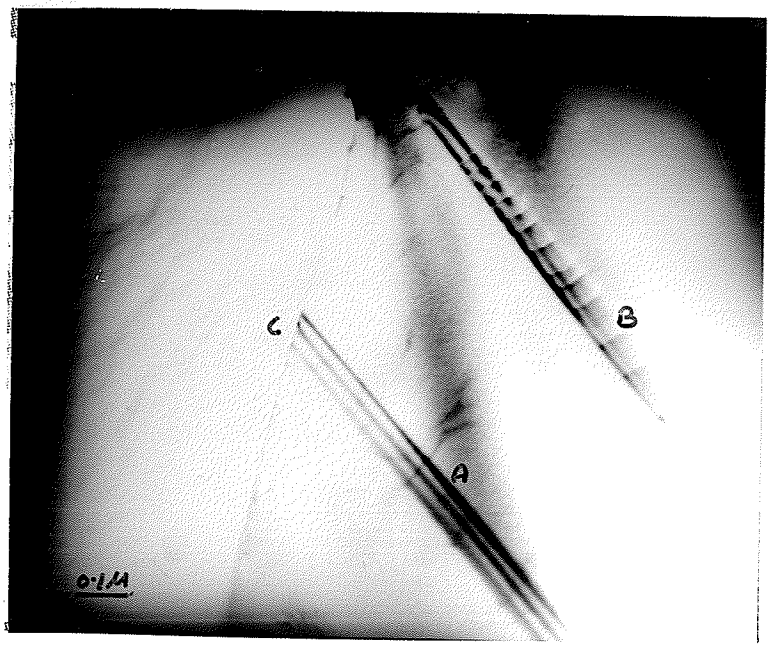

FIG.13b STRAIN = 3.0×10^{-4}

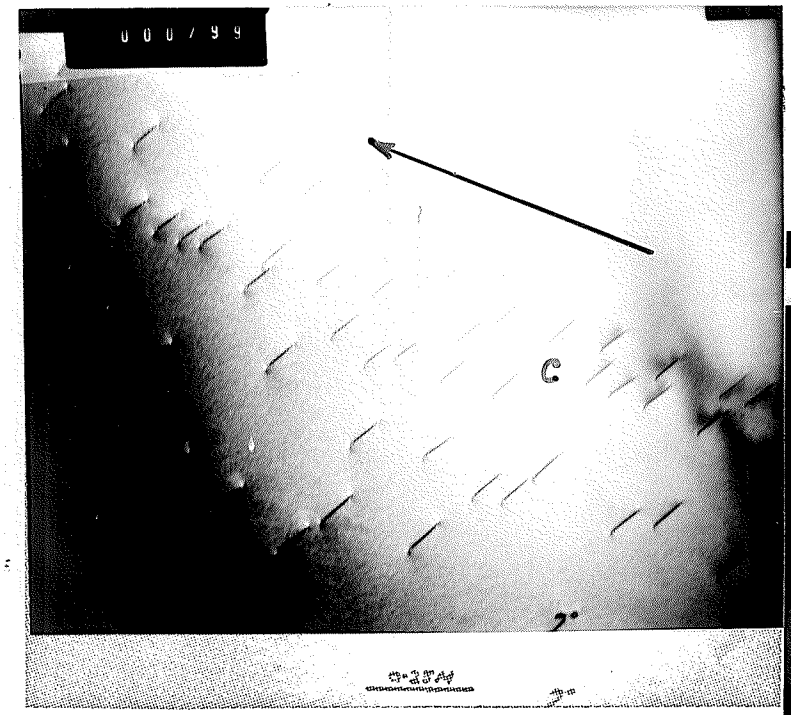

FIG. 13d

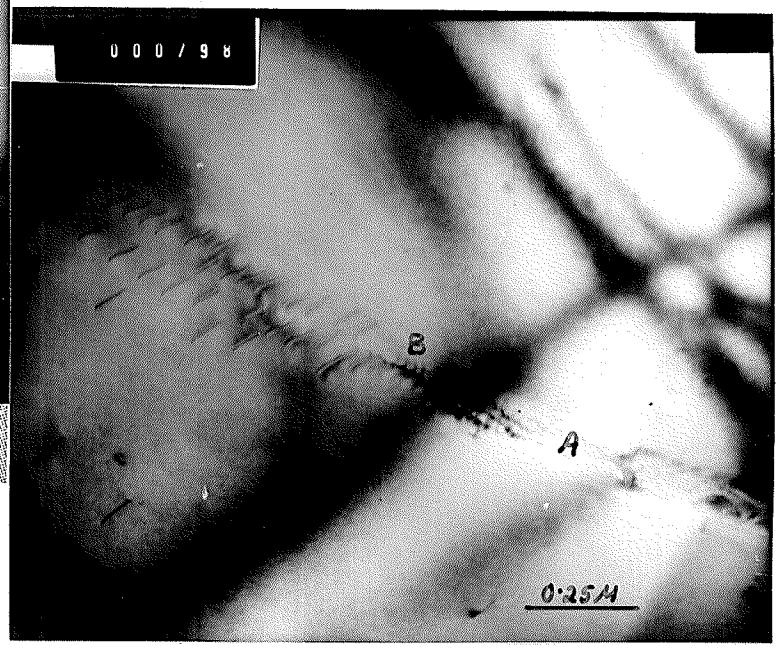

STRAIN = 3.0×10^{-4}

FIG. 13c

twin 'A', twin boundaries 'B' and grain boundaries 'c', some helical dislocations on twin 'A' at 'D' are seen in Fig. 13a. Twin boundary dislocations 'B' and single stacking fault 'A; originating at the grain boundary at 'c' can be clearly seen in Fig. 13b.

Dislocation pile-ups on slip plane 'A' are shown in Figs. 13c and 13d. Fig. 13d is an area left to that of Fig. 13c. Given the proper orientation condition (as at 'B') these piled-up dislocations cross-slip to other planes. An uniform distribution 'c', of these dislocations after cross-slipping, suggests their screw character. The similar nature of end contrast from these dislocations suggests a similarity in their character[32]. The curvature of the dislocations (c) suggest that their direction of movement is as indicated by the arrow in Fig. 13d.

3.2.1.1.2.4 $\varepsilon = 4.0 \times 10^{-4}$

Fig. 14a shows annealing twins 'T' and the twin boundaries 'T_B'. This electron micrograph also shows the manner in which dislocations move within the twin boundary. The twin boundary dislocations as at 'A' move along the direction of the arrow. Beyond 'A' the sudden change in the twin boundary direciton leads to the corss-slipping of dislocations on to the twin boundary along A'A". The initial stages of this corss-slip process is seen at A_1A' and A". The dislocations after cross-slipping are seen at B and C. Similar contrast from these dislocations suggests that these have the same character. These dislocations are seen to interact on the twin boundary for example at 'D'. These dislocations, as they move, and when provided with proper crystallographic orientation

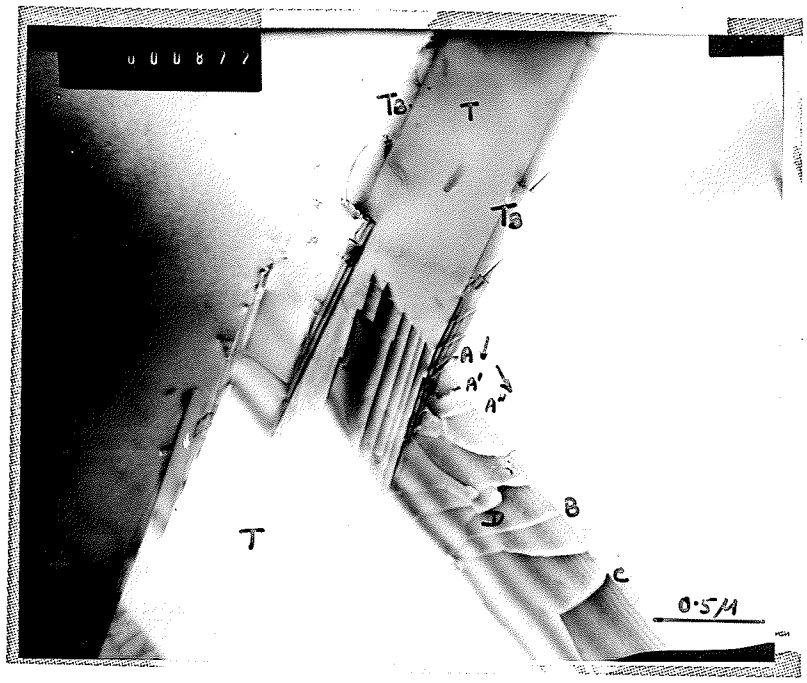

FIG.14a STRAIN = 4.0×10^{-4}

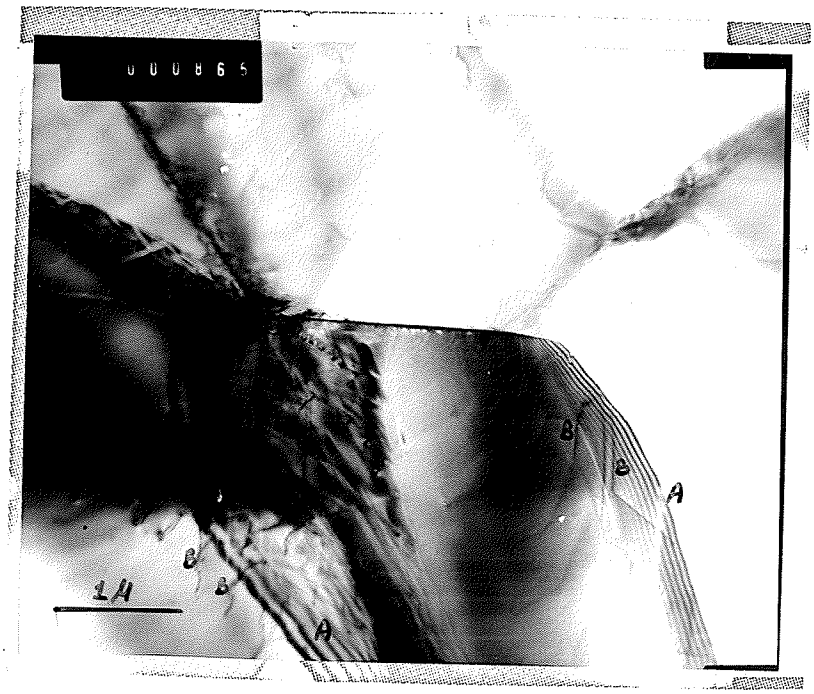

FIG. 14b STRAIN = 4.0×10^{-4}

conditions, can cross-slip from the twin boundaries on to the slip planes and may thus act as sources of dislocations. Fig. 14b shows dislocations 'B' eminating from the grain boundaries 'A'.

The general nature of the dislocation arrangements at 4.0×10^{-4} strain is represented by the electron micrographs in Figs. 14(c-h). There is an appreciable increase in the dislocation density at 4.0×10^{-4} strain as compared to that in specimens deformed upto 3.0×10^{-4} strain. The cell formation is quite evident from Figs. 14e and 14f. There is a significant increase in the dislocation loop density (Fig. 14d). A magnified picture (Fig. 14g) of the area'A' of Fig. 14f shows heavily tangled dislocations at 'A' and dislocation loops at 'B'. A careful examination of Fig. 14h suggests that the following mechanisms are responsible for the defect generation.

1. Movement of heavily jogged dislocations leads to dipole formation at at 'B' and dislocation loops are created by the pinching of dipoles as at 'A' and 'c'.
2. The dislocation loops can also be formed by the attraction of opposite type of dislocations moving on parallel planes as at 'D'.

Dislocation cell formation is clearly seen in specimens deformed to 4.0×10^{-4} strain in Fig. 14i and 14j. The dislocations within the cell of Fig. 14j are mostly straight with a few jogs on them, but the dislocations in the cell walls are badly tangled. The straightness of dislocations within the cell and their cross-grid arrangement suggest that these are produced

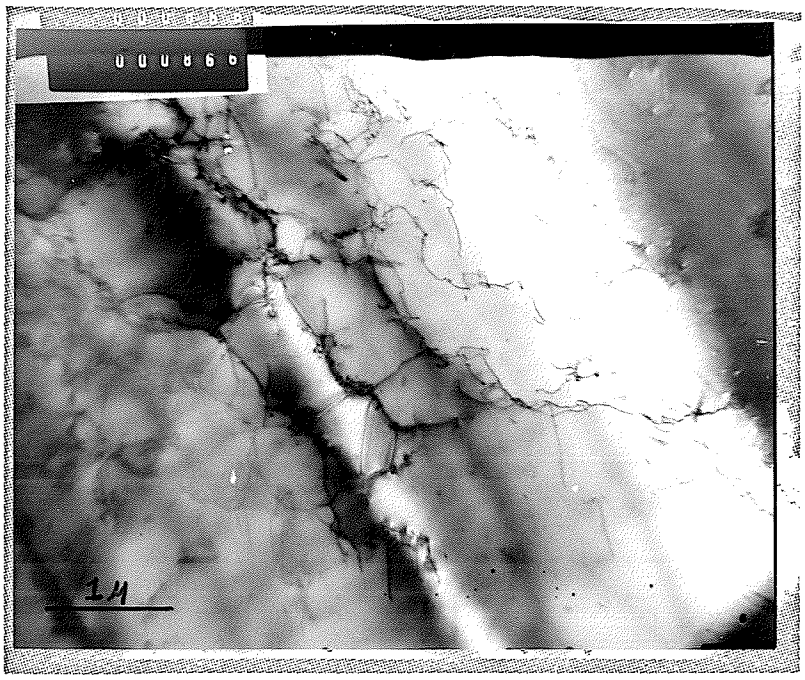

FIG. 14c STRAIN = 4.0×10^{-4}

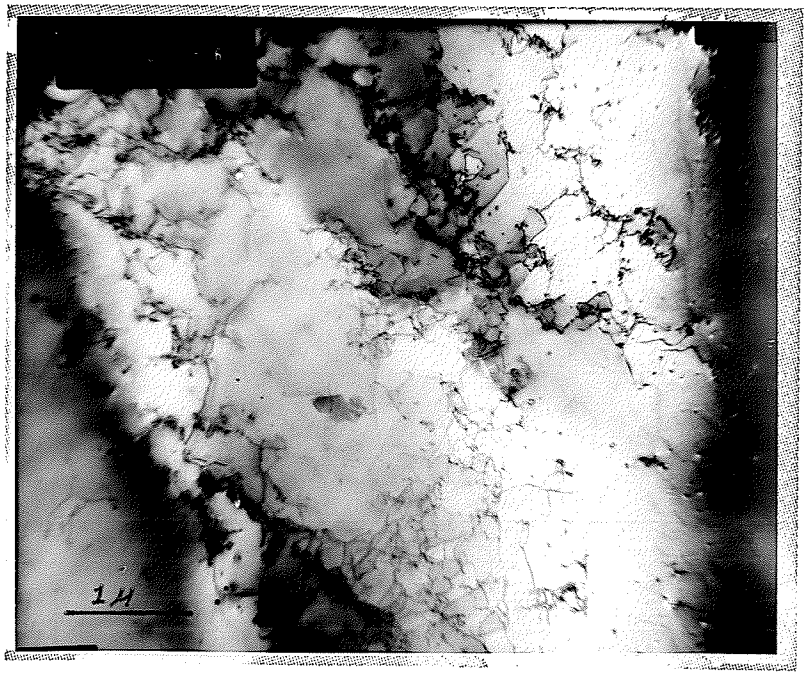

FIG. 14d STRAIN = 4.0×10^{-4}

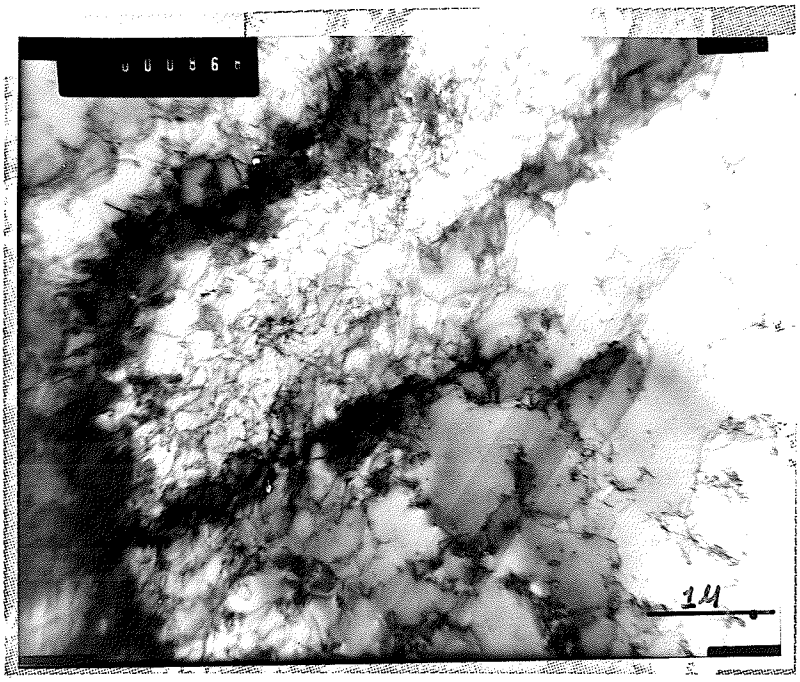

FIG.14e STRAIN = 4.0×10^{-4}

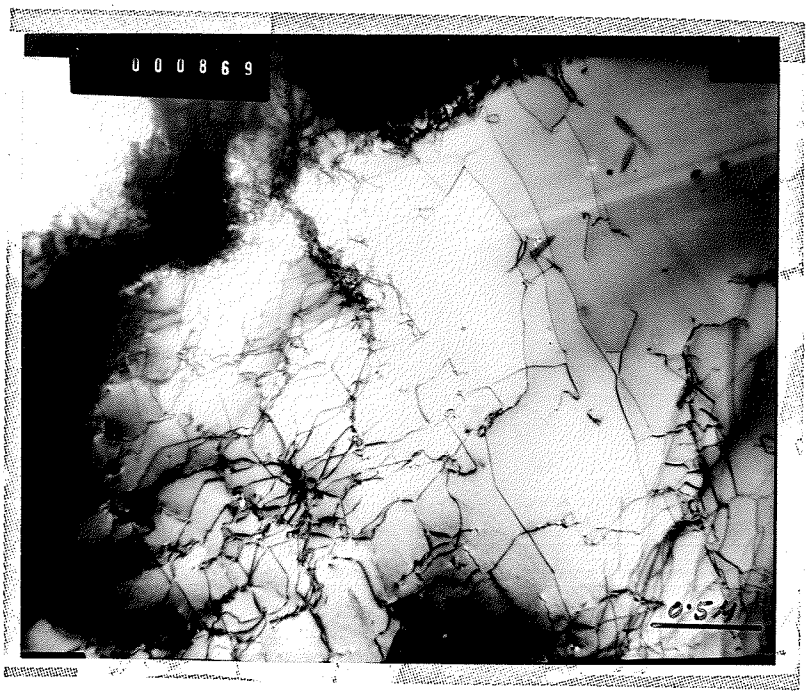

FIG.14f STRAIN = 4.0×10^{-4}

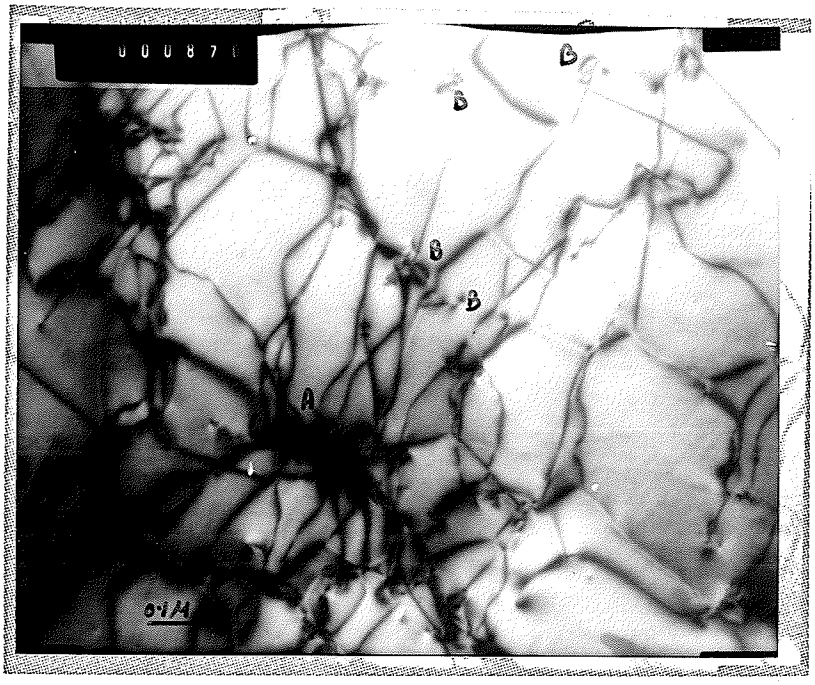

FIG.14g STRAIN = 4.0×10^{-4}

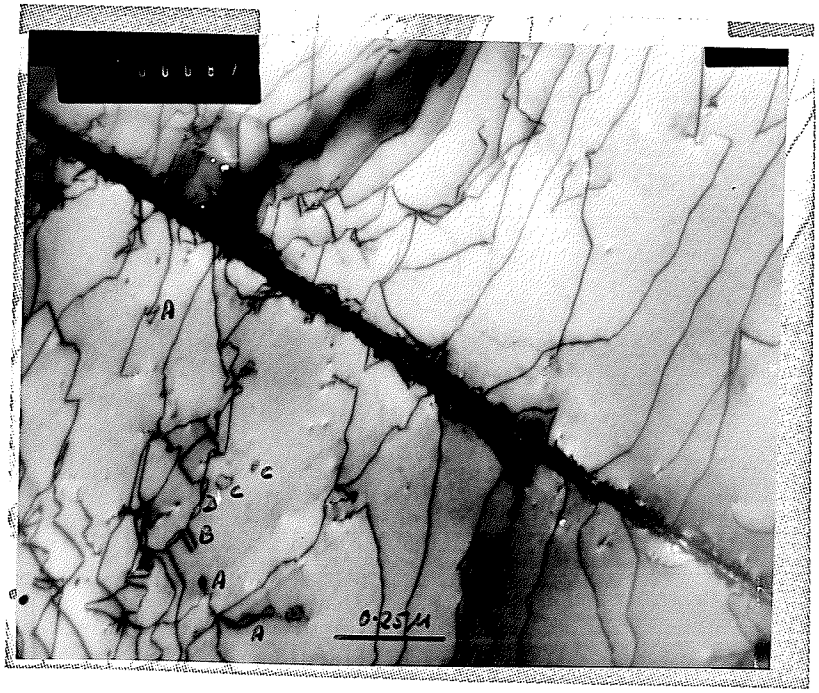

FIG.14h STRAIN = 4.0×10^{-4}

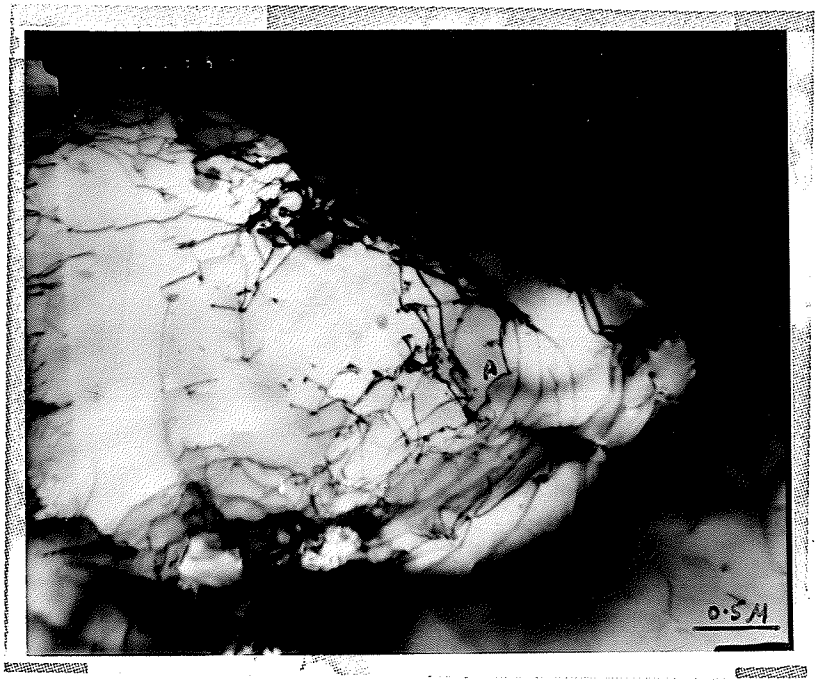

FIG.14i STRAIN = 4.0×10^{-4}

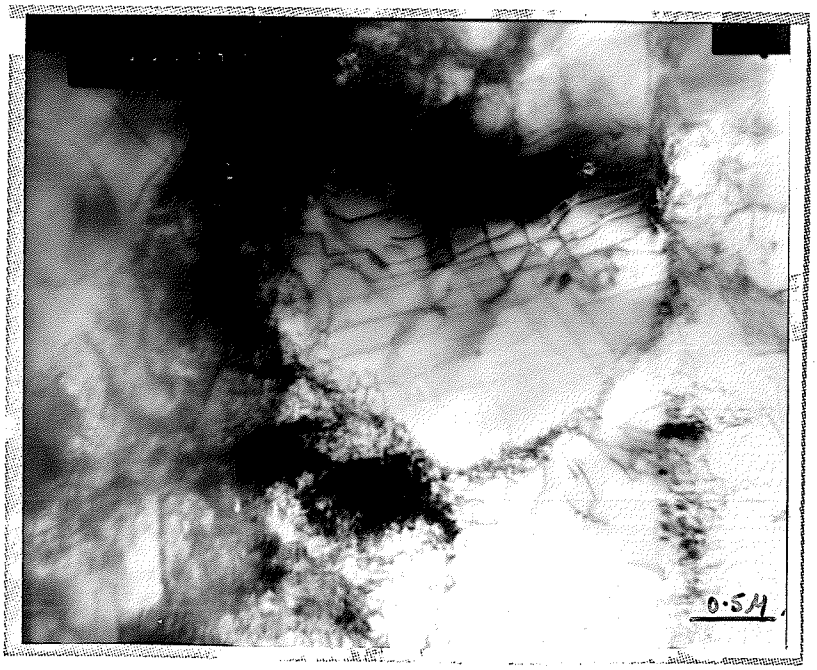

FIG.14j STRAIN = 4.0×10^{-4}

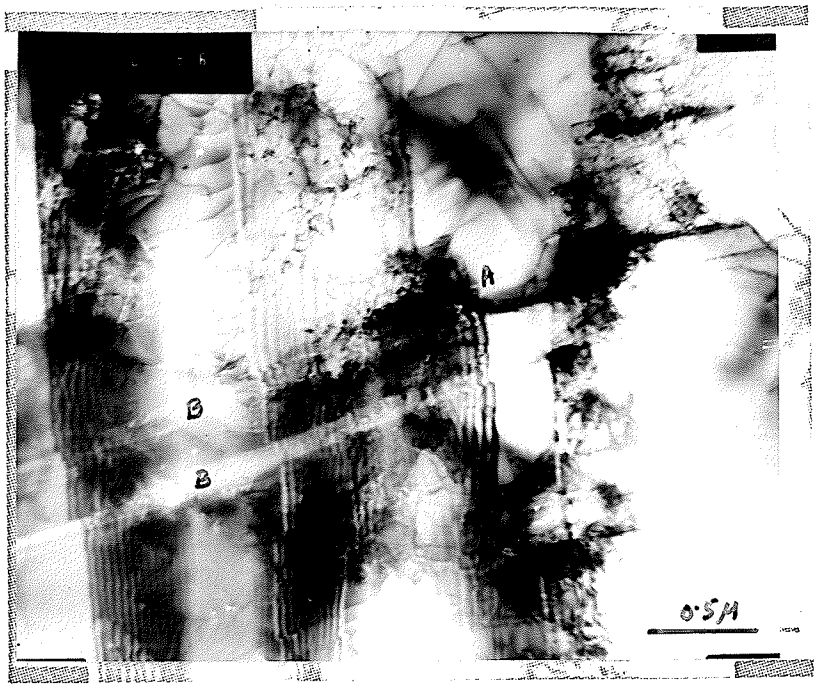

FIG.14k STRAIN = 4.0×10^{-4}

FIG.14l STRAIN = 4.0×10^{-4}

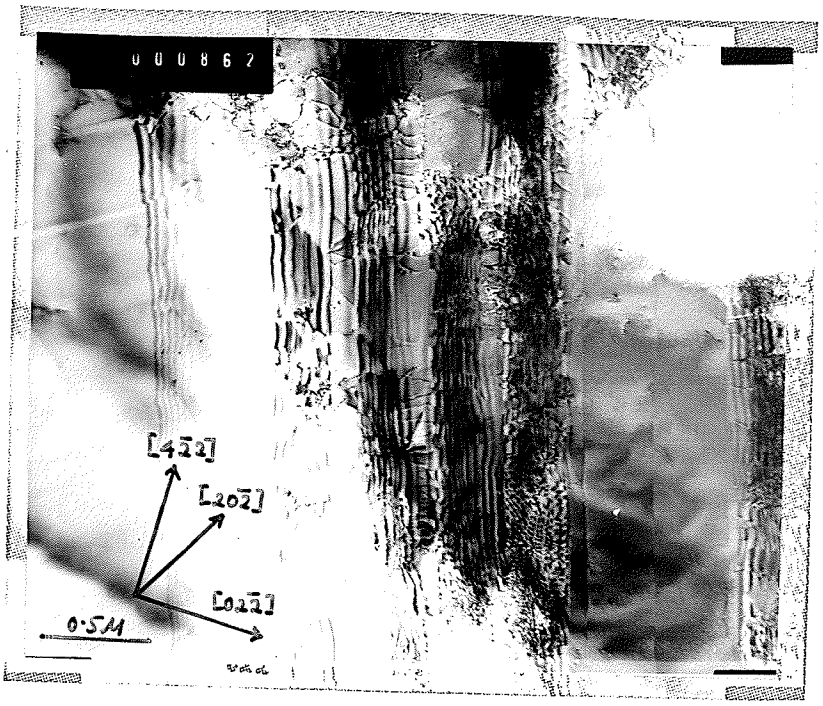

FIG.14m STRAIN = 4.0×10^{-4}

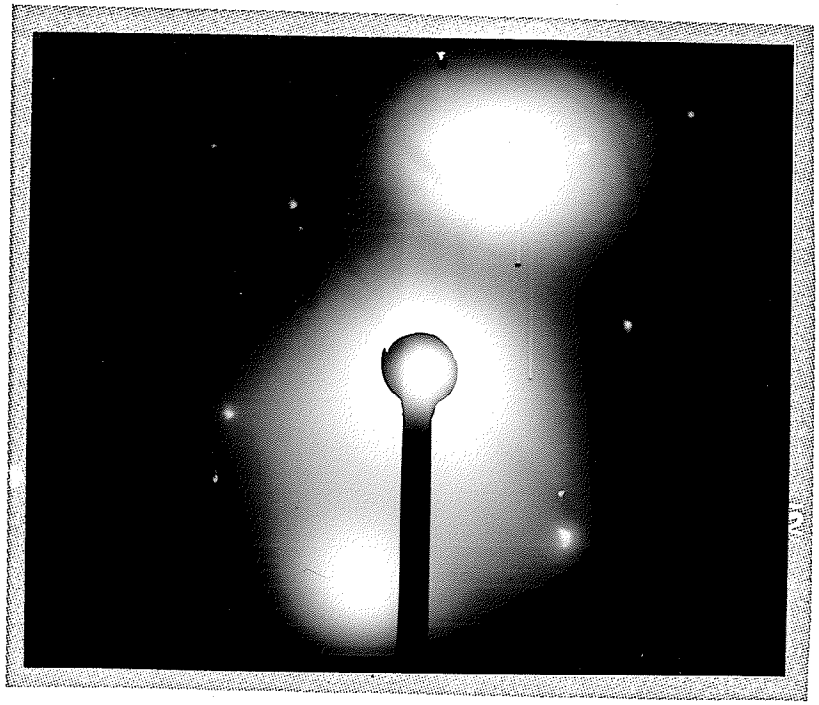

FIG.14n STRAIN = 4.0×10^{-4}

FIG.14o STRAIN = 4.0×10^{-4}

by the hydrostatic nature of stresses from the cell walls.

Stacking fault bundles were observed in nickel deformed to 4.0×10^{-4} strain. A series of photographs along their length were taken and these are shown in Fig. 14(k-o). These faults were analysed (Appendix I) and were found to be intrinsic in nature. These faults are mostly single except the fault 'E' in Fig. 14m which gives contrast similar to that of the overlapping faults. These faults were found to originate at the intersection of the slip planes as is shown by the fault originating at 'A' in Fig. 14k which is the intersection of slip plane 'B' with the fault plane. This fact is also supported by the generation of overlapping faults 'E' in Fig. 14m at 'c' where the slip trace'B' intersects the fault plane whose slip trace is 'D'. To find the slip plane 'B' and fault plane 'D' selected area diffraction pattern was taken of Fig. 14m and is shown in Fig. 14n. The foil plane was found to be (111). Since the trace 'D' is lying along $[20\bar{2}]$, the slip plane 'D' is $(11\bar{1})$ and the slip plane 'B' is $(1\bar{1}1)$. Therefore, the faults are not generated only at the grain boundaries but also at the intersections of slip or glide planes. Fig. 14o shows the dark field electron-micrograph of the area shown in Fig. 14m and was used to determine the nature of the stacking faults.

3.2.1.1.2.5 $\varepsilon = 5.0 \times 10^{-4}$

The specimens deformed to a strain of 5.0×10^{-4}, were examined and the electron micrographs are shown in Figs. 15(a-i) Figs. 15a and 15b are from adjacent areas and show the general

FIG.15a STRAIN = 5.0×10^{-4}

FIG.15b STRAIN = 5.0×10^{-4}

nature of dislocation arrangements at this strain. An examination of dislocations in Fig. 15a suggests that these dislocations are heavily tangled along <110> directions which is the direction of intersection of {111} planes. The areas surrounded by these tangles contain cross-grids of long and heavily jogged dislocations. The dislocation loops at 'A' seen to have formed by the attraction between the two arms of the same dislocation moving on parallel planes. The stage just before the pinching is as shown at 'c' in Fig. 15a. A series of loops formed in this manner are seen at 'A' in Fig. 15a. The dislocation dipoles are also seen to form by the movement of jogged dislocations as at 'B' in Figs. 15a and 15b. The dislocation cell formation is also seen to be present at this strain of 5.0×10^{-4} and is shown at 'A' in Figs. 15c and 15d.

The stacking fault bundles were also seen in specimens deformed to 5.0×10^{-4} strain. A series of electron micrographs in Figs. 15(e-i) were taken along the length of these overlapping, intrinsic stacking faults (Appendix I). The foil plane was found to be (110) and since these faults lie along $[\bar{2}20]$, the fault plane is (111). The nature of dislocations on slip plane 'A' in Fig. 15g, being similar to the dislocations observed in the twin boundaries in Fig. 14a, suggests that these dislocations have come to the slip planes 'A' from the twin boundaries and seen to be responsible for the formation of overlapping stacking faults. Figs. 15(e-g) are Bright field electron-micrographs of the stacking faults and Figs. 15h and 15i are the S.A.D.P. and Dark field respectively of the stacking fault in Fig. 15g.

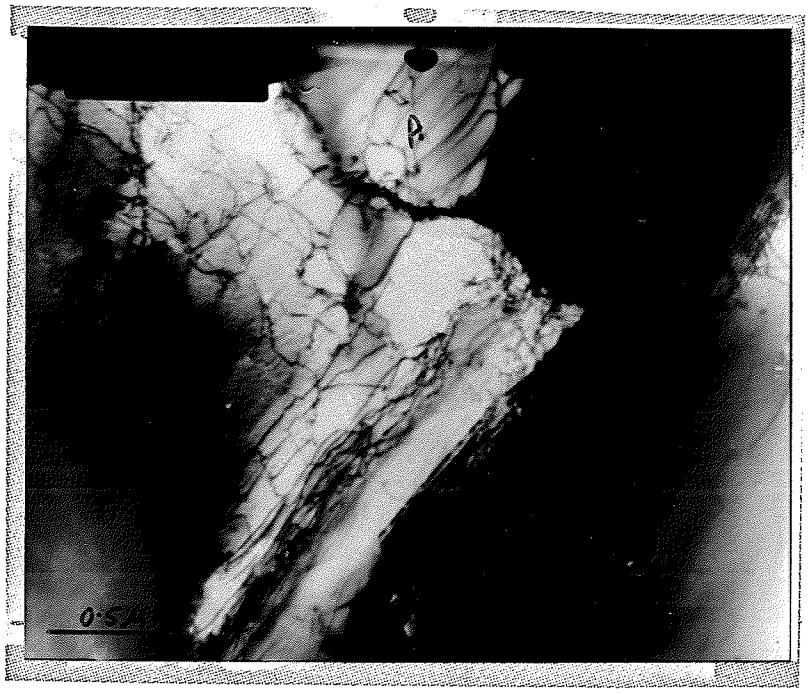

FIG.15c STRAIN = 5.0×10^{-4}

FIG.15d STRAIN = 5.0×10^{-4}

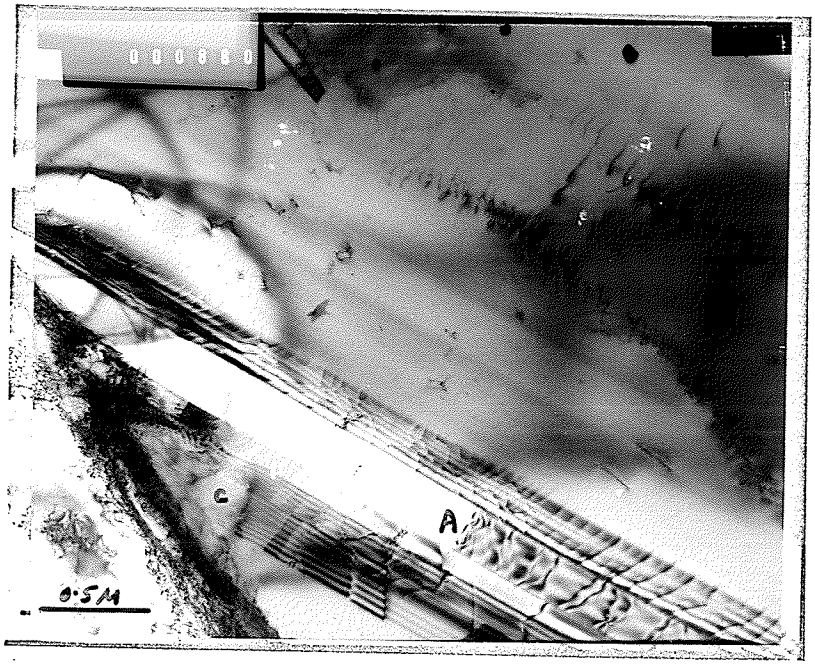

FIG.15e STRAIN = 5.0×10^{-4}

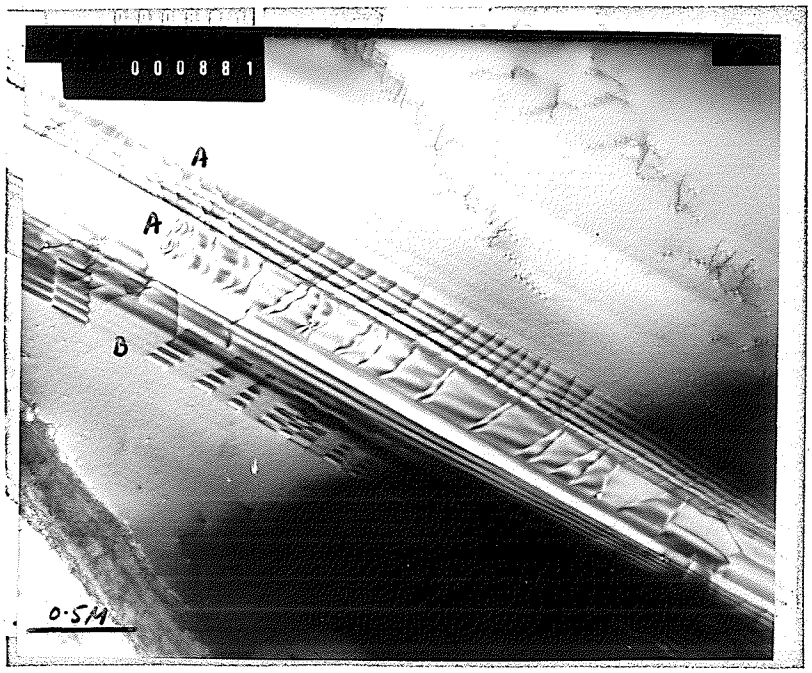

FIG.15f STRAIN = 5.0×10^{-4}

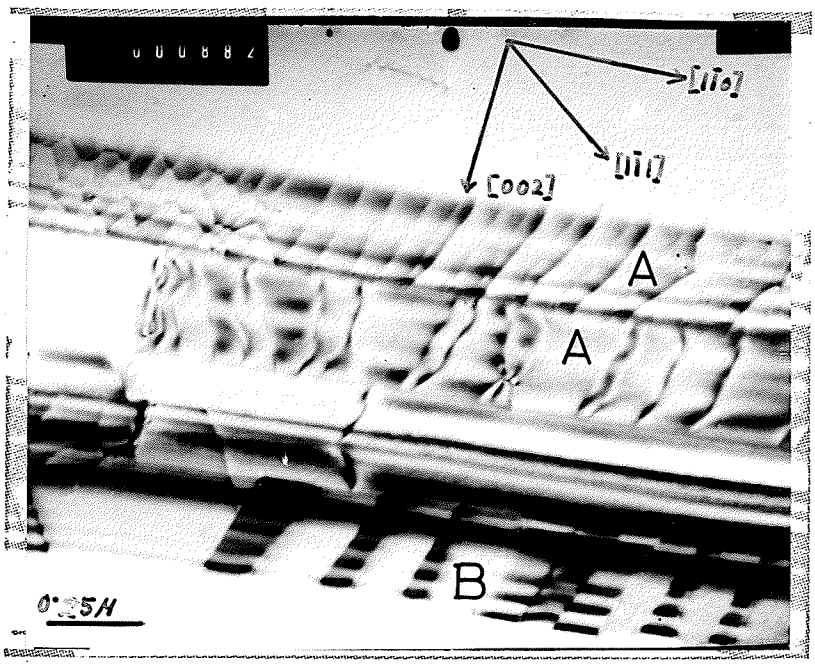

FIG.15g STRAIN=5.0×10^{-4}

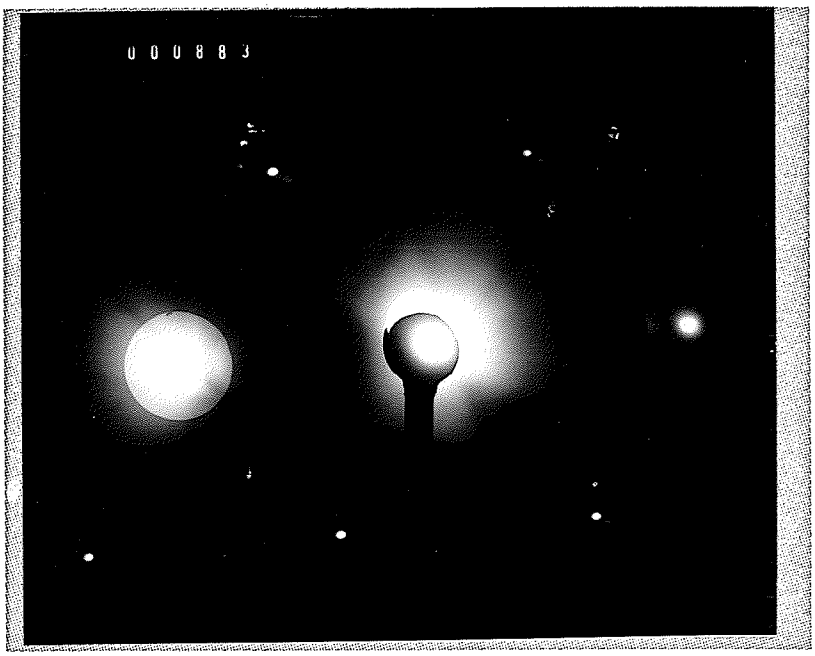

FIG.15h STRAIN=5.0×10^{-4}

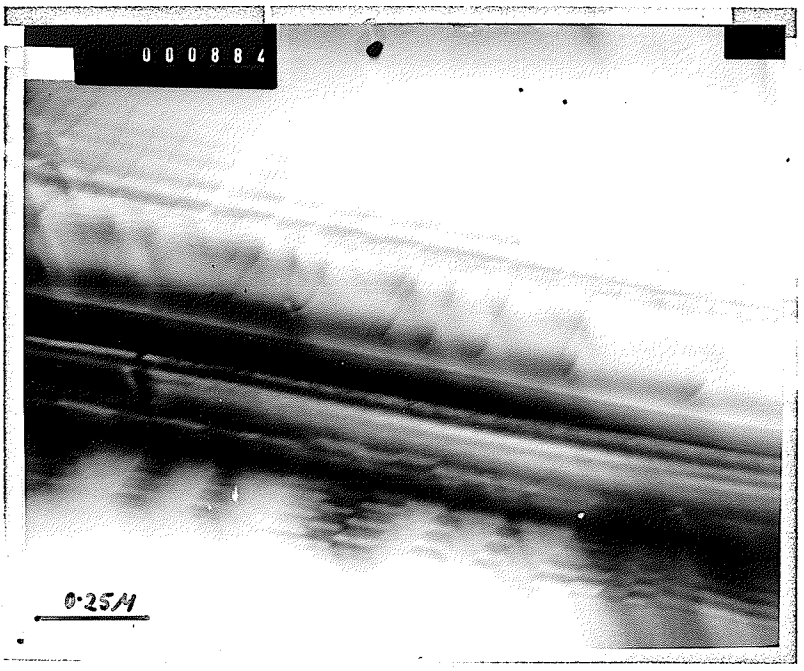

FIG.15i STRAIN=5.0×10^{-4}

3.2.1.1.2.6 $\varepsilon = 6.0 \times 10^{-4}$

The cross-slipped screw dislocations, piles up against a grain boundary beyond 'A', can be seen in Fig. 16a. These dislocations do not seem to lie on the foil plane (01 1) because the zig-zag contrast suggests that they are inclined to the foil plane. All of them are of similar character because of the similar nature of contrast from their ends 'B'. Fig. 16b shows similar dislocations but uniformly distributed suggesting that these dislocations are screw in character and can glide easily.

Long and heavily jogged dislocations 'c' were observed (Fig. 16c) in specimens deformed to 6.0×10^{-4} strain. The slip traces at 'A', dislocation loops at'D' and point defect clusters at 'B' giving rise to half moon contrast can be clearly seen. The dislocation tangles generated at this strain are shown in Fig. 16d. Comparing with previous electron micrographs (up to a strain of 3.0×10^{-4}), a considerable increase in dislocation density is apparent. There is a general increase in tangling and so most of these tangles lie along a particular direction, this direction is expected to be the intersection of planes of easy glide within the foil resulting in the formation of Cottrell locks. The free dislocations away from these locks, contain multiple jogs 'A'. The point defect clusters were seen to be left behind the dipole configuration as at 'B' and the absence of point defect clusters near the grain boundary, suggests its effectiveness as a sink.

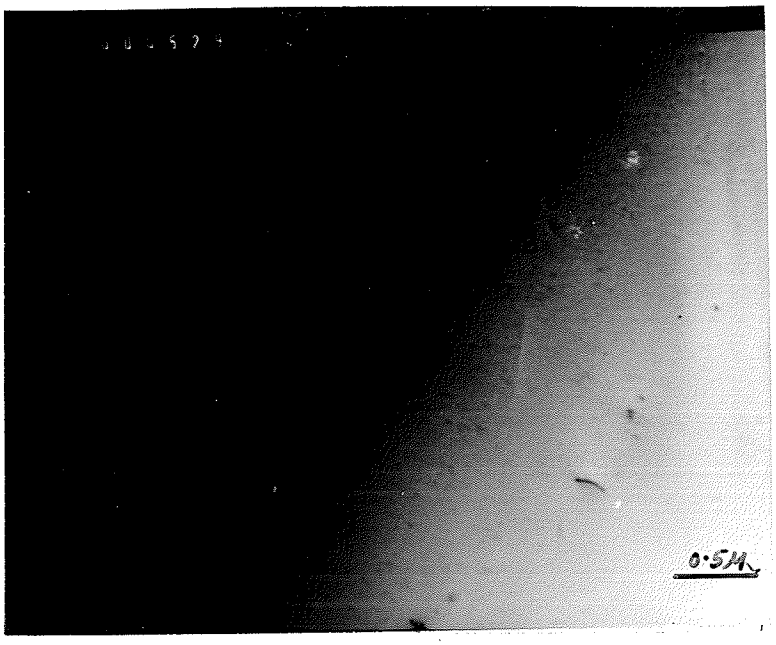

FIG.16a STRAIN=6.0×10^{-4}

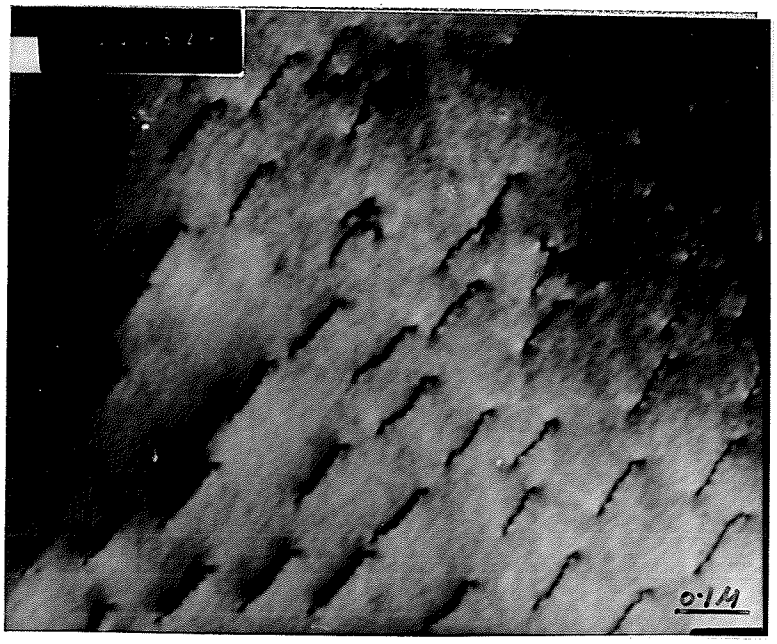

FIG.16b STRAIN=6.0×10^{-4}

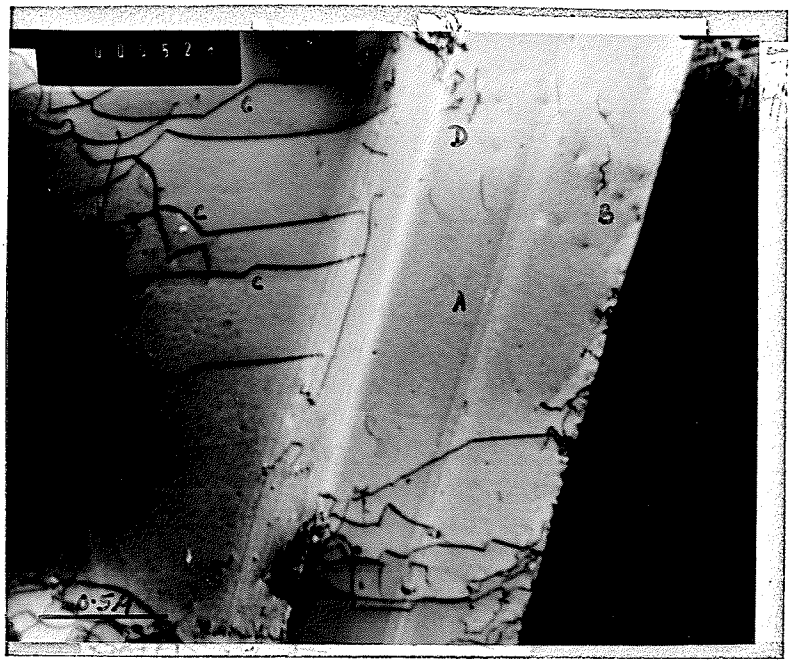

FIG.16c STRAIN= 6.0×10^{-4}

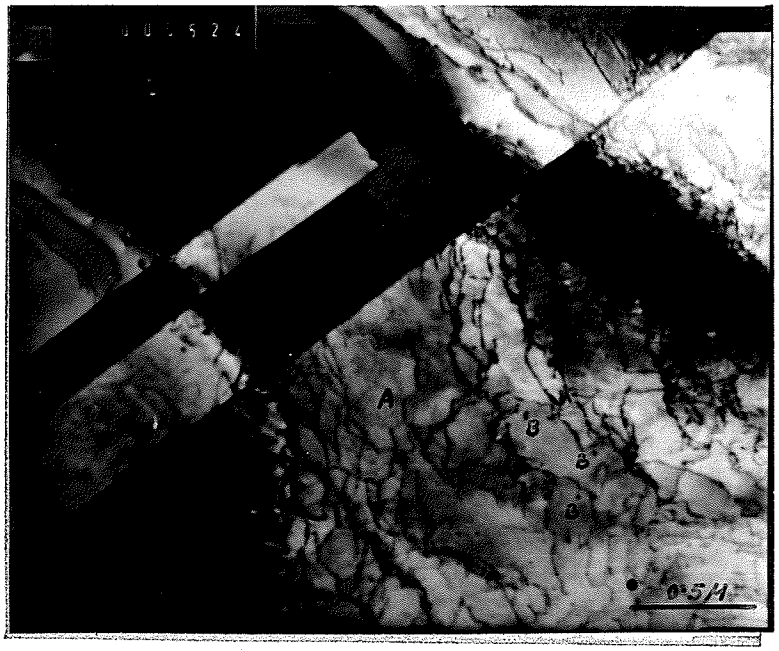

FIG.16d STRAIN= 6.0×10^{-4}

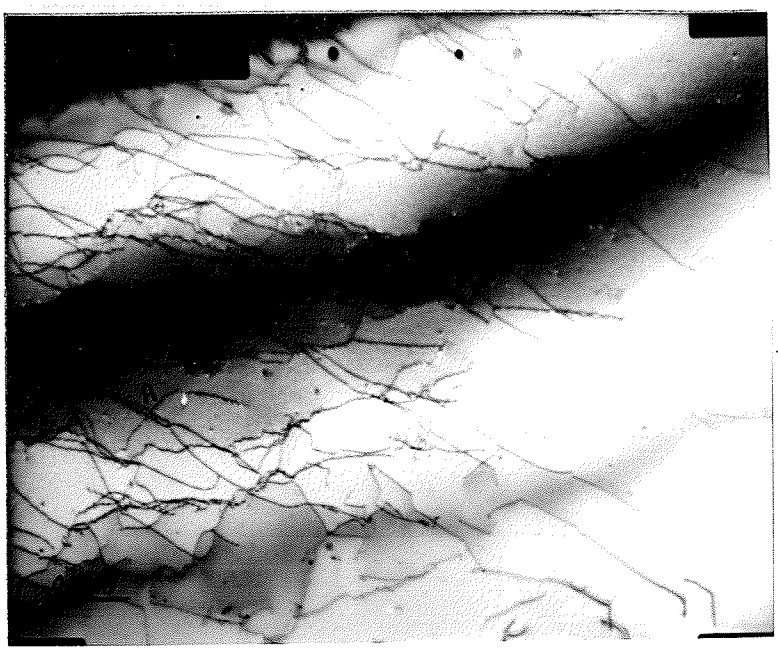

FIG.16e STRAIN = 6.0×10^{-4}

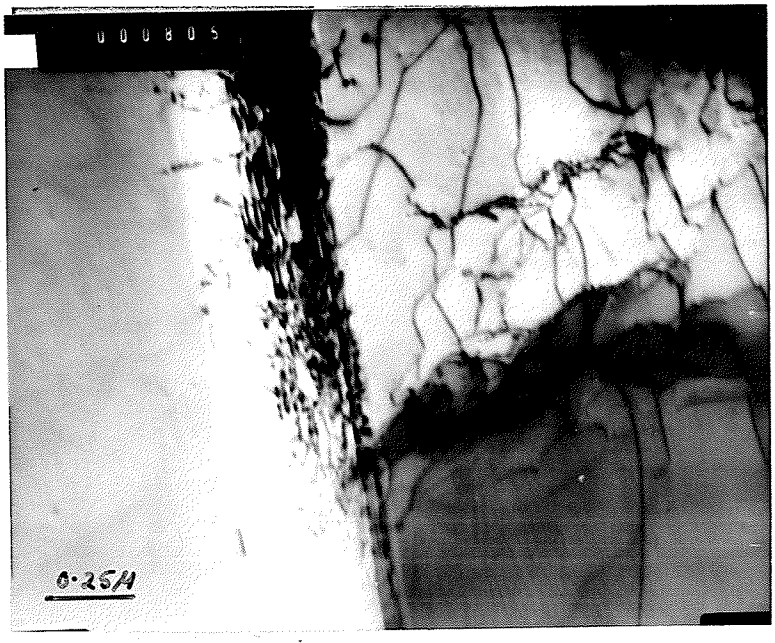

FIG.16f STRAIN = 6.0×10^{-4}

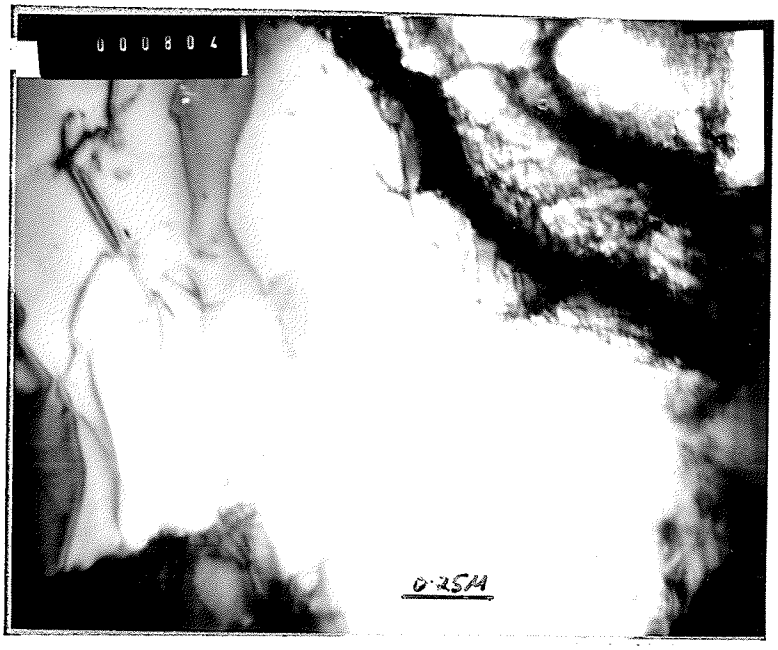

FIG.16g STRAIN=6.0X10^{-4}

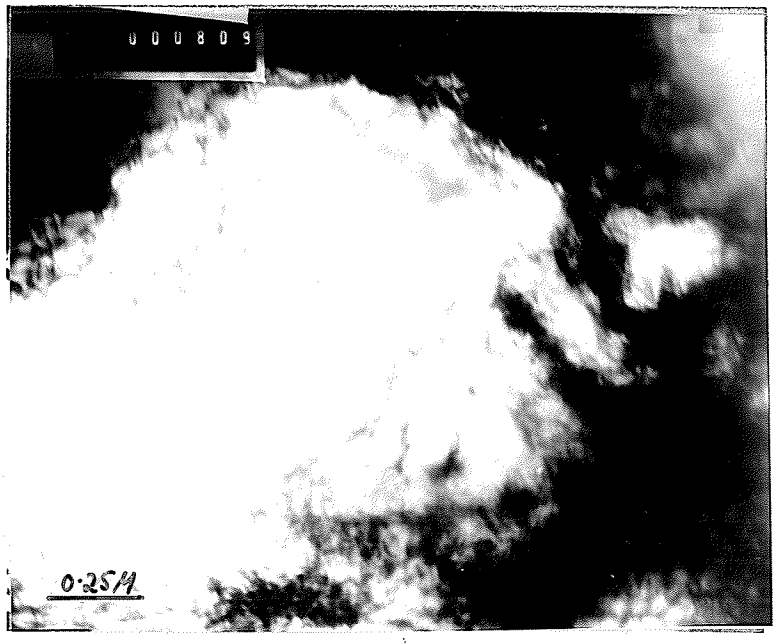

FIG.16h STRAIN=6.0X10^{-4}

The cell formation, at a strain of 6.0×10^{-4}, which was absent up to a strain of 3.0×10^{-4}, can be seen in Figs. 16g and 16h.

3.2.1.1.2.7 $\varepsilon = 45.0 \times 10^{-4}$

The dislocations which have corss-slipped on to the (100) plane of the foil (Fig. 17a) are seen to interact at a strain of 45.0×10^{-4} producing dislocation loops 'A' and point defect clusters 'B'. This kind of dislocation behaviour was not observed in specimens deformed upto 6.0×10^{-4} strain. The existance of dislocation loops 'A', jogs 'B', half moon contrast 'c' and dipoles 'D' in Fig. 17b suggests that point defects are produced by the pinching of dipoles. Fig. 17c shows dislocation structure of the grain boundaries 'A' and also the heavily tangled dislocations adjacent only to the grain boundary 'B'.

The general nature of the dislocation entanglement at 45.0×10^{-4} strain is represented by Figs. 17(d-f). These electron micrographs are from adjacent areas and therefore suggest that the extent of tangling is widespread but, the general nature of entanglement is similar to that in specimens deformed up to a strain of 6.0×10^{-4}. Heavily kinked dislocations, in Fig. 17g, were also seen on (100) plane, i.e. the plane of the foil.

A pair of stacking faults is seen to emerge from the grain boundary in Fig. 17h. The difference between this electron micrograph and the previous electron micrographs showing stacking faults is the dislocation activity in areas surrounding the faults. The cell formation at this strain of 45.0×10^{-4} appears to be

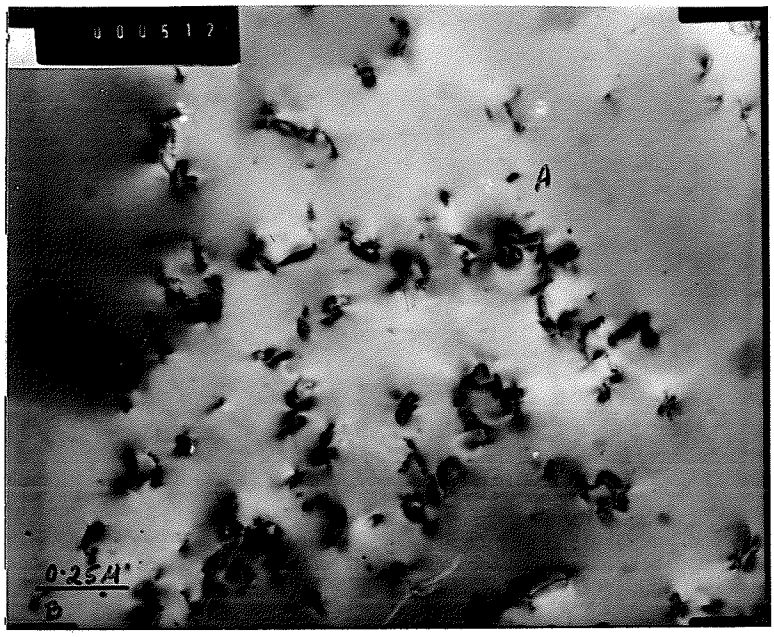

FIG.17a STRAIN=45.0×10^{-4}

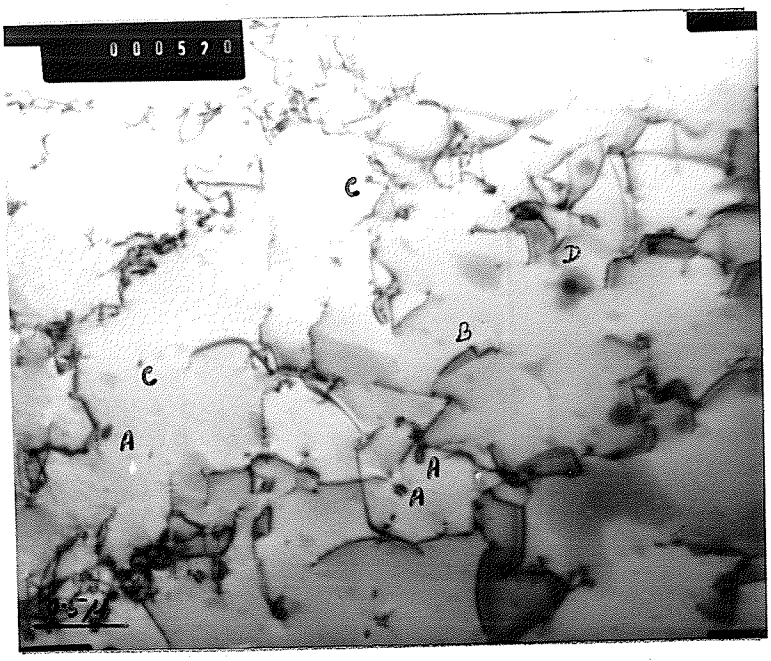

FIG.17b STRAIN=45.0×10^{-4}

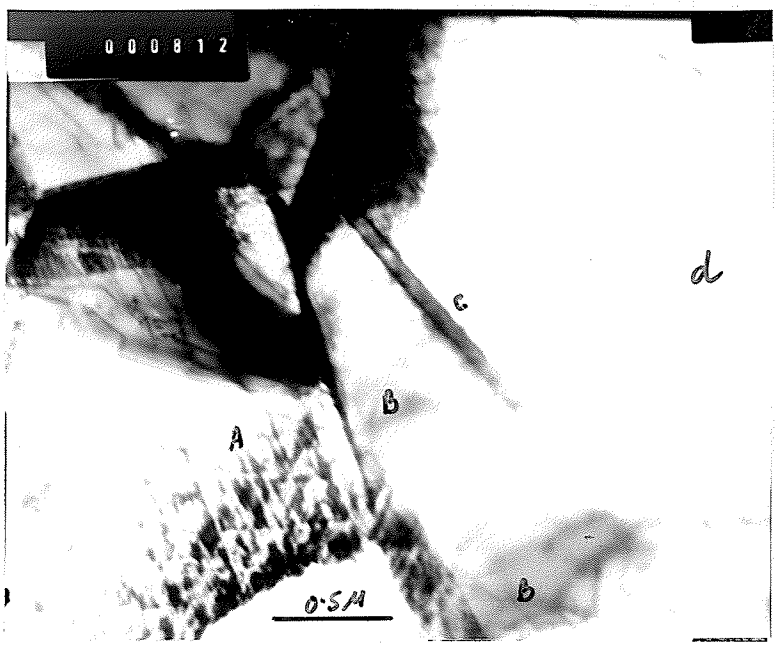

FIG.17c STRAIN=45.0X10^{-4}

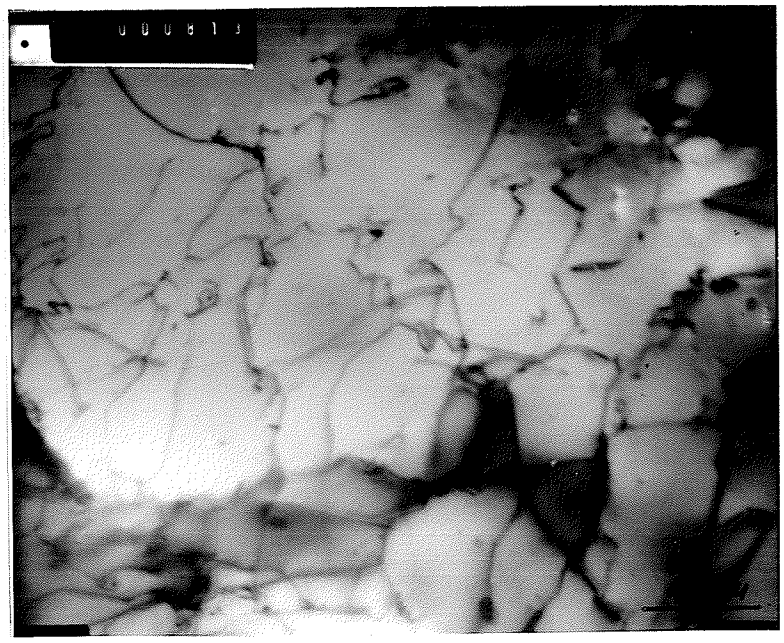

FIG.17d. STRAIN=45.0X10^{-4}

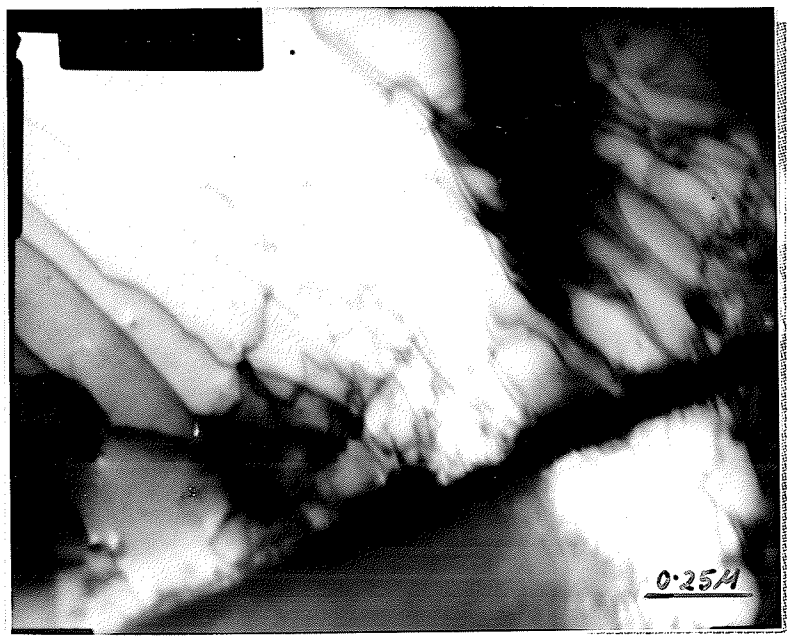

FIG.17e STRAIN=45.0X10^{-4}

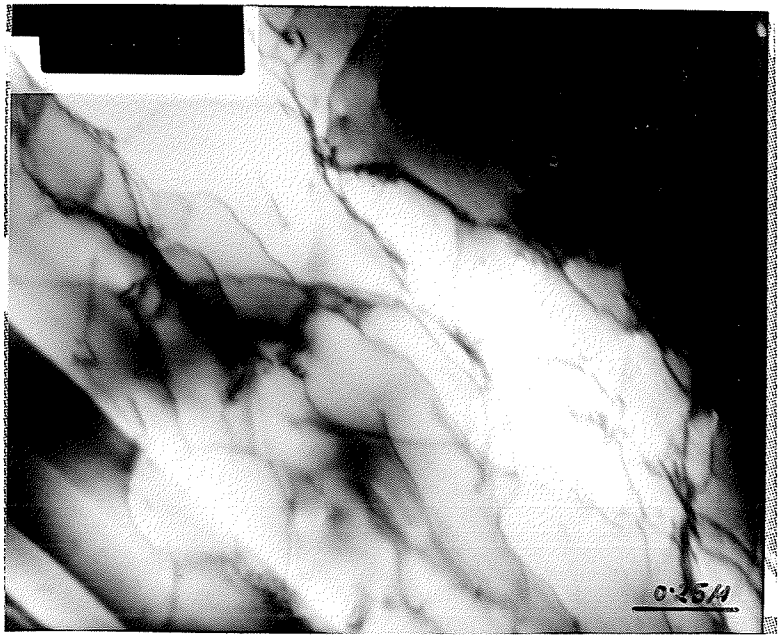

FIG.17f STRAIN=45.0X10^{-4}

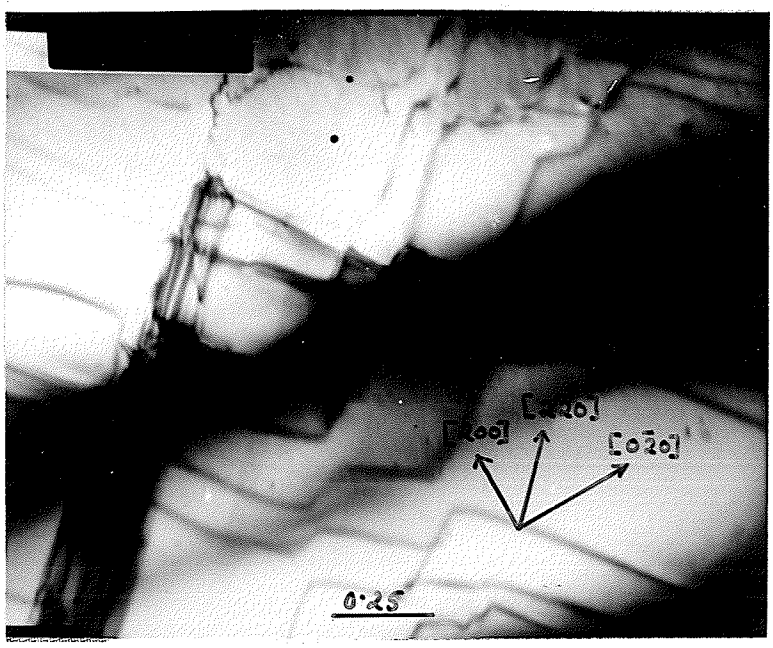

FIG.17g STRAIN = 45.0×10^{-4}

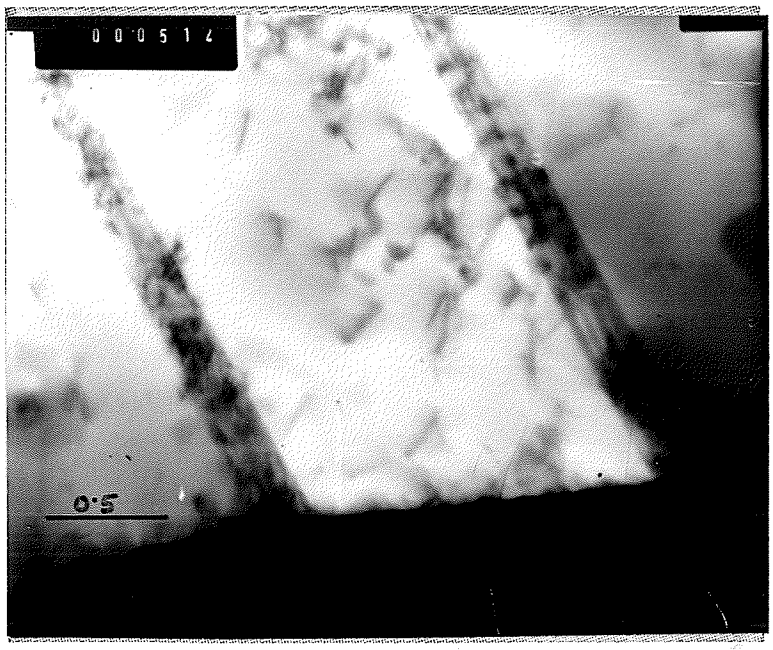

FIG.17h STRAIN = 45.0×10^{-4}

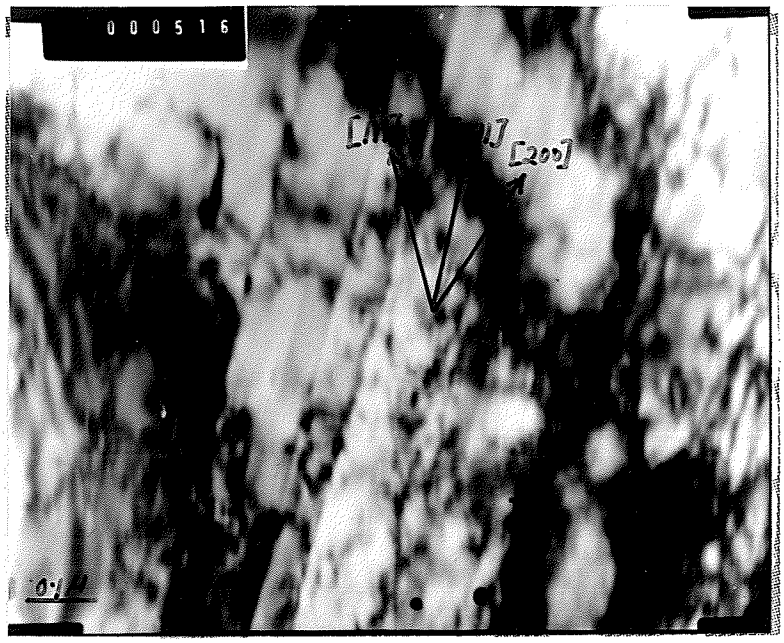

FIG. 17i STRAIN = 45.0×10^{-4}

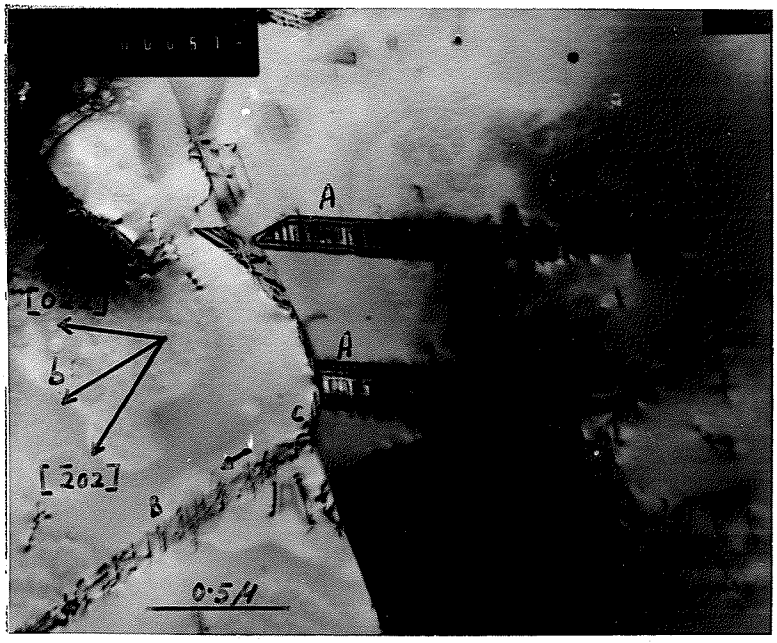

FIG. 17j STRAIN = 45.0×10^{-4}

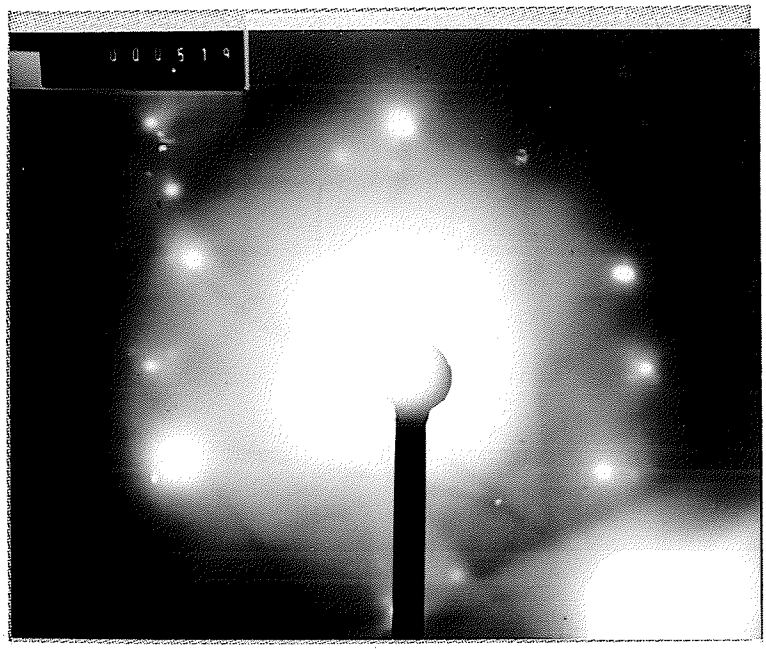

FIG.17k STRAIN=45.0X10^{-4}

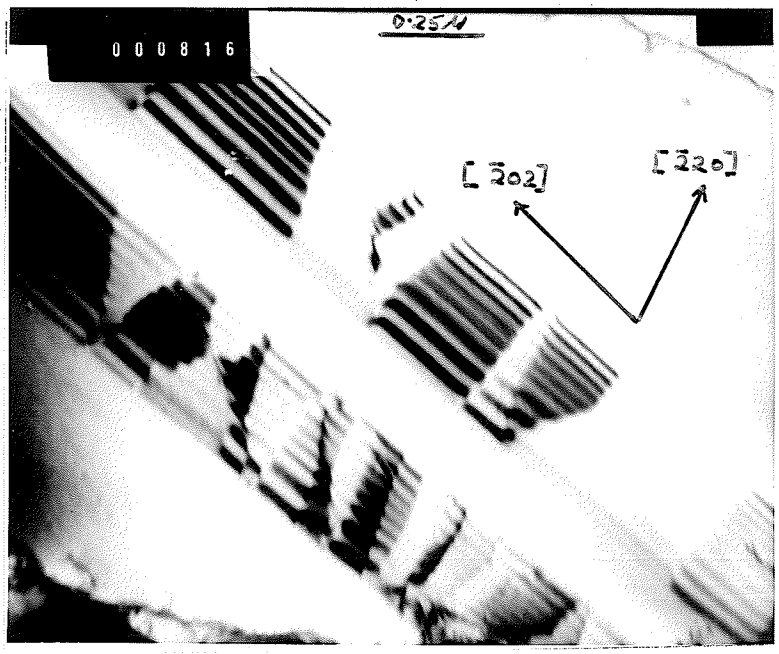

FIG.17l STRAIN=45.0X10^{-4}

widespread Fig. (17i) as compared to the specimens deformed up to a strain of 6.0×10^{-4}.

Figure 17j shows deformation twins at 'A' and probably an early stage of stacking fault formation at 'B', all originating at a grain boundary. The twin reflections from the deformation twins are shown in Figure 17k. The origin of the twins at the grain boundary, where it is curved and lying along $[2\bar{2}0]$, suggest that these are produced by the migration of twinning dislocations on adjacent {111} twinning planes[26]. Their passage results in the formation of an intrinsic stacking fault on every {111} plane and hence the formation of deformation twins. The foil plane is (111) and the dislocations on the slip plane 'B' have come out of the grain boundary at 'c'. These dislocations are not the normal lattice type dislocations[33] and are considered to be partials. The movement of these partials in the direction indicated is considered to be the mechanism for stacking fault generation.

A pair of overlapping stacking faults is seen in Fig. 17ℓ. The foil plane is (111) and since the faults are lying along $[\bar{2}02]$, the fault plane was found to be $(1\bar{1}1)$.

In summary, the more significant results of this electron micrographic study are as follows:

1. Up to a strain of 3.0×10^{-4} there was no appreciable increase in dislocation density, but beyond the strain of 4.0×10^{-4} dislocation density increased appreciably.
2. The amount of dislocation entanglement up to 3.0×10^{-4} strain was not appreciable, as compared to that beyond a strain of 4.0×10^{-4}.

However, at all levels of strains, some dislocation activity and entanglement in some restricted areas was observed. Thus it may be concluded that dislocation mobility is present even at a strain as low as 1.0×10^{-4}.

3. The appearance of dislocation loops, jogs on dislocations and point defect clusters at a few of the localized areas, even at a strain of 0.01%, suggests that point defects are produced at very low tensile deformations. The mechanism of their production is discussed in section 4.1.

4. Single stacking faults, overlapping stacking faults and deformation twins were produced during tensile deformation as low as 1.0×10^{-4}.

5. Grain boundaries (Fig. 11c and 17j) and twin boundaries (Fig.14a) were observed to act as dislocation sources.

6. The stacking faults were seen to originate either;

   a) at grain boundaries (Figs. 10c, 13b and 17h)

   b) at twin boundaries (Fig. 15e) and

   c) at the intersection of slip planes (Fig. 14b).

7. The first appearance of cell formation was observed at a strain of 4.0×10^{-4}. The electron micrographs in Figs. 14i and 14j are in support of the above observation.

8. The appearance of cross-grids of dislocations within the cell walls of Fig. 14j suggests that the cell walls exert hydrostatic stresses on the matrix surrounding these walls.

3.2.2 Tensile Stage Electron Microscopy

In situ deformation studies were performed on the thin foils of nickel. The Philips EM300 tensile stage was used. Specimens were pulled and examined at ~-130^{o} C so as to avoid specimen heating.

3.2.2.1 Results and Interpretation

Figures 18(a-i) show the successive stages of increasing tensile deformation. The amount of strain could not be measured accurately, but the maximum strain was found to be about 1 pct. A careful examination of these electron micrographs leads to the following conclusions.

1. As the specimen is deformed, the dislocations start moving and run into obstacles (in general other dislocations) initiating the process of tangling. The increasing amount of entanglement with increasing strain is evident from this series of electron micrographs.

2. The point defects are produced by the movement of dislocations with jogs on them. The jogs at 'A' and defect clusters at 'B' are seen in Figs. 18(f-h). As we increase the tensile stress the dislocations bow out e.g., at 'c' in Figs. 18(f,g and h) and the decreasing radius of curvature with increasing stress is clear from the above set of figures. Dislocations bow out because it is difficult to move the jogs on them. The point defect clusters, left behind these moving dislocations with jogs, are seen at 'B'

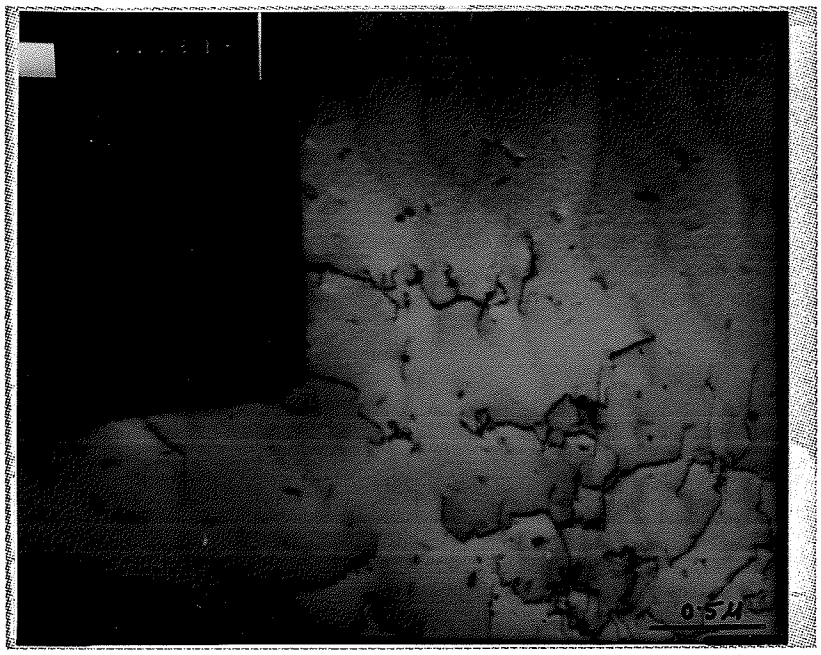

FIG.18a

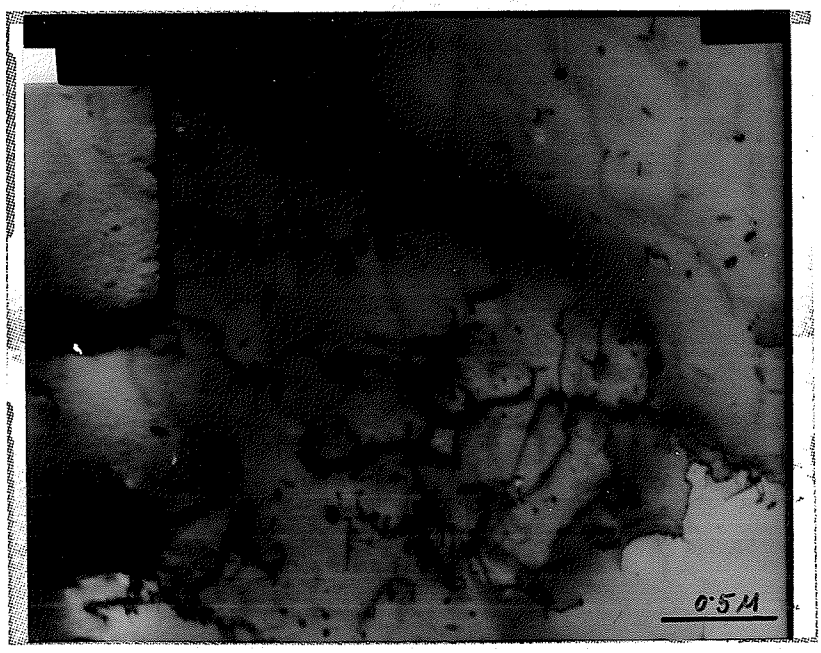

FIG.18b

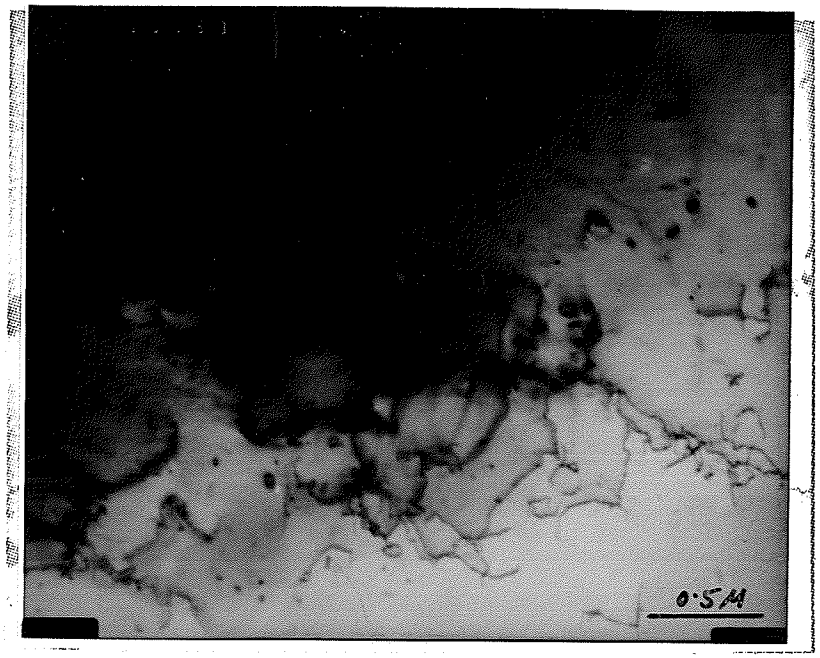

FIG.18c

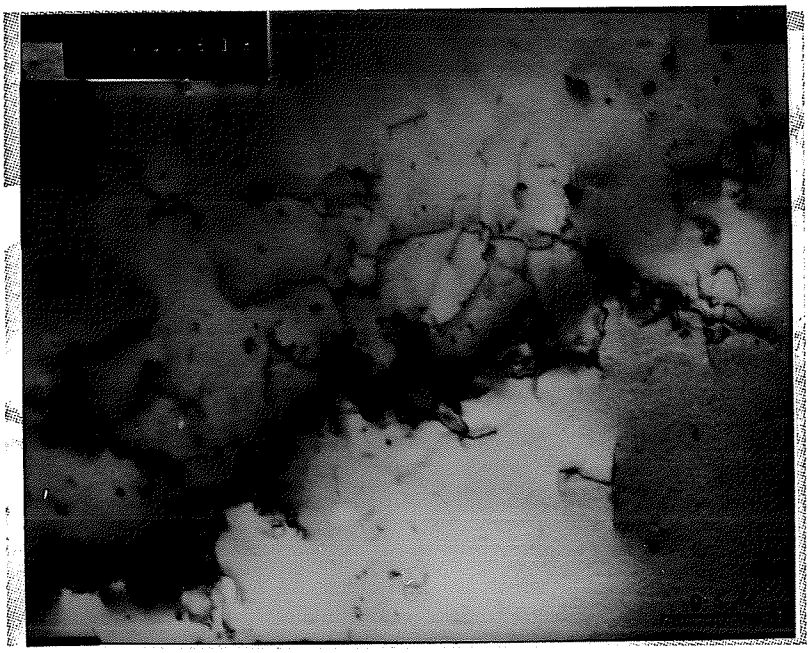

FIG.18d

FIG.18e

FIG.18f

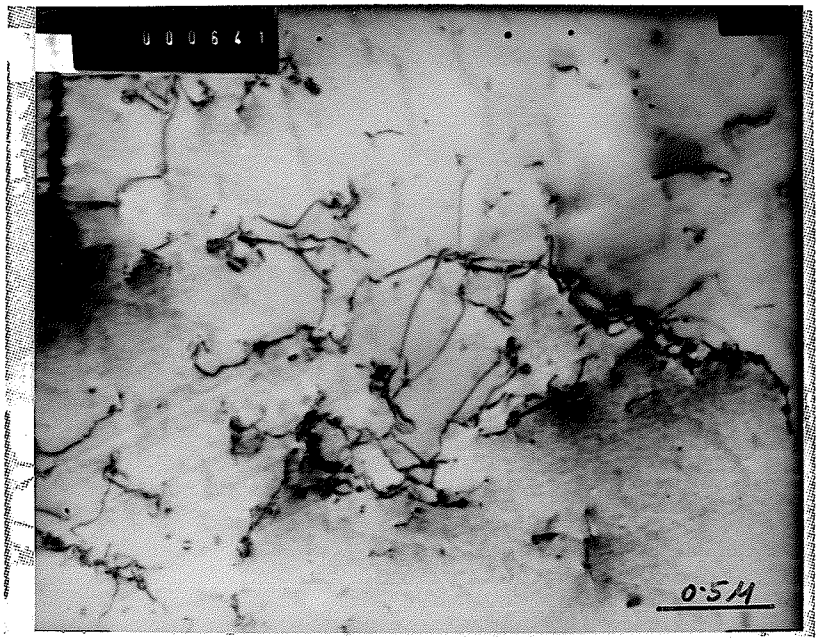

FIG.18g

FIG.18h

FIG.18i

and these are produced by the attraction between the dipoles produced during the course of dislocation movements.

3. Attention may be drawn to the presence of point defect clusters within the grains at 'D' and their absence near the grain boundaries. As the point defects are produced due to dislocation movement, the above experimental observation suggests that dislocation movement is more predominent in areas removed from the grain boundaries.

4. The formation of dislocation cells in thin foils deformed in the microscope was not observed. This is not surprising in view of the fact that the dislocations and point defects generated during deformation of a thin foil are easily lost to the foil surface and thus are not available for the formation of cell structure.

3.3 Tensile Test Results and Interpretation

To gain a better understanding of the types of lattice defects generated during deformation in the microplastic region and their interactions, specimens were deformed to a strain of 1.0×10^{-4}, 2.0×10^{-4}, 3.0×10^{-4}, 6.0×10^{-4} and 45.0×10^{-4} respectively and aged for 60 hours at $20^{o}C$. The yield stress of these prestrained and aged specimens was then determined for 0.009% offset. The results are shown in Table 9.

Table 9

Specimen No.	Prestrain	0.009 pct Offset Yield Stress (Psi)
6	0	3.13×10^{3}
7	1.0×10^{-4}	3.35×10^{3}
8	2.0×10^{-4}	4.40×10^{3}
9	3.0×10^{-4}	4.50×10^{3}
10	6.0×10^{-4}	5.30×10^{3}
11	45.0×10^{-4}	6.60×10^{3}

A plot of yield stress vs prestrain is given in Fig. 19. These data were replotted on a log-log scale, as shown in Fig. 20. The least square fit for a straight line for the experimental data given in Table 9, as shown in Fig. 20 gives the following relationship:

$$\sigma_{\gamma} = 16.5 \times 10^{3} \varepsilon^{0.16} \qquad 3.3.3.1$$

The nature of the plot in Fig. 19 suggests that there is a rapid increase in the yield stress during the initial stage but as the magnitude of prestrain is increased the rate of increase in yield stress decreases. This may be explained by the point and

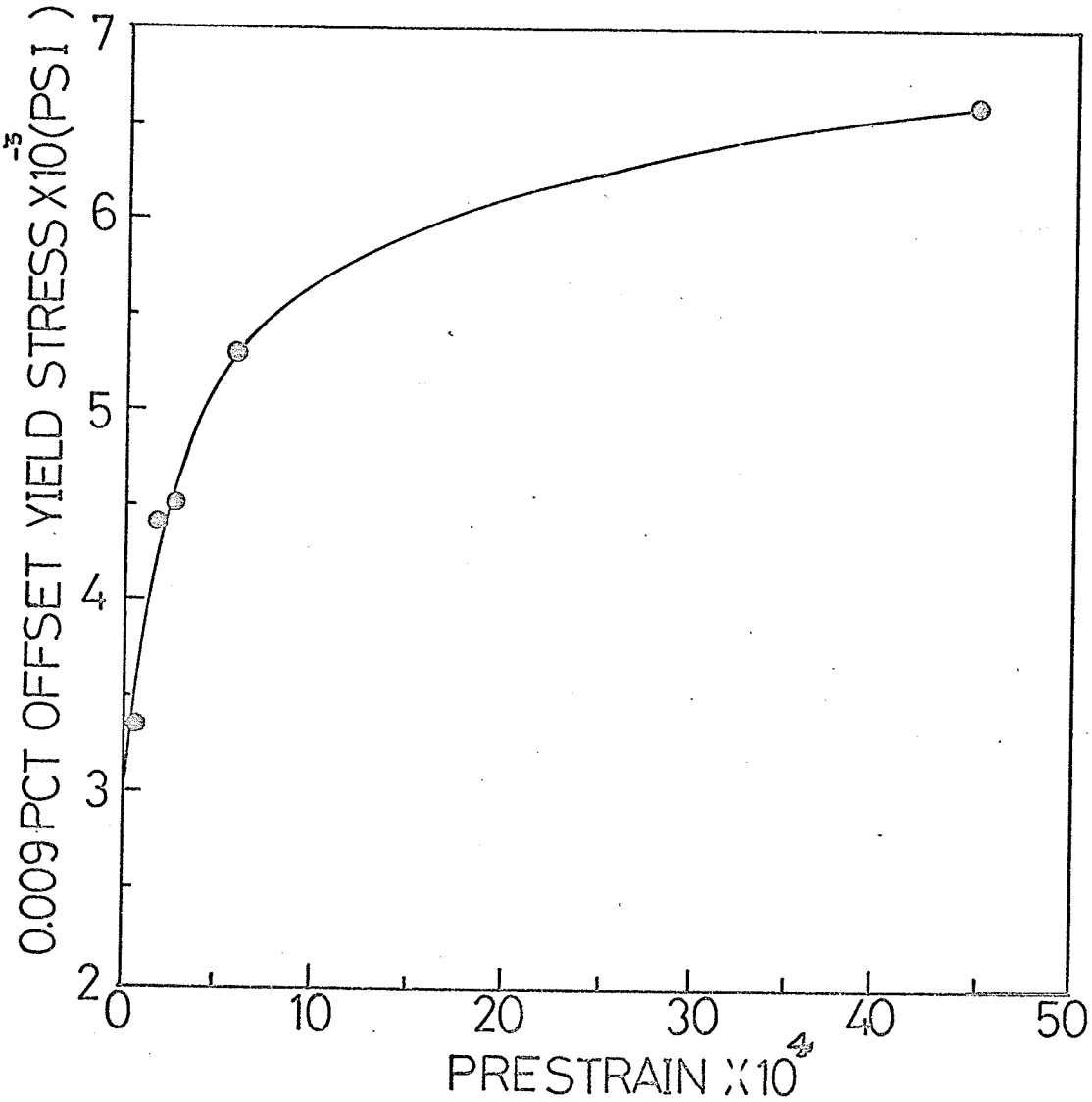

FIG. 19 YIELD STRESS VS PRESTRAIN IN POLYCRYSTALLINE NICKEL

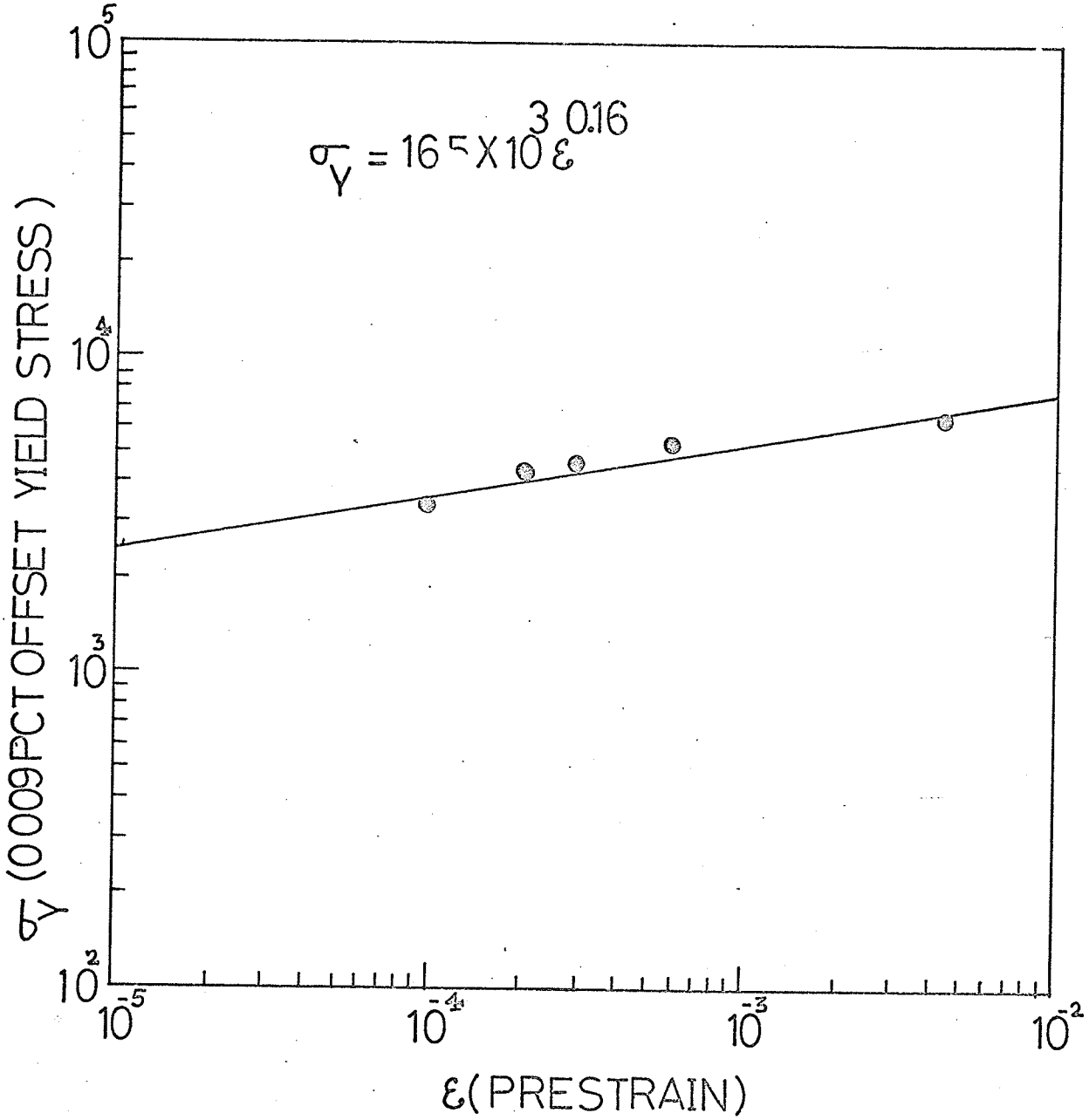

FIG. 20 YIELD STRESS VS PRESTRAIN IN POLYCRYSTALLINE NICKEL

line defects generation and interactions as observed during electron microscopic examination. Since all the specimens were aged for 60 hours after tensile deformation, the point defects generated during deformation are expected to be annealed out as was suggested in section 3.1. As such the only defects left after room temperature ageing are dislocations and a few stacking faults. Therefore the rapid increase in the yield stress at low values of pre-strain (Fig. 19) is ascribed primarily to the interactions of new dislocations with the pre-existing dislocations produced during prestraining. The rate of dislocation entanglement in the initial stages (Fig. 19), is very high because of the higher dislocation mobility of pre-existing (mostly untangled) dislocations. But with increasing prestrain the density of free (mobile) dislocations decreases resulting in a slower rate of tangling. This decreased tangling rate results in the decreased rate of yield stress increase. A small increase in the yield stress at higher prestrains is attributed to the dislocation entanglement in a few of the grains and also further entanglement in regions already containing tangles. The formation of tangles in tangle free grains, as mentioned above, suggests a non-uniform dislocation distribution as observed experimentally during electron microscopic examination.

From the above discussion of tensile test data following conclusions could be made.

1. The higher rate of dislocation entanglement during the initial stages of the deformation process may be attributed to the higher dislocation mobility.

2. From the yield stress data it is concluded that the dislocation distribution during tensile deformation of polycrystalline nickel is non-uniform.

3. The variation of yield stress 'σ_γ' with prestrain 'ε' in polycrystalline nickel may be given by the following equation:

$$\sigma_\gamma = 16.5 \times 10^3 \, \varepsilon^{0.16}$$

4. A significant increase in yield stress, even at 1.0×10^{-4} prestrain, suggests that there is an appreciable dislocation activity even in the very early stages of tensile deformation.

4. DISCUSSION

4.1 Nature of Line and Point Defect Generation and Their Interactions in the Microplastic Region of Nickel

4.1.1 Nature of Line Defects and Their Interactions

The generation of point defects during deformation requires apriori presence of mobile deslocations with jogs. In the initial stages of deformation, apart from other sources, grain boundaries may also act as a source of dislocations. In the present investigation, the dislocation density within the grains was observed to increase at strains as low as 1.0×10^{-4}. However, the complete recovery of resistivity due to room temperature ageing suggests that a re-arrangement of dislocation in the grain boundaries takes place without altering the overall average density of dislocations.

The mechanisms, by which, grain boundaries function as sources of dislocation have been described by Hornbogen et al.[33] who proposed two different generation mechanisms: the first occurs when the grain boundary is mobile, while the other is responsible for the creation of dislocations in stable grain boundaries. In mobile grain boundaries (boundaries which exhibit shear at low temperatures under the influence of external stress) dislocations exist which move along the boundary (grain boundary dislocations, GBD). The shearing of grain boundaries depends on the movement of GBD. The GBD can move by slip along the flat regions of grain boundaries. This can extend over the edge of a grain boundary only when the Burgers vector of GBD changes. Thid change takes place by a dislocation reaction in which the lattice dislocation is

separated. This separation of lattice dislocations from GBD is the mechanism by which mobile grain boundaries function as dislocation sources. This is confirmed by electron microscopic examination. They have shown also that this mechanism is responsible for the crossing of slip lines by grain boundaries. The following generation mechanism operates in stable boundaries. These boundaries can act as sources of dislocation only when two slip planes intersect along the grain boundary. The boundary emits dislocations alternately into the two slip planes, their Burgers vector lying so that no shearing of the grain boundaries sets in. This mechanism is also confirmed by electron microscopic examination.

A schematic diagram, after Hornbogen et al.[33], showing the nature of operation of the first kind of source is shown in Fig. 21. It is clear that an edge dislocation of Burgers vector 'b' is generated on the slip plane 'A', where the grain boundary changes its direction and hence the grain boundary dislocation also changes its Burgers vector. This suggests that this will generally happen near the bends on the grain boundaries. This mechanism seems to operate in pure nickel as evidenced by Fig. 11c, which shows a source 'A' at the curved region of the grain boundary G. The pile up of dislocations in the slip planes 'B' is clearly visible. The same type of emission of dislocations by grain boundary can be seen at 'c' in Fig. 17j. The slip plane 'B' intersects the grain boundary along the $[1\bar{1}0]$ direction, where it is acting as a source of dislocations. This supports the idea of Hornbogen et al.[33] that for a grain boundary to act as a source it should meet some slip plane along a suitable crystallographic direction.

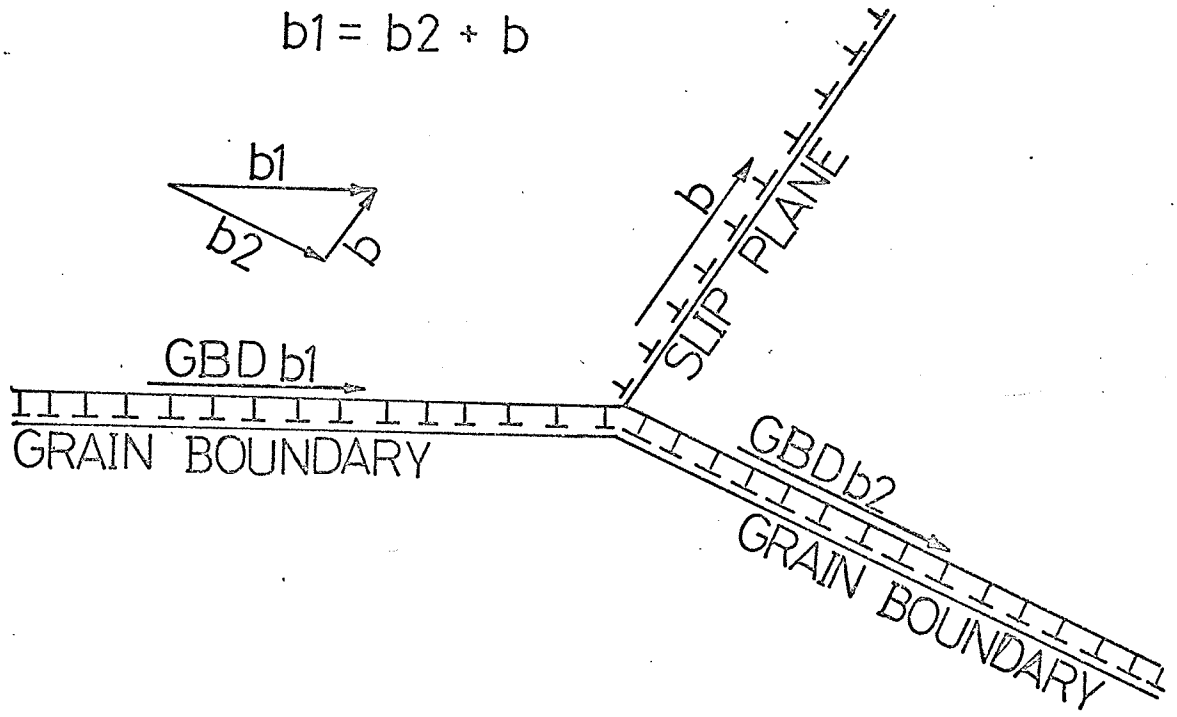

FIG. 21 SCHEMATIC DIAGRAM REPRESENTING THE GENERATION OF LATTICE DISLOCATIONS (b) FROM THE GRAIN BOUNDARY DISLOCATIONS (b1)

Apart from the grain boundaries, twin boundaries were also observed to act as dislocation sources as described earlier in section 3.2.1.1.2.4.

Once dislocations are generated they start to interact and as the interaction progresses, dislocation tangles are formed which ultimately result in subcell formation.

The nature and origin of dislocation tangles have been discussed by Kuhlmann-Wilsdrof et al.[34]. According to them, dislocation tangles are three dimensional dislocation arrays frequently forming cell walls or ill-defined zones parallel to possible slip planes, but these arrays are never confined to one or a few closely packed slip planes. As is clear from the electron micrographs of pure nickel, the tangles are always associated and interspersed with small dislocation loops, probably prismatic in character.

In pure FCC metals, tangles are formed under almost any circumstances, except when they are strained as thin foils (see section 3.2.2).

Kuhlmann et al.[34] have considered three basic mechanisms to explain dislocation tangling; namely (1) dislocation intersection jogs, (2) cross-slip, and (3) intersection between dislocations and point defects. They have suggested that tangles must be caused by an effect which not only allows the dislocations to move out of their slip planes but which, at the same time, provides resistance against glide. They have presented arguments to the effect that neither cross-slip nor intersection jogs alone can lead to the

formation of tangles. Their arguments against cross-slip are three fold: cross-slip is observed extensively in thin foils of Al, but no true tangling ever takes place in foils of Al while strained in the electron microscope. Also, cross-slip is known to be virtually absent in stages I and II (a typical stress-strain curve for single crystals deformed in tension contains three distinct regions or stages. The stage I refers to easy glide, stage II to linear hardening and stage III refers to the region where recovery takes place) of Fcc pure metal crystals.[36] Nonetheless, the tangles seen in Al deformed at room temperature in stages I, II and III are qualitatively alike, except that in stage III they resemble markedly to cell walls. Thirdly it is impossible to conceive what could cause dislocations to cross-slip without any visible obstacle if this cross-slip could happen in response to the applied stresses without any assistance from thermal activation[35].

In the present investigation on polycrystalline nickel foils deformed in the microscope, dislocation tangles were observed (section 3.2.2). As such, it is suggested that the absence of tangling in their single crystal specimens deformed in the electron microscope could be due to the easy excape of dislocations to the foil surface (due to image forces). Cross-slip may not be present in stages I and II in case of single crystals deformed in a particular orientation, but, in the case of polycrystalline material, due to the complex nature of stresses arising from grain boundaries, cross-slip is bound to be present. The grain boundaries certainly act as the obstruction to the movement of dislocations and hence

will assist cross-slip.

In light of the above, it may be assumed that cross-slip does play a relatively important role in the formation of dislocation tangles in polycrystalline materials. Similar arguments may also be made for the relatively greater importance of intersection jogs in polycrystalline materials as compared to that in single crystals.

The third mechanism, i.e. intersections between point defects and dislocations, according to Kuhlmann et al.[34], is basically responsible for the dislocation tangling. They argue that point defect concentration by plastic deformation, at intermediate temperatures, represents a very high supersaturation, even after a strain of 1 pct. or less. Again the occurance of well defined dislocation loops in quenched FCC metals on {111} or {110} bounded by <110> or <112> directions, which are formed by the condensation of vacancies[37], shows that dislocation "climb" can be considered from two different view-points. On the one hand, one may consider the condensation of point defects simply as a means which allows dislocations to move (by climb) in response to stresses normal to their slip planes and thus to circumvent obstacles which block their progress by glide. Conversely one can consider dislocation "climb" to be the by-product of point defect precipitation, which takes place primarily in order to reduce the free-energy of the metal, and only incidently creates dislocations or moves them out of their slip planes. By simple energy calculations it has been shown [34] that dislocation "climb" is far more

likely to happen by the point defect condensation rather than due to mechanical stresses.

The climb, resulting from the condensation of defects on to the dislocation, is highly non-uniform and blocks the dislocation glide. Now, as the external stress is increased, the dislocation segments in nearly screw orientation may cross-slip and all of the above mentioned processes may occur to cause tangling. Thus, it is seen that condensation of point defects produced during deformation plays an essential part in the formation of dislocation tangles.

In the case of polycrystalline nickel, electron microscopic observations suggest that all of the three above mentioned processes are operative. In the initial stages of deformation cross-slip and intersection jog mechanisms are responsible for the dislocation interactions. The point defects are generated, primarily due to the jogs on the dislocatons. But as the stress is increased more and more of point defects are created and these interact with dislocations and hinder their movement. Whereas some segments of the dislocations are pinned, the unpinned segments start acting as dislocation sources. The extensive tangling observed after a strain of 3.0×10^{-4} supports these ideas.

4.1.2 Nature of Point Defects and Their Generation

Several mechanisms have been proposed for the generation of point defects during plastic deformation. Seitz[38] and Mott[39] suggested that a plastic strain, ε, produces a concentration 'c_v' of vacancies of the order of

$$c_v \cong 10^{-4}\ \varepsilon \qquad 4.1.2.1$$

On the other hand, van Bueren and Jogenburger[40] have emphasized that the resistivity change $\frac{\Delta\rho}{\rho}$ varies with elongation $\frac{\Delta\ell}{\ell}$ as

$$\frac{\Delta\rho}{\rho} \simeq \left(\frac{\Delta\ell}{\ell}\right)^{3/2} \qquad 4.1.2.2$$

the proportionality factor being of the order of unity. van Bueren[41] has connected this observation with a theory in which expanding dislocation rings develop jogs on them at a rate proportional to the area of slip plane swept by the rings, and in which these jogs produce point defects at a rate proportional to the distance they move through the slip plane. From this analysis the concentration of point defects is expected to vary as

$$c \propto \varepsilon^{3/2} \qquad 4.1.2.3$$

in accordance with the resistivity measurements.

Another mechanism after Friedel[42], in which two arms of a Frank - Read source may often lie in neighbouring glide planes and may coalesce at the end of each cycle of operation of the source. As a result, a line of point defects is formed, the number of which is of the order of ℓ/b where 'ℓ' is the length of the source and 'b' is the atomic spacing. Each time the source operates, ℓ/b defects are created, so that the concentration 'c_v' produced by N cycles

of operation per unit volume is given by

$$c_v \simeq \frac{\ell}{b} v N \qquad 4.1.2.4$$

where $v(\simeq b^3)$ is the atomic volume. If the area swept by each dislocation ring is 'L^2', the plastic strain is given by $\varepsilon = L^2 bN$; hence

$$c \simeq \frac{\ell b}{L^2} \varepsilon \qquad 4.1.2.5$$

Making the reasonable assumption that $L \simeq 3\ell = 3 \times 10^4 b$, this gives

$$c \simeq 10^{-5} \varepsilon \qquad 4.1.2.6$$

which is comparable with the estimates of Seitz[38] and Mott[39].

None of the above mechanisms, representing theoretical possibilities, seem sufficient to explain the results obtained for polycrystalline nickel. The point defect (vacancies) concentration 'c_v' was found to depend on strain 'ε' according to the following relation

$$c_v = 4.54 \times 10^{-3} \varepsilon^{0.36} \qquad 4.1.2.7$$

The results suggest that the production of point defects is a complex process consisting of a variety of mechanisms operating simultaneously or in succession. The experimental evidence suggests that the point defects and dislocation loops are produced by the movement of jogs on screw dislocations and the attractive junction of the dipole configuration respectively. These mechanisms are represented by the sketches in Figure 22.

Both of these mechanisms are essentially the same. Case (1) refers to jogs of one or two atomic distances in height whereas case (2)

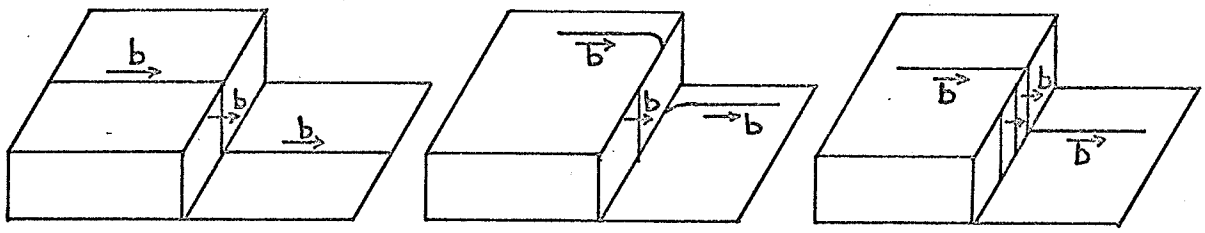

(a)

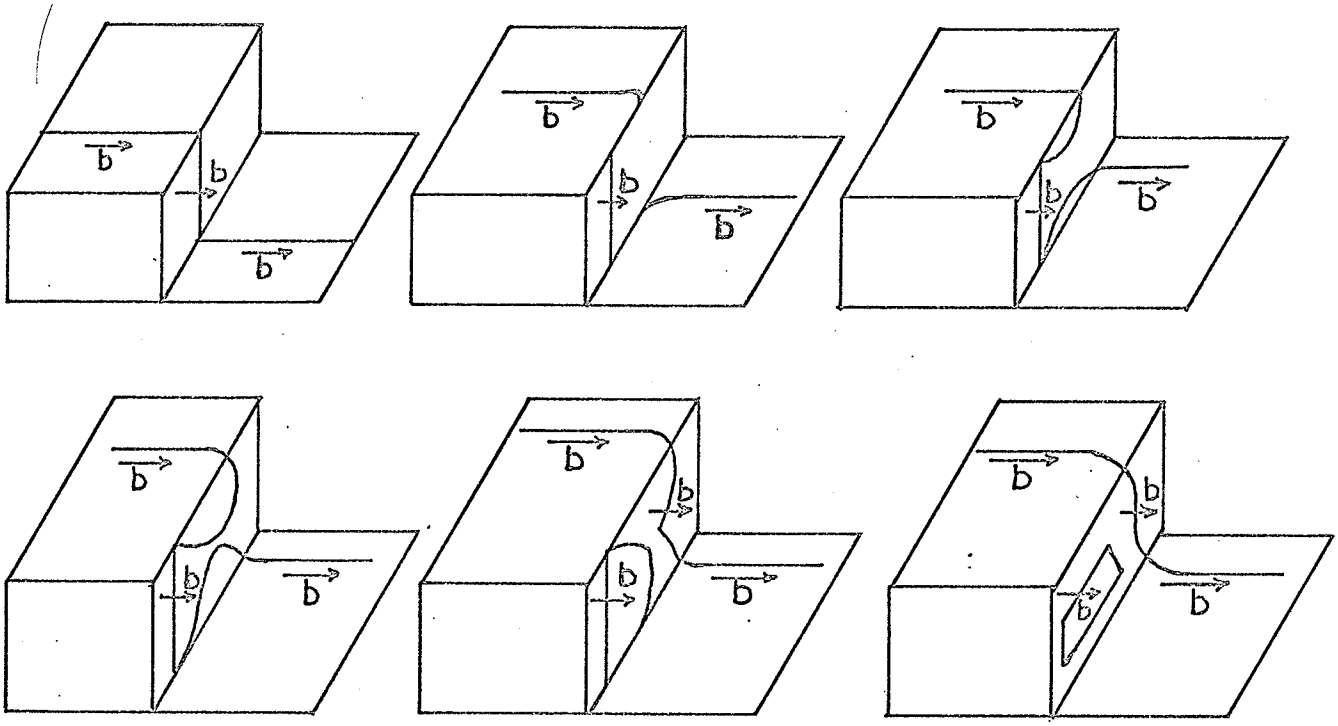

(b)

FIG. 22 SCHEMATIC DIAGRAM REPRESENTING SUCCESSIVE STAGES OF (a) POINT DEFECT AND (b) DISLOCATION LOOP GENERATION DURING MOVEMENT OF JOGGED DISLOCATIONS.

refers to jogs of considerably greater height. However, once mechanism (2) has operated, the jog height is decreased to the extent that this mechanism ceases to operate and the conditions are made favourable for the operation of mechanism one again.

Apart from the above mechanisms for point defect production, mention may also be made of another mechanism arising from the "uncertainty principle for dislocation axes[34]". According to this, it is not possible to define with precision the axis position of a dislocation and as such that of a slip plane. As a result, a moving dislocations transfer smaller or larger segments to neighbouring slip planes creating complex jogs. As these jogs cannot move conservatively, point defects are generated during the movement of these jogged dislocations. When a moving edge dislocation changes its slip plane, a row of point defects is produced whereas in the case of a screw dislocation only single point defects are generated.

In conclusion, grain boundaries and twin boundaries act as sources of dislocations which are active in the initial stages of deformation. The intractions among these dislocations are by the 'cross-slip' and the 'intersection jog' mechanisms. However, in the later stages of deformation, point defects and dislocation loops are created which are responsible for enhanced dislocation activity resulting in cell formation. At very low strains, point defects are produced by the movement of jogs which are formed on moving dislocations due to their intersections and axis uncertainty.

4.2 Nature and Origin of Residual Lattice Strains in Pure Polycrystalline Nickel

It was observed that residual lattice strains (RLS) become significant only after a strain of 3.0×10^{-4}. This observation is in agreement with the earlier work of Swaroop and Tangri[13].

A careful examination of the electron micrographs reveals that dislocation activity increases appreciably beyond a strain of 3.0×10^{-4}. This increased dislocation activity results in enhanced dislocation tangling and ultimately cell formation at a few places as shown in the electron micrograph (Figure 14j) of a specimen deformed to a strain of 4.0×10^{-4}. These observations support the earlier suggestion[13] that the RLS is intimately related to the dislocation substructures produced during deformation. These substructures, in turn, produce stresses which are expected to be hydrostatic in nature. A careful examination of the dislocation arrangement inside the cells (Figure 14j) reveals the presence of cross-grids of straight dislocations. It is proposed that these grids are formed due to the hydrostatic nature of stresses arising from the cell walls.

To determine the total strain at which RLS first makes its appearance, specimens were loaded up to various strains and unloaded instantaneously. The results are given in Table 10.

Table 10

Sp. No.	Trial No.	Stress 10^3(psi)	Strain μ(in/in)	2 θ (420)	d A^o	$\Delta d \times 10^4$
13	1	0	0	155.69	0.78792	- -
13	2	1.99	110	155.67	0.78795	+0.3*
13	3	0 loaded	0	155.69	0.78792	0.0
14	1	0 unloaded	0	155.66	0.78796	-
14	2	3.047 loaded	190	155.664		-0.1
				155.671	0.78795	
14	3	0 unloaded	26	155.66		+0.1
				155.65	0.78797	
14	4	4.27 reloaded	308	155.687		
				155.689	0.78792	-0.4
				155.686		
14	5	0 unloaded	90	155.649	0.78798	+0.2
				155.670	0.78795	-0.1

*This unexpected change in 'd' spacing could be attributed to the mishandling of the specimen.

From the data it can be concluded that a significant level of the residual lattice strain develops only after a total strain of 3.0×10^{-4}. Therefore the simultaneous appearance of cell formation and residual lattice strain after a strain of 3.0×10^{-4} confirms that cell walls are responsible for the RLS in polycrystalline nickel.

The nature of RLS in instantaneously unloaded specimens was observed to change sign during subsequent room temperature ageing (Specimen 14 of Table 10, trial n0. 5). This could be explained by the mechanism proposed by Tangri et al[13]. It is seen that point defects are produced during tensile deformation of pure nickel. In view of the above, the nonequilibrium concentration of point defects

produced during room-temperature deformation of nickel is expected to acuse a general expansion of the lattice. Assuming that the effect of instantaneous unloading is analogous to that of quenching, a net tensile strain, as experimentally observed, may be expected if the general expansion resulting from the presence of point defects in the lattice is more than the compressive strain due to the residual stress system developed by the substructure walls and the matrix. It can then be easily seen that on subsequent ageing at room temperature the expansion of the lattice will progressively decrease with the progress of room temperature recovery, until a compressive strain similar to that observed during the gradual unloading of a specimen is again observed.

4.3 Deformation Faulting in Pure Polycrystalline Nickel

Considering the electronic structure there is no reason why nickel, situated between cobalt (γ = 10 erg/cm^2) and copper (γ = 40 erg/cm^2) in the periodic table, should have a high stacking fault energy, as suggested by Seeger[43]. The overlap of 3d electrons of neighbouring atoms is small at the end of the third long period, as is the difference in the energy between the stacking orders ABCABC and ABABAB of closed packed planes. In fact Reimer[44] obtained a hexagonal phase of Ni by condensation from the vapour at low temperatures. The large frequency of twins in Ni (supported by micrographs in as annealed specimens) also suggests a low stacking fault energy, because the energy of the twin-boundary is closely related to the stacking fault energy.

Smallman and Westmacott[45] determined the stacking fault probability of nickel to be about half of that for Cu indicating $\gamma_{Ni} > \gamma_{Cu}$. Christian and Spreadborough[46] concluded from line shifts and the change of electrical resistivity with deformation that nickel belonged in a class with Cu regarding its stacking fault energy. Seeger[43], after interpreting the data on the plastic properties of nickel concluded that γ_{Ni} = 80 ergs/cm^2, in good agreement with Haasen's[47] calculated value of 90 ergs/cm^2 by the τ_{III} method.

Overlapping stacking faults were seen[34] to form in polycrystalline, neutron-irradiated nickel during observation in the electron microscope. However, in the present investigation, overlapping stacking faults were observed only in specimens deformed to various strains and never in the fully recrystallized specimens.

This suggests that a small amount of deformation can free the dislocations from their pinning atmospheres, formed during annealing, thus allowing them to dissociate for the formation of stacking faults. In view of the above, it is surprising that stacking fault formation has been observed in irradiated specimens[34].

To determine if the faulting is a result of high stresses produced due to mishandling of the foil, annealed and deformed specimens were deliberately handled severely before examination. The absence of faults in the annealed foil and no increase in the fault density in the deformed foil after deliberate mishandling confirmed that these faults were not formed by the stresses developed during mishandling, but rather due to the stresses developed during tensile deformation. These faults were analysed and found to be mostly overlapping intrinsic faults. As mentioned earlier (section 3.2.1.1.2.1), the contrast analysis of the extreme fringes of these faults, confirmed that these are not microtwins.

A possible explanation for the formation of stacking faults may be developed by extension of Hornbogen et al's analysis of the behaviour of grain boundary dislocations. The dissociation of a grain boundary dislocation into two components, one travelling onto a suitably oriented slip plane while the other is confined to the grain boundary has been discussed earlier. It is reasonable to expect that the Burgers vector of the dislocation sent onto the slip plane will depend upon the Burgers vector of the original grain boundary dislocation as well as the particular orientation

relationship between the available slip plane and the grain boundary. It is proposed that, given a favourable set of these conditions, a grain boundary dislocation will generate suitable partials which during their movement on the slip plane produce stacking fault which are seen to emanate from the grain boundary. The behaviour of grain boundary dislocation (GBD) at a situation where grain boundary meets the slip plane, is schematically represented in Figure 23. The dissociation of GBD into perfect lattice dislocation and another GBD results into the pile up of perfect lattice dislocations on to the slip plane as shown by Figure 23a. This mechanism is seen to operate in pure polycrystalline nickel and is confirmed by the electron micrographs in Figures 11c and 17j. In another situation the orientation relationship may be such that GBD dissociates to form two partial dislocations, one of which could move on to the slip plane and may be connected with other partial (stuck at the intersection of slip plane with the grain boundary) through the stacking fault (Figure 23b). When this type of a dislocation reaction takes place, the area ahead of the intersection of the slip plane and the grain boundary is expected to be denuded of dislocations. A typical area denuded of dislocations due to such a dislocation reaction is shown in Figure 10c.

Similar arguments may be developed for the formation of stacking faults at the twin boundaries as seen in Figures 15(e-i). The experimental evidence to support the above proposed mechanism is the appearance of dislocations 'A' on the slip planes, similar in nature to the dislocations observed near the twin boundary sources

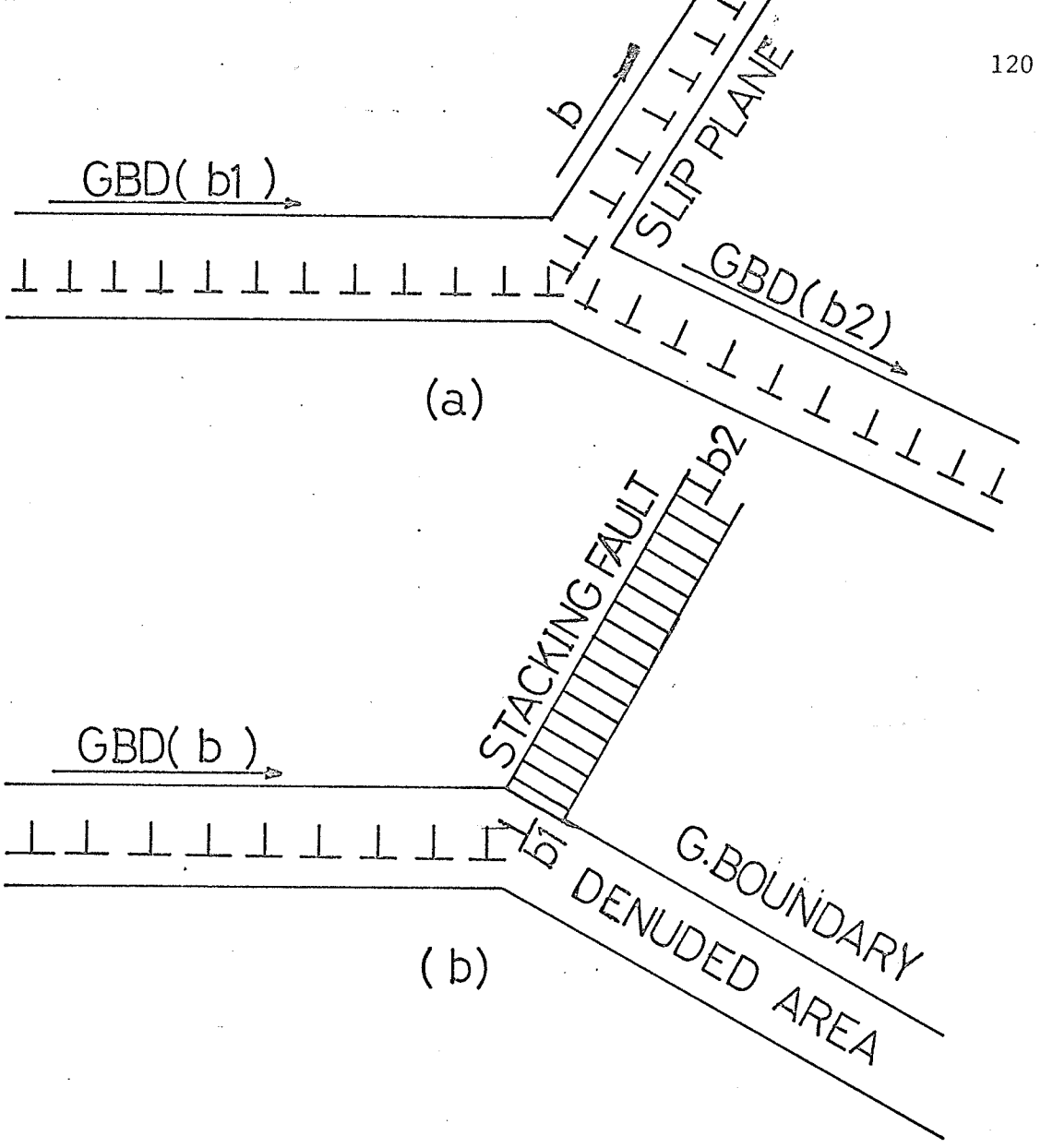

FIG. 23 (a) SCHEMATIC DIAGRAM SHOWING GENERATION OF LATTICE DISLOCATIONS(b) FROM THE GRAIN BOUNDARY DISLOCATIONS(GBD, b1).

(b) SCHEMATIC DIAGRAM SHOWING GENERATION OF PARTIAL DISLOCATIONS 'b1' AND 'b2' FROM THE GBD 'b'. PARTIAL 'b2' HAS MOVED ONTO THE SLIP PLANE AND JOINED BY PARTIAL 'b1' THROUGH THE STACKING FAULT.

in Figure 14a. It is obvious that the Burgers vector of these dislocations must be such as not to permit their dissociation.

Stacking faults are also seen to originate at the intersection of a fault plane with another slip plane as shown at 'c' in Figure 14m. There are pile-ups of dislocations at the intersection of slip planes, which cause a considerable build up of stresses at these sites. One of the possible mechanisms for the release of these stresses is the cross-slip of the lead dislocation of a pile up. It is proposed that sometimes these stresses could also be released by the dissociation of perfect dislocations into partial dislocations and corss-slip of one of these partials on to the next slip plane where it is connected to the other partial through a stacking fault. The operation of the above mechanism on parallel slip planes results in the formation of overlapping stacking faults.

From our experimental observations the sequence of operation of the various mechanisms seems to be as follows:

The grain boundary mechanism operates at very low strains (less than 3.0×10^{-4}). Then, as the stress is increased, the intersecting slip plane mechanism starts operating and with further increase in the stress twin boundary mechanism starts to operate. In view of the above it is suggested that grain boundaries are the easiest sources of dislocations and that the twin boundaries are the more difficult sources of dislocations, and also that their availability for deformation faulting is of the same order.

5. CONCLUSIONS

1. Grain boundaries and twin boundaries were observed to act as dislocation sources. The grain boundaries were seen to generate dislocations at a strain of 1.0×10^{-4} and twin boundaries at a strain of 5.0×10^{-4}.

2. The amount of dislocation entanglement up to 3.0×10^{-4} strain was not apprecialbe, as compared to that beyond a strain of 4.0×10^{-4}. However, at all levels of strain, some dislocation activity and entanglement in some restricted areas was observed. Thus, it may be concluded that dislocation mobility is present even at a strain as low as 1.0×10^{-4}. This was further confirmed by the electrical resistivity and tensile test results.

3. The electron-microscopic examination of polycrystalline nickel specimens deformed in tension showed a non-uniform distribution of dislocations. This was further supported by the tensile test results.

4. The nature of variation of yield stress vs prestrain suggests a higher rate of dislocation entanglement during the initial stages of the deformation and could be attributed to the high dislocation mobility.

5. The appearance (electron microscopic examination) of dislocation loopes, jogs on dislocations and point defect clusters at a few of the localized areas, even at a strain of 1.0×10^{-4}, showed that point defects were produced at very low tensile deformations. Their concentration was measured by electrical resistivity and was found to follow the following relation.

$$c_v \text{ (at pct vac.)} = 4.54 \times 10^{-3} \varepsilon^{0.36}$$

where ε = Total strain.

It is proposed that these point defects are produced during the movement of jogged dislocations.

6. From ageing studies it is concluded that vacancies annealed out by some complex process. The analysis carried out to determine the 'order of reaction' suggested that these annealed out by condensation on dislocations.

7. The presence of point defect clusters (in the specimen deformed under the electron microscope) within the grains and their absence near the grain boundaries suggested that grain boundaries may also act as sinks for point defects.

8. Fractional change in resistivity $\left(\frac{\Delta\rho}{\rho}\right)$ of polycrystalline nickel deformed in tension was found to be related to the tensile strain (ε) by the following relationship:

$$\frac{\Delta\rho}{\rho} = 0.5 \times \varepsilon^{0.66}$$

9. Complete recovery of increase in resistivity while ageing of specimens deformed up to 3.0×10^{-4} strain indicated no net increase in dislocation density. In view of this the dislocation activity within this strain is proposed to be due to the rearrangement of dislocations within the grain boundaries.

10. The formation of dislocation cells in thin foils deformed in the microscope was not observed, because the dislocations and point defects, are easily lost from the surface, which are so important for entanglement.

11. The first appearance of dislocation cells after a strain of 4.0×10^{-4} and an appreciable amount of residual lattice strain (RLS) after a strain of 3.0×10^{-4} confirmed that RLS in polycrystalline nickel was due to dislocation cell structure.

12. From the nature of the substructure of areas bounded by cell walls, it was concluded that the cell walls are sources of hydrostatic stresses.

13. Single stacking faults, overlapping stacking faults and deformation twins were produced during tensile deformation of polycrystalline nickel. These faults were analysed and found to be intrinsic in nature.

14. The stacking faults were seen to originate either:

a) at grain boundaries

b) at twin boundaries, and

c) at the intersection of slip planes.

It is porposed that a proper crystallographic orientation of the fault plane with respect ot these sites, where faults originate, is a necessary precondition for faulting to take place.

15. Yield stress (σ_γ) vs prestrain (ε) was found to follow the following relationship:

$$\sigma_\gamma = 16.5 \times 10^3 \, \varepsilon^{0.16}$$

6. SUGGESTIONS FOR FUTURE WORK

1. X-ray diffraction, electron microscopic studies coupled with resistivity on single crystals of nickel to further investigate the sources of residual lattice strains.
2. Electron microscipic studies to reveal the grain boundary sub-structure and its effectiveness as dislocation source.
3. Measurement of stacking fault energy of pure nickel by the annealing of dislocation loops produced by the guenching from higher temperatures.
4. The nature, origin and interactions of line and point defects in single crystals and bi-crystals of nickel deformed in the microplastic region and their relation to polycrystalline material.
5. The nature, origin and interactions of line and point defects in single crystals and bi-crystals of nickel deformed with varying strain rates.
6. The effect of varying strain rates on microplastic region and its correlation to the micro-structure.
7. The effect of supersaturation of point defects on the mechanical properties and dislocation dynamics, in polycrystalline and single crystal material.

7. REFERENCES

1. W. Bollmann, Phys. Rev., 1956, V 103, p. 1588.

2. P.B. Hirsch, R.W. Horne and M.J. Whelan, Phil. Mag., 1956, V, 1, p. 677.

3. Z. Basinski, Symp. Role of Substructure in Mechanical Behaviour of Metals (Technical Document Report No. ASD-TDR-63-324, 1963), p. 227.

4. P.B. Hirsch, Relation between structure and mechanical properties of metals (H.M.S.O., London, 1963), p. 40.

5. Madar, Seeger and Thieringer, J. Appl. Physics, 1963, V 34, p. 3376.

6. A. Howie, Proc. European Regional Conf. Electron Microscopy (Delft, 1961), p. 183.

7. Fowrie and Murphy, Phil. Mag., 1962, V 7, p. 1617.

8. Madar, Electron Microscopy and Strength of crystals (Interscience, New York, 1963), p. 183.

9. Essmann, Physica Status Solidi, 1963, V 3, p. 932.

10. P.R. Swann, Dislocation arrangements in FCC metals and alloys, Electron microscopy and strength of crystals (Interscience, New York, 1963), p. 131.

11. D. Kuhlmann - Wilsdorf, R. Maddin and H.G.F. Wilsdorf, Am. Soc. Metals Symp. on strengthening mechanisms in solids, 1962, p. 137.

12. N.F. Mott, Trans. Am. Inst. Mining Met., Petrol Engrs., 1960, V 218, p. 962.

13. B. Swaroop and K. Tangri, Trans. AIME, 1969, V 245, p. 61.

14. A.C. Damask and G.J. Dienes, Point defects in metals, Gordon and Breach, 1963, p. 188.

15. T. Broom, Proc. Phys. Soc., 1952, [B], V 65, p. 871.

16. P.G. Klemens, Australian J. Physics, 1953, V 6, p. 122.

17. Tweedale, Cited in Canad. J. Physics, 1956, V 34, pp. 1217 and 1234 (Discussion).

18. F.J. Blatt, F.S. Ham and J.S. Koehler, Bull. Amer. Phys. Soc., 1956, [ii], V 1, p. 115.

19. H.G. van Buren, Philips Res. Rep. 1957, V 12, pp. 1 and 190.

20. M.C. Martin and K.F. Welton, Acta. Met. 1967, V 15, p. 571.

21. H. Kressel, D.W. Short and N. Brown, Acta. Met., 1967, V 15, p. 525.

22. D. Schumacher, W. Schule and A. Seeger, Z. Naturforsch, 1962, V 17a, p. 228.

23. W. Schule, J. Phys. Soc. Japan, 1963, V 18, Suppl. III, p. 293.

24. Beeston et al., Met. Sci. Journal, 1968, V 2, p. 12.

25. A. Seeger, Z. Physik, 1956, V 144, p. 637.

26. J.W. Matthews, Acta. Met., 1968, V 16, p. 35.

27. J.W. Matthews and D.L. Allison, Phil. Mag., 1963, V 8, p. 1283.

28. M.J. Whelan and P.B. Hirsch, Phil. Mag., 1957, V 2, pp. 1121 and 1303.

29. J. van Landuyt, R. Gevers and S. Amelinckx, Phys. Stat. Solidi, 1965, V 9, p. 135.

30. Hirsch, Howie, et al., Electron Microscopy of thin crystals, Butterworths 1965, pp. 230-232.

31. A. Art, R. Gevers and S. Amelinckx, Phys. Stat. Soli., 1963, V 3, p. 697.

32. Pages (188-190) of Ref. 30.

33. G. Baro, H. Gleiter and E. Hornbogen, Mat. Sci. and Eng., 1968, V 3, p. 92.

34. D. Kuhlmann - Wilsdorf and H.G.F. Wilsdorf, on the origin of dislocation tangles and loops in deformed crystals by Thomas and Washburn, Interscience Publishers, 1963, pp. 575-604.

35. G. Schoeck and A. Seeger, Defects in Crystalline Solids, Phys. Soc. London, 1955, pp. 340-346.

36. A. Seeger, Dislocations and mechanical properties of crystals, Wiley, New York, 1957, pp. 340-346.

37. D. Kuhlmann- Wolsdorf and H.G.F. Wilsdorf, J. App. Phys., 1960, V 31, p. 516.

38. F. Seitz, Advances in Physics, 1952, V 1, p. 43.

39. N.F. Mott, Phil. Mag., 1952, [VII], V 43, p. 1151, 1953, [VII], V 44, pp. 187 and 742.

40. H.G. van Buren and Jongenburger, Nature, 1955, V 175, p. 544.

41. H.G. van Buren, Acta Met. 1955, V 3, p. 519.

42. J. Friedel, "Les Dislocations", 1956, Paris (Gauthier-Villars).

43. A. Seeger, Phil. Mag., 1955, V 46, p. 1194, 1957, Report Lake Placid Conference on dislocations and mechanical properties of crystals (New York, J. Wiley), p. 243.

44. L. Reimer, Phys. Verh., 1957, V 8, p. 48.

45. R.E. Smallman and K.H. Westmacott, Phil. Mag., 1957, V 2, p. 669.

46. J.W. Christian and J. Spreadborough, Phil. Mag., 1956, V 1, p. 1069.

47. P. Haasen, Phil. Mag., 1958, p. 384.

48. H. Hashimoto, A. Howie and M.J. Whelan, Phil. Mag., 1960, V 5, p. 967.

APPENDIX

I METHOD OF ANALYSIS TO DETERMINE THE NATURE OF STACKING FAULT

The sense of the lattice displacement is defined in the usual way such that if the lower part of the crystal is displaced with respect to the upper part (Figure 24) so as to give rise to an intrinsic fault then the sense of 'R' (the displacement vector) must be in the upward direction. Conversely if an extrinsic fault is to be formed then 'R' must be in the downward sense as shown in Figure 24. The micrograph can always be oriented such that the fault plane slopes as shown in Figure 24. It is clear therefore that the phase angle $\alpha = 2\pi g.R$ is of opposite sign for intrinsic and extrinsic faults for the same 'g' vector. As shown in Figure 24 for each sense of 'R' there are two possibilities for the direction of 'g', so that the angle 'β' between 'g' and 'R' must be known to be acute or obtuse before identification of 'R' is possible.

Since the magnitude of R is always the same for a given defect, all the possible values of Cos β can be obtained since $\alpha = 2\pi|g||R|$ Cos β. The sign of α is obtained from the color of the first fringe, 'g' is known from diffraction pattern, hence the sense of R can be deduced which is compatible with the observed values of α, and g, and the possible 'β' values. Thus for a 111 reflection with positive 'g' on the R.H.S. of the fault plane, if the first fringe is black (on a positive print), $\alpha = \frac{-2\pi}{3}$, Cos β is -1/3 for $|R| = a\sqrt{3}/3$ so that R and g are obtuse and the fault is intrinsic.

Before presenting an illustrated example, the more significant results of the contrast analysis from stacking faults by Hashimoto et al.[48] are:

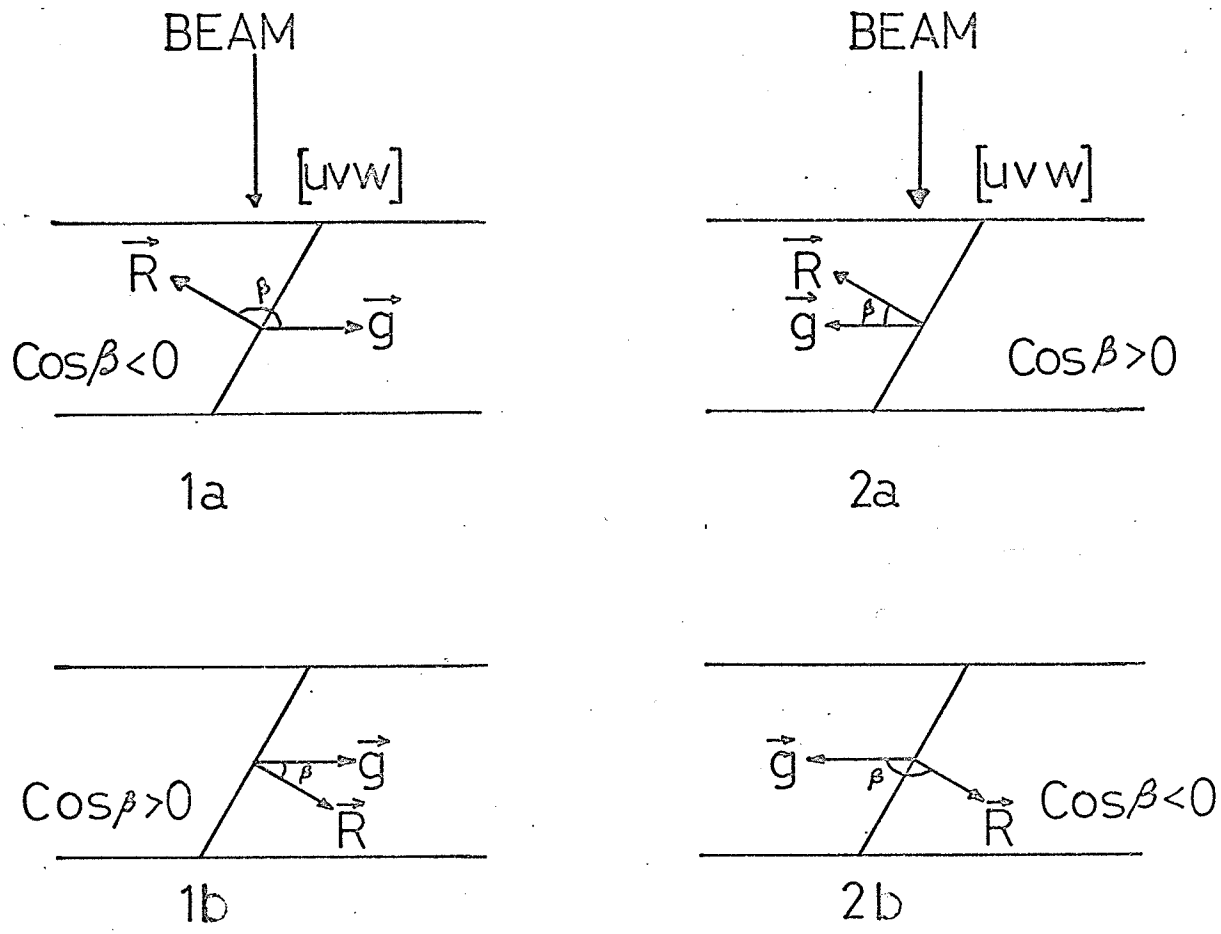

FIG.24 POSSIBLE RELATIVE ORIENTATIONS OF THE DIFFRACTION VECTOR g AND THE DISPLACEMENT VECTOR R FOR(a) INTRINSIC AND(b) EXTRINSIC FAULTS.

1. The dark field image (of stacking fault) is asymmetrical but the bright field image is symmetrical.
2. The top surface of the foil can be determined from the non complementary nature of the bright and dark field images.
3. The entensity of the first fringe is determined by the sign of the phase factor 'α'. When 'α' is positive the first fringe is bright and vice-versa on a positive photographic print.

For example fault in Figure 11g has foil top at the right edge and since the first fringe is dark the $\alpha = \frac{-2\pi}{3}$. The 'g' is $[2\bar{2}0]$ and pointing towards right of the fault plane, therefore Cos β is negative and hence obtuse. Therefore vector R is pointing up and the fault is intrinsic in nature.

Other faults were also analysed in the same manner and the results are tabulated below.

Table 11

Nature of the Stacking Faults

ıre No.	Top of the Foil	Nature of first Fringe (positive Plate)	Phase Factor 'α'	Reciprocal lattice vector 'g'	Cos'β'*	Orien-tation of 'g' with fault	Nature of the fault
	Right edge	Dark	$-\frac{2\pi}{3}$	$[2\bar{2}0]$	-ve	Right	Intrinsic
	Right edge	Bright	$+\frac{2\pi}{3}$	$[0\bar{2}2]$	+ve	Left	Intrinsic
	Left edge	Bright	$+\frac{2\pi}{3}$	[002]	+ve	Right	Intrinsic

= $2\pi g.R = 2\pi \, |g||R| \text{Cos } \beta$

= Reciprocal lattice vector

= Displacement vector